Dibris

ISTITUTO ITALIANO DI TECNOLOGIA

UNIVERSITÀ DI GENOVA

FONDAZIONE ISTITUTO ITALIANO DI TECNOLOGIA (IIT)

Doctoral School on "Bioengineering and Robotics"

Curriculum: "Bionanotechnology"

XXXI Cycle

INTERACTION BETWEEN NANOSTRUCTURED MATERIALS AND SYNTHETIC AND PLASMATIC MEMBRANES

Doctor of Philosophy (PhD) Thesis

Supervisor: Prof. Alberto Diaspro

Tutor: Dr. Silvia Dante

PhD candidate: Barbara Salis

To Mom and Dad

Declaration

I hereby declare that except where specific reference is made to the work of others, the contents of this dissertation are original and have not been submitted in whole or in part for consideration for any other degree or qualification in this, or any other university. This dissertation is my own work and contains nothing which is the outcome of work done in collaboration with others, except as specified in the text and Acknowledgements. This dissertation contains fewer than 65,000 words including appendices, bibliography, footnotes, tables and equations and has fewer than 150 figures.

Barbara Salis

December 2018

Acknowledgements

My first thanks go to the Nanoscopy&NIC@IIT group: to my supervisors Dr. Silvia Dante for her kindness, patience and perseverance with which she supervised me during these years and Prof. Alberto Diaspro for the opportunity he gave me to work in such a great environment as IIT is. Then I would like to thank all my colleagues for their support, for their help and for the nice time we spent together.

I would like to thank Dr. Marco Salerno and Dr. Amirreza Shayganpour for involving me in the project of anodic porous alumina and Dr. Teresa Pellegrino for the opportunity of working with nanoparticles in her team.

Thanks to Dr. Silvia Dante for the analysis of Derjaguin, Landau, Verwey e Overbeek theoretical model, to Dr. Tiziana Ravasenga for taking care of neuronal cell cultures and to Amira El Merhie for the Neuro2a and Chinese hamster ovary cell cultures.

Thanks to Giammarino Pugliese for his help with chemistry lab and Sergio Marras for x-rays diffraction measurements. Riccardo Carzino for the help with the custom made trough and Marco Scotto for the help with the confocal microscopy setup.

I want to thank my parents for the support and the encouraging words in moments of justified nervousness in the latter period.

I have to thank the person who, with enormous patience, has always listened to my everyday problems, and with right words managed to calm me and suggest me the right advice to deal with: thanks Dario for always being there.

Publications

Peer-reviewed journals _____

2018

B Salis, G Pugliese, T Pellegrino, A Diaspro, S Dante (2018) *Polymer Coating and Lipid Phases Regulate Semi-Conductor Nanorods' Interaction with Neuronal Membranes: a Modeling Approach*, ACS chemical neuroscience

2017

Salerno M., Shayganpour A., **Salis B.**, Dante S. (2017). *Surface-enhanced Raman scattering of self-assembled thiol monolayers and supported lipid membranes on thin anodic porous alumina*. *Beilstein Journal of Nanotechnology*, vol. 8, pp. 74-81, 2190-4286.

Conference Proceedings _____

2017

Shayganpour A., Salerno M., **Salis B**., Dante S. (2017). *Towards a single bioactive substrate combining SERS-effect and drug release control based on thin anodic porous alumina coated with gold and with lipid bilayers*. *MRS Advances, pp. 1-8.*

Conference Presentations_____

Posters

2018

Barbara Salis, Sahitya Kumar Avugadda, Amira El Merhie, Teresa Pellegrino, Alberto Diaspro, Silvia Dante, *Interaction of nanoparticles with cellular and model membranes: influence of surface charge, size and membrane potential.* ICONAN 2018, Rome, Italy.

B Salis, A Quarta, T Pellegrino, A Diaspro, S Dante "*Surface charge*

2017 | *regulated adsorption of semiconductor polymer coated nanorods on lipid membranes"* European biophysics journal with biophysics letters 46, S192-S192

Orals

2018 | **Barbara Salis**, Teresa Pellegrino, Alberto Diaspro, Silvia Dante, *Interaction of nanoparticles with model membranes: influence of surface charge and membrane complexity.* ANNIC 2018. Berlin, Germany.

Abstract

Understanding the interplay between nanostructured materials and cell membranes is the basis of their possible usage for therapeutics and for engineering new bio-applications. With the aim to unravel the mechanisms of interaction at the molecular scale, I have studied during my PhD the interaction between CdSe/CdS semiconductor nanorods (NRs) and polymeric micelles with model and plasmatic lipid membranes. NRs were *in-house* synthetized and functionalized with different amount of bis-amino polyetilenglycol (PEG) and a tertiary amine to tune their surface potential (ζ) between -50 mV and +10 mV. Their interaction with lipid mixtures of different composition in form of supported lipid bilayers (SLBs), lipid monolayers (LMs) and different *in vitro* cell lines was tested. In particular, NRs adsorption to SLBs was monitored by quartz crystal microbalance with dissipation monitoring (QCM-D) varying lipid mixtures charge and investigating the influence of gel phase domains; interactions with LMs same in composition as SLBs were measured by surface pressure-area isotherms. Results showed that tuning the mutual properties of the system regulates the interaction with NRs on the membranes and that the increase of membrane complexity inhibits it: in particular a strong interaction was registered with fluid state membranes and NRs opposite in charge when $\Delta\zeta > 70$ mV, whereas the interaction was hindered in presence of gel phase domains. LMs models gave more detailed information, showing removal of lipid molecules from air-water interface or insertion of NRs between lipids according to the overall system charge. QCM-D and surface pressure-area isotherms results were in agreement.

Since the polymer coating of the NRs was shown to regulate the interaction, in order to elucidate its effect I have employed also fluorescent polymeric micelles of different dimension (60 and 300 nm in diameter). I have tested the interaction of both NRs and micelles with different cell lines, namely post-natal mouse neuronal network (known to have a dynamically changing membrane potential), mouse neuroblastoma Neuro2a (that can differentiate in neuronal-like cells) and Chinese hamster ovary cells (epithelial, with a static membrane potential), using confocal microscopy both on fixed samples and in real time. Preliminary results showed adhesion of negatively charged NRs and micelles on both dynamic potential

membrane cell lines. Again a threshold value was found for NRs interacting with neurons (ζ_{NR} < -18 mV), similarly to what was observed with models. A neurotoxin was then introduced in the experiments, to reduce the spikes of the active cells.

A satellite project is finally presented as a full paper at the end of the thesis. The project concerns the fabrication and characterization of thin anodic porous alumina (tAPA) substrates, which surface was made surface-enhanced Raman spectroscopy (SERS) -active by coating with a thin gold (Au) layer. My part in this project was related to the monitoring of the chemisorption of thiols and the formation of SLB models from lipid vesicles by using the QCM-D technique on Au substrates.

Table of Contents

List of Figures

List of Tables

List of Equations

List of Abbreviations

AFM	atomic force microscopy
APA	anodic porous alumina
C-18P	(poly(maleic anhydride-1-octadecene)
DAPI	4′,6-diamidino-2-phenylindole
DLVO	Derjaguin, Landau, Verwey and Overbeek
DLPC	1,2-dilauroyl-sn-glycero-3-phosphocholine
DMPC	1,2-dimyristoyl-sn-glycero-3-phosphocholine
DOPC	1,2-dioleoyl-phosphatidylcholine
DOPE	1,2-dioleoyl-phosphatidylethanolamine
DOTAP	1,2-dioleoyl-3-trimethylammonium-propane
DPPC	1,2-dipalmitoyl-sn-glycero-3-phosphocholine
LB	Langmuir-Blodgett
LM	lipid monolayer
LML	lipid multilayer
N2a	Neuro 2a
NP	nanoparticle
NR	nanorod
NR-	negative nanorod
NR+	positive nanorod
PBS	phosphate buffered saline
POPC	palmitoyl-oleoyl phosphatidylcholine
POPS	palmitoyl-oleoyl phosphatidylserine
QCM-D	quartz crystal microbalance with dissipation monitoring
SAM	self-assembled monolayer
SDS	sodium dodecyl sulfate
SERS	surface enhanced Raman scattering
SLB	supported lipid bilayer

TTX	tetrodotoxin neurotoxin
XRD	X-rays diffraction

Introduction

The global outline of my PhD project was the study of the interactions occurring between nanoparticles (NPs) and cells at cell plasma membrane interface. After a general description of the plasmatic membrane, which are its most important components and how is possible to mimic them using models (described in chapter 1), and a description of the nanostructured materials and which are their applications (chapter 2), I introduce the NPs employed during my work, i.e. CdSe/CdS nanorods (NRs) and polymeric micelles and the techniques I used to characterize and functionalize them (chapter 3). The most relevant part of my PhD project was carried on through the use of quartz crystal microbalance with dissipation monitoring technique (QCM-D) and Langmuir trough to perform pressure – area (π - A) isotherms applied to different lipid model membrane systems, in particular supported lipid bilayers (SLBs) and lipid monolayers (LMs). All the techniques employed are described in chapter 4. Different lipid mixtures, characterized by different overall charge and phase separation behavior, have been employed together with NRs, and the results are described in chapter 5. NRs were then employed, also with custom-made polymeric micelles, in the study of the interaction between NPs and plasmatic membranes from different cell lines in vitro, such as neurons and epithelial cell. This study was carried out by the means of laser scanning confocal microscopy and results are showed in chapter 6.

Then, an appendix describes the study of the same NRs used in the rest of the thesis, but without the presence of the surface tuning functionalization layer, together with model membranes. Here, the x-rays diffraction technique is added as an investigation tool.
Finally, a paper in which I was involved, concerning the use of anodic porous alumina substrates as bio-sensing surfaces, is attached.

Chapter 1
Cytoplasmic Membrane and Model Systems

The cytoplasmic membrane of eukaryotic cells (Figure 1.1) is a complex structure with the main function to separate the inner environment of the cell from the extracellular space. It is selectively permeable to ions and organic molecules [1] and is involved in important biological processes including bidirectional transport of molecules and cell adhesion. It is mainly composed by a double layer of amphiphilic lipid molecules with embedded proteins, in a ratio which can vary significantly between different cell types [2-4].

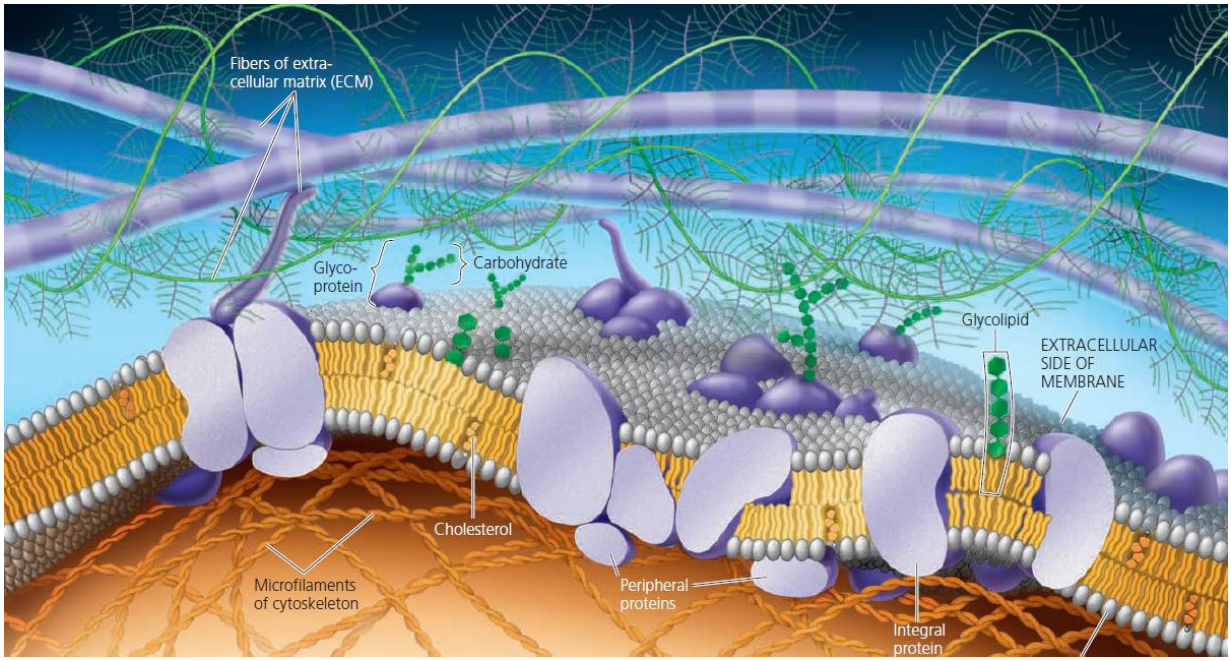

Figure 1.1 Schematic representation of a eukaryotic plasmatic membrane (from *Campbell Biology 10th Edition*).

Membrane lipids are mainly divided in three classes: phospholipids, glycolipids, and sterols [2, 4, 5]. The most abundant are phospholipids; because of their amphiphilic nature, in aqueous media and in physiological conditions they tend to organize in a lamellar configuration, typical of biomembranes, with the polar head pointing toward the aqueous medium and the hydrophobic tails facing each other. Proteins can be temporarily attached to

the bilayer surface (peripheral proteins) or can present a hydrophobic domain which is permanently embedded in the membrane (integral proteins) [5].

The first model of plasma membrane which described in a proper way the molecular organization of both lipids and proteins was the fluid mosaic model, proposed by Singer and Nicolson in 1972 [3]. According to their hypothesis, the membrane was considered as a mosaic of proteins moving in a bidimensional phospholipid fluid, but this model did not take into account any lateral organization of proteins or lipids, well established nowadays [6, 7]. Also, several evidences collected in the last decades suggested that lipid distribution in the cell membrane matrix is not uniform, but presents several microdomains, termed "lipid rafts" (Figure 1.2), which differ in composition and physical properties from the surrounding regions and which are thought to have an important role in many cellular processes, such as cell signaling and protein trafficking [8-10].

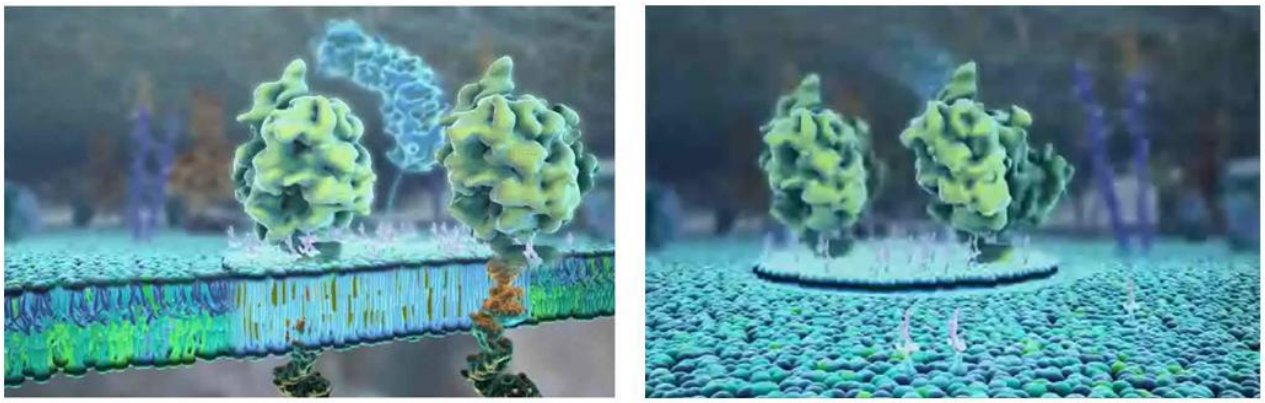

Figure 1.2 – Representation of lipid rafts, composed by sphingolipids, cholesterol and proteins (from "*The Inner Life of the Cell", Harvard University*).

The propensity of plasma membrane to organize in distinct lateral domains is strongly related to the high heterogeneity of membrane lipids, which can coexist in different lipid phases according to their molecular structure (see paragraph 1.1). Multi-component model systems can

be used to reproduce raft behavior in a scale suitable for most of *in-vitro* investigation techniques.

1.1 Membrane Lipids and Lipid Phases

The membrane structure is not fixed, but its high fluidity makes it continuously change at the nanoscale in response to stimuli of the external environment. The composition of the plasma membrane is cell-type dependent, but in each cell the largest fraction are the phospholipids, that include most of the 50% of total lipids of the membrane. Glycolipids only 2% and the rest is made by sterols [11].

The hydrophobic tails in phospho- and glycolipids contain an even number of carbon atoms, typically 16- and 18-carbon (C). They may be saturated or unsaturated, i.e. could contain double C-C bonds (in the unsaturated ones). The length of the chains and the number and position of unsaturation affect the membrane fluidity: unsaturated lipids have bended carbon chains, preventing the tails from packing together tightly and so decreasing the melting temperature and the fluidity of the membrane [12, 13]. The entire membrane is bound via non-covalent interaction of the hydrophobic tails. Physiologically, phospholipid molecules in the cell membrane are in the so called "liquid crystalline state", i.e. the molecules are free to

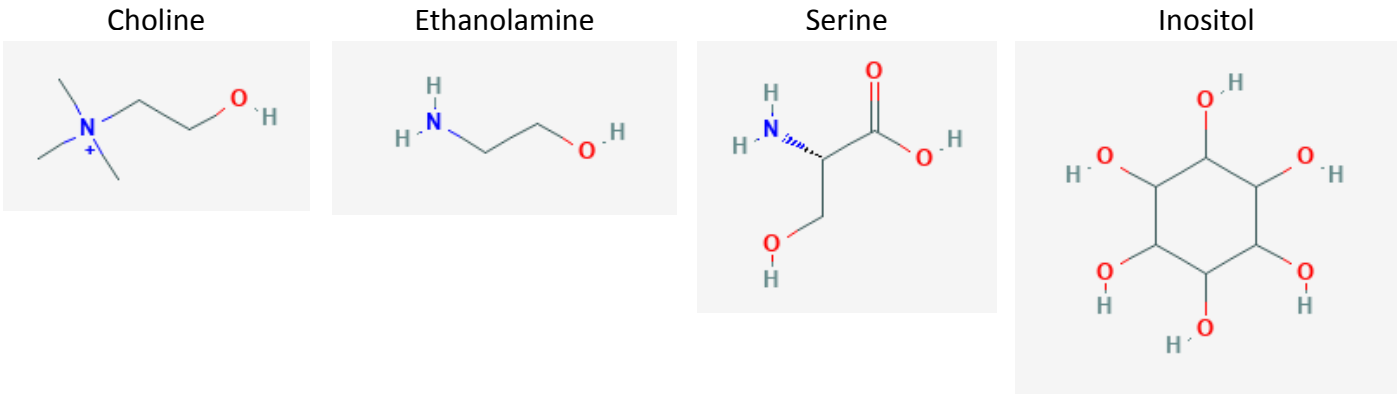

Figure 1.3 Structures of most common lipid polar heads (modified from *https://pubchem.ncbi.nlm.nih.gov/*).

diffuse along the layer in which they are [14-16]. The major structural lipids in plasma membrane, glycerophospholipids, are constituted by a glycerol backbone which binds, through an ester bond, two saturated or *cis*-unsaturated hydrophobic tails. A polar head, which may be choline, ethanolamine, serine, or inositol, (Figure 1.3) is also bound to the glycerol backbone through a phospho-ester bond.

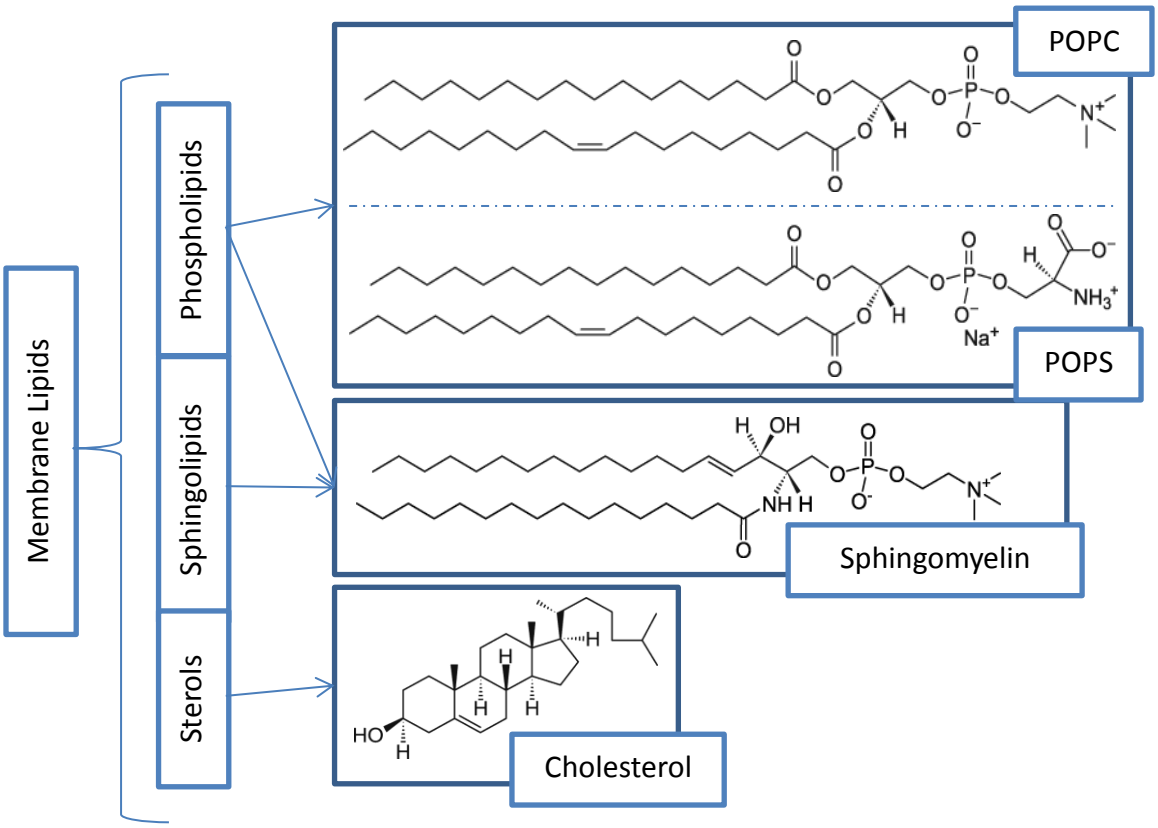

Figure 1.4 – Most common plasma membrane lipids (images from *avantilipids.com*): each box shows exemplifying molecule for each class. From top to bottom: palmitoyl-oleoyl phosphatidylcholine (POPC), palmitoyl-oleoyl phosphatidylserine (POPS), sphingomyelin, cholesterol.

Sphingolipids represents the other class of structural lipids in plasma membrane: they consist in a ceramide backbone (a sphingosine linked to a fatty acid), which may bind different

headgroups. The main sphingolipids in mammal membranes are sphingomyelin (SM), a phosphosphingolipid composed by ceramide and phosphocholine. Phospholipids and sphingolipids are amphiphilic molecules, consisting both of a hydrophobic part (diacylglycerol / ceramide) and of a hydrophilic one (polar headgroup). For this reason, in water excess they spontaneously assume a lamellar configuration, with the hydrophobic tails facing each other in order to prevent their interaction with the solvent. Figure 1.4 shows the structure of the most common lipids in plasma membranes.

Non-lamellar phases, induced by the presence of particular lipids such as phosphatidylethanolamine or cardiolipin, are not normally found in plasma membrane, but can appear as a transient state associated to specific membrane events, such as fusion, fission and pore formation [17-19] (Figure 1.5).

Cholesterol is the main non-polar lipid in mammal cell membranes, normally found in the irregular spaces between the hydrophobic tails of the membrane lipids, where it confers a stiffening and strengthening effect on the membrane [20]. Additionally, the amount of cholesterol in biological membranes varies between organisms, cell types, and even in individual cells. It regulates the fluidity of the overall membrane, meaning that cholesterol controls the amount of movement of the various cell membrane components based on its concentrations [20-23].

Lipids are not evenly distributed between the two membrane leaflets [4, 24-27]: phosphatidylcholine, which represents more than half of phospholipids in most of eukaryotic membranes, is mainly located in the outer leaflet, as well as sphingolipids, while phosphatidylserine, phosphatidylethanolamine and phosphatidylinositol are predominantly found in the inner leaflet [28]. Cholesterol resides for more than 70% in the inner leaflet [20, 23]. Nevertheless, its presence and distribution in the outer leaflet is fundamental in determining lipid lateral organization.

As it has been already pointed out, in fact, membranes also present a lateral heterogeneity, characterized by the presence of domains displaying peculiar phase behaviors. Membrane lipids can exist in multiple possible phase states [12, 13, 22, 29] (Figure 1.6),

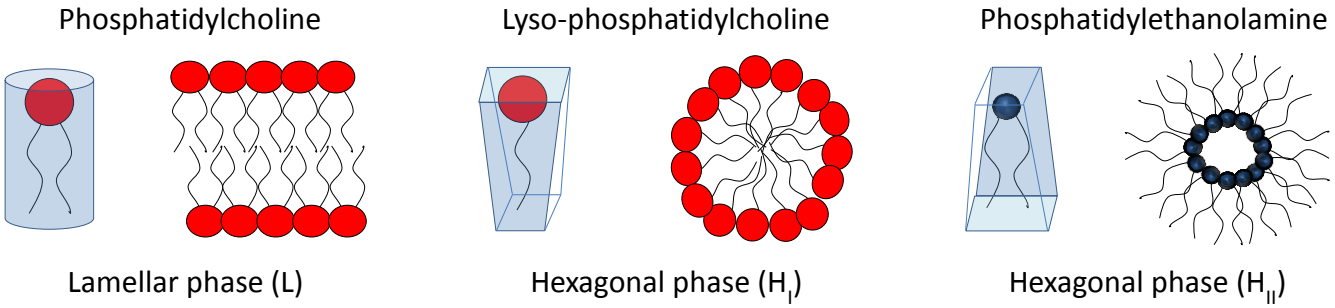

Figure 1.5 – Lipids organize in different lipid phases, according to the volume occupied by the polar headgroup and by the hydrophobic fatty acyl chains [30]. Most of glycerophospholipids in plasma membrane have a cylindrical geometry, which results in a lamellar phase organization.

depending on the length and on the presence of unsaturations in the acyl chains, as well as on temperature. Lipids containing long, saturated chains, such as sphingolipids, tend to organize in a tightly packed lamellar configuration, called solid-ordered or gel phase (*So* or *Lβ*), characterized by a high molecular order and a reduced lateral mobility. Most of phospholipids, on the contrary, contain unsaturated chains, which cause them to be fluid at room temperature. These lipids normally exist in a disordered state, the liquid disordered phase (*Ld* or *Lα*), which has a high lateral diffusion. Phospholipids can form a gel phase only below a specific transition temperature (*Tm*), which, because of the presence of unsaturated chains, is significantly lower than the physiological one (see Table 1.1). The presence of cholesterol between acyl chains may induce a transition both in *Ld* and in *So* phase. In fact, its rigid structure imposes a conformational order between unsaturated phospholipids, affecting their lateral mobility. On the other hand, cholesterol insertion between fully saturated chains strongly increases bilayer fluidity, without significantly perturbing the conformational order.

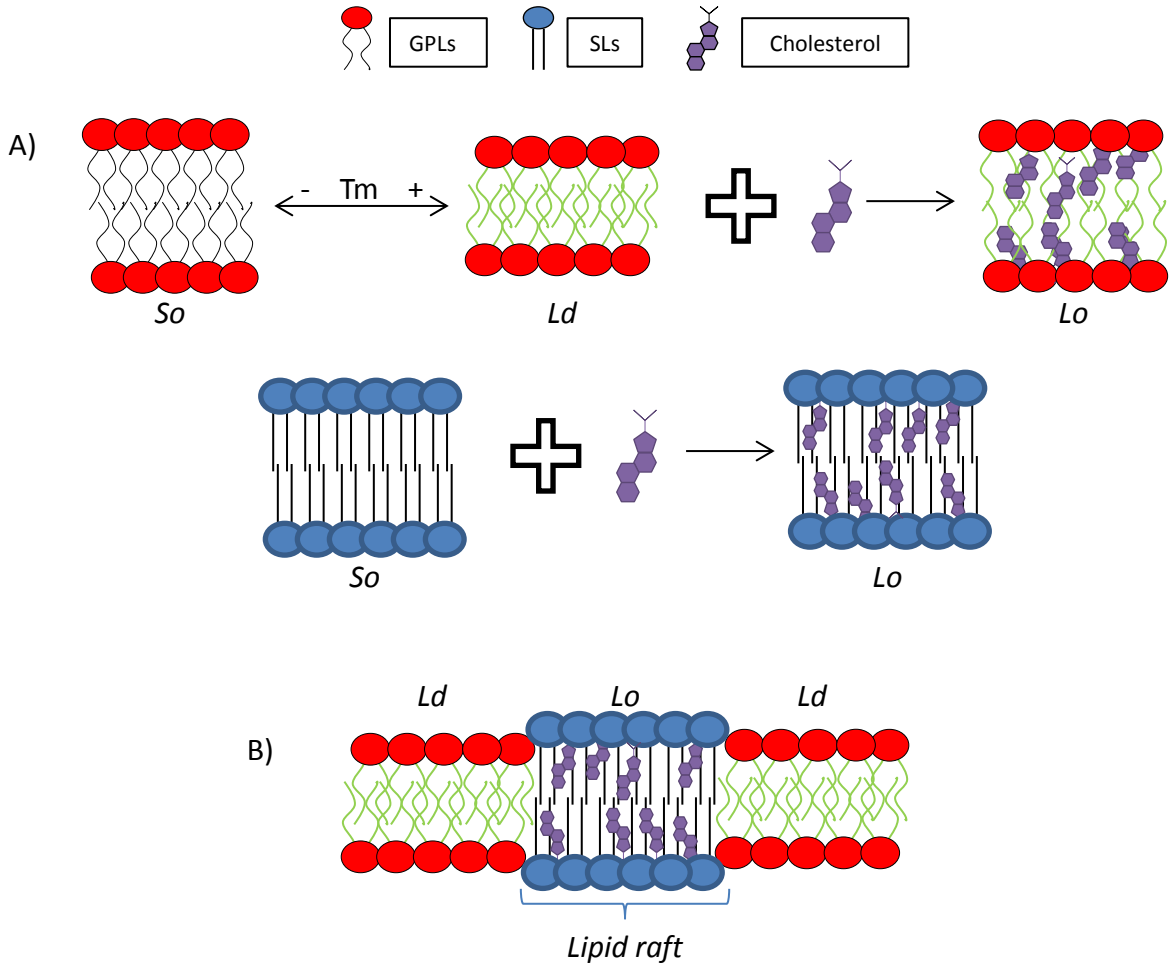

Figure 1.6 – A) Lipid phases of glycerophospholipids (GPLs) and sphingolipids (SLs). Phase transition of pure GPLs mixtures is triggered by a variation of temperature (*T*) with respect to GPLs transition temperature (*Tm*). At body *T* most of GPLs in plasma membrane are fluid, while most of SLs are in *So* phase. Addition of cholesterol induces a transition from both SLs *So* phase and GPLs *Ld* phase into *Lo* phase. **B)** Cholesterol inserts preferentially between SLs and GSLs chains, because of the larger headgroup protection from the solvent. Addition of cholesterol in GPLs and SLs mixture induces *Lo* and *Ld* phase coexistence [31].

In conclusion, the addition of a proper amount of cholesterol in a lipid bilayer can induce a phase transition from either *Ld* or *So* phase into a liquid ordered phase (*Lo*), characterized by a high conformational order and a high fluidity, being the diffusion coefficient generally only two or three times lower than the one measured in the disordered phase [21-23].

	Lipid	C length	Unsaturation degree	Tm (°C)
Saturated chains lipid	DLPC	12 -12	0 - 0	-2
	DMPC	14 -14	0 - 0	24
	DPPC	16 - 16	0 - 0	41
Unsaturated chains lipid	POPC	16 - 18	0 - 1	-2
	POPS	16 - 18	0 - 1	14
	DOTAP	18 - 18	1 - 1	4

Table 1.1 Properties of lipids related to their fluidity: chain length and saturation level. For every lipid, the C-length of every chain and the presence of a double C-C bond (unsaturation degree) is indicated.

1.2 Model Membrane

The investigation of physiological and pathological phenomena happening at the nanoscale at cell interface is extremely challenging, because of the high complexity and heterogeneity of plasma membrane. For this reason, the use of simplified models [32-37] (Figure 1.7), capable of mimicking the behavior of a controlled number of membrane components, can be very interesting. Model membranes basically consist in a single or double layer of phospholipids, typically planar or spherical, or a combination of both. In 1917, I. Langmuir introduced the experimental and theoretical modern concepts of insoluble monolayers. Since that time, and because it has been found to provide invaluable information at the molecular scale, the monolayer technique has been more and more extensively used, and a huge increase in the number of publications has occurred. Half-membranes can be used as useful models, especially in the case of interfacial interactions study. Lipid monolayer (LMs) at the air-water interface are extensively used for the investigation of interactions with lipid head groups [38] (see chapter 4, paragraph 4.4 and 4.5).

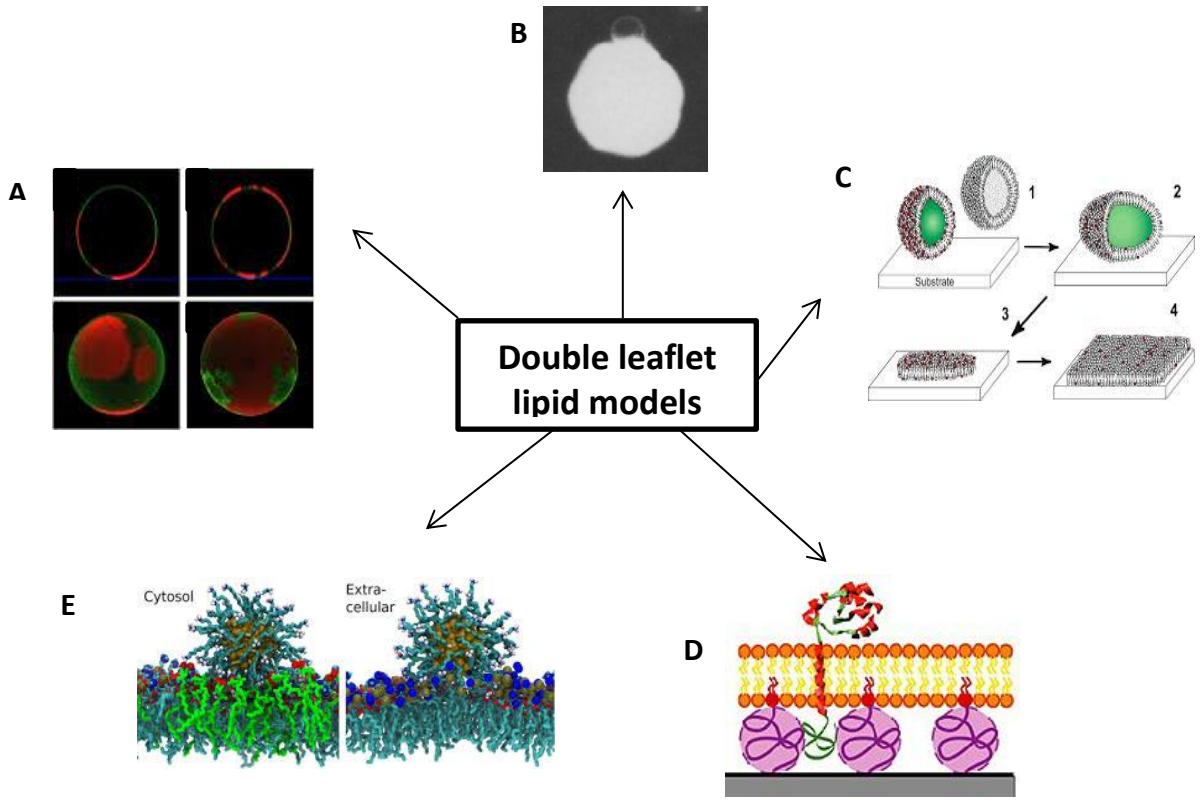

Figure 1.7 – Examples of double leaflet model membranes **A)** GUVs [39] **B)** blebs protruding from cells [40] **C)** supported lipid bilayers on solid substrate [41] **D)** Tethered membranes [42] **E)** mechanical simulations [43].

The simplest spherical model membranes are represented by unilamellar vesicles, ranging from tens (small unilamellar vesicles, SUVs) to hundreds of nanometers (large unilamellar vesicles, LUVs), and, eventually, to tens of micrometers (giant unilamellar vesicles, GUVs). These vesicles can be free-standing, connected to each other or tethered to a substrate. SUVs and LUVs are generally prepared through extrusion or sonication of a solution containing multilamellar vesicles (MLVs), which spontaneously form upon hydration of dried lipid films. Giant liposomes, instead, are usually generated through an electro-formation process. GUVs are important model systems [33], which are mainly used to investigate lipid phase behavior using fluorescent probes [44].

Planar geometry is widely used in surface characterization studies [45-47]. Bilayers supported by a rigid substrate (SLBs), which will be described in the next section, are a valuable tool to simulate the behavior of the lipid part of plasma membrane, but they may present some limitations. First of all, the substrate can influence the study. SLBs do not allow the insertion of transmembrane proteins, because the short distance from the substrate (about 1-2 nm) may induce loss of mobility and, most of all, protein denaturation. This problem can be solved with the use of tethered bilayers [48-50], in which the model membrane is separated from the substrate by a proper linker. Membrane supported by a softer substrate, such as a polymer cushion [51, 52], should be preferred in case of mechanical measurements, since the polymer assembly is a better approximation of the cytoskeleton rather than a rigid surface. As last mention, mechanical simulation approach is becoming more and more important in the investigation of phase behavior [53, 54] and in the study of membrane interaction with different nanoparticles [55, 56].

1.3 Lipid Monolayers

Lipid monolayers can be obtained on the air-water interface of a watery subphase using a Langmuir trough. In the Langmuir model system, various parameters such as lipid composition, subphase, and temperature can be chosen to imitate biological conditions [32, 38, 57, 58]. In addition, lipid monolayers are very well-defined bidimensional system with planar geometry. The most relevant property of a lipid monolayer is its surface pressure, which can be calculated as:

$$\pi = \gamma_0 - \gamma_{surfactant}$$

in which π is the surface pressure, γ_0 is the subphase surface tension (which is 72 mN/m at 25° C for water) and $\gamma_{surfactant}$ is the surface tension of the subphase in the presence of the monolayer [59]. This parameters can be calculated using the Wilhelmy plate method (see chapter 4, paragraph 4.4). Typically, the investigation of lipid monolayers interaction with NPs can be

performed in two ways. First, a lipid monolayer on the water/buffer surface is compressed by applying lateral pressure to a surface pressure (π) at which the lipid packing density is similar to the one of plasmatic membrane (π = 30 mN/m) [57].
By keeping the film area constant, changes in π are recorded upon addition of NPs to the subphase. Alternatively, a NP dispersion can be used as a subphase (usually a buffer with pH 7.4 is used to mimic biological systems) to form a lipid monolayer. The monolayer is then compressed, and the values obtained for the pure lipid and for the lipid with NPs are compared.

Apart from changes in π, changes in lipid morphology at the air-water interface can be studied by Brewster angle microscopy [60]; this method allows *in situ* study of the two-dimensional Langmuir monolayers at the air-water interface. This technique does not use probe compounds or any other modifications to sample for investigation; thus it ensures that the monolayer under investigation is in its original state.

1.4 Supported Lipid Bilayers

Supported lipid bilayers (SLBs) are lipid bilayers formed on flat solid substrates such as silicon or mica form which they are separated by a thin hydration layer (about 1 – 2 nm of watery layer). Thanks to this separation, the lateral fluidity of the lipids is preserved. Generally, SLBs are formed by fusion of lipid vesicles onto these solid supports or by the LB technique. The vesicle fusion technique, introduced in 1984 by Brian and McConnell [61], basically consists in the deposition of a SUVs or LUVs dispersion to a hydrophilic substrate: vesicle adsorption and spreading on the surface may lead, under specific conditions, to bilayer formation. The final result depends both on lipids and substrate physico-chemical properties, as well as on other factors, including temperature, vesicles concentration, and ionic strength of the used buffer, which may affect both vesicle-vesicle and vesicle-substrate interaction.

It is possible that, after the administration, vesicles do not adsorb onto the substrate, they adsorb but remain intact, they first adsorb intact and start forming the bilayer only after having reached a critical coverage, or they rupture instantaneously, creating bilayer patches.

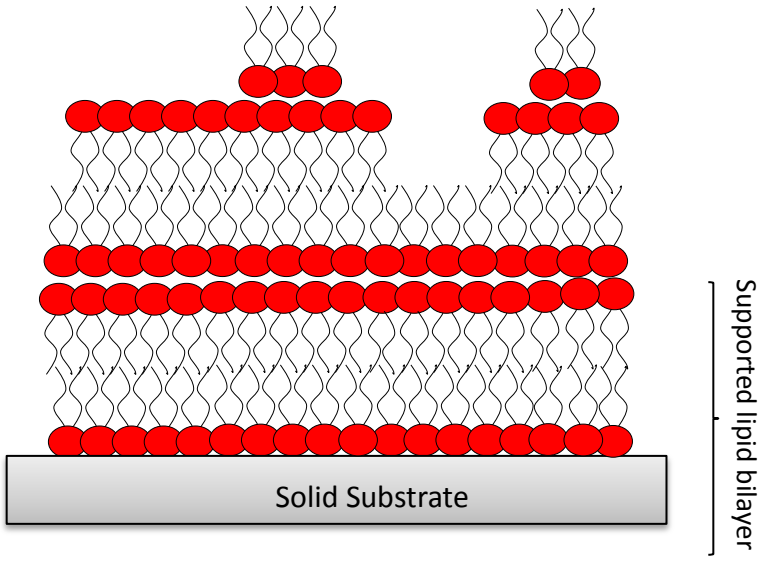

Figure 1.8 Solid supported lipid multilayer in air.

All these situations can be investigated using Quartz Crystal Microbalance with Dissipation Monitoring (QCM-D) [45, 47], that will be introduced in chapter 4.

In conclusion, with a proper choice of experimental conditions, it is possible to form stable, defect-free lipid mono and bilayers, which can be used to mimic the lipid part of plasma membrane and changes in structure, morphology, and surface chemistry. The interactions between membranes and nanostructured objects, such as nanoparticles, can be investigated using various techniques, such as scanning laser confocal microscopy, scanning electron microscopy, transmission electron microscopy, atomic force microscopy, QCM-D, pressure-area isotherms using a Langmuir trough, dynamic light scattering and X-ray scattering.

Chapter 2
Nanostructured materials in bio-applications

Nanoparticles (NPs) are nanostructured materials with all of their dimensions at the nanoscale. They can be synthetized using almost every material and can be inorganic or organic (see figure 2.1). It is widely known that the properties of a material at the nanoscale are different from the bulk material itself; this is why there is a huge need of understanding how they can interact with living organisms.

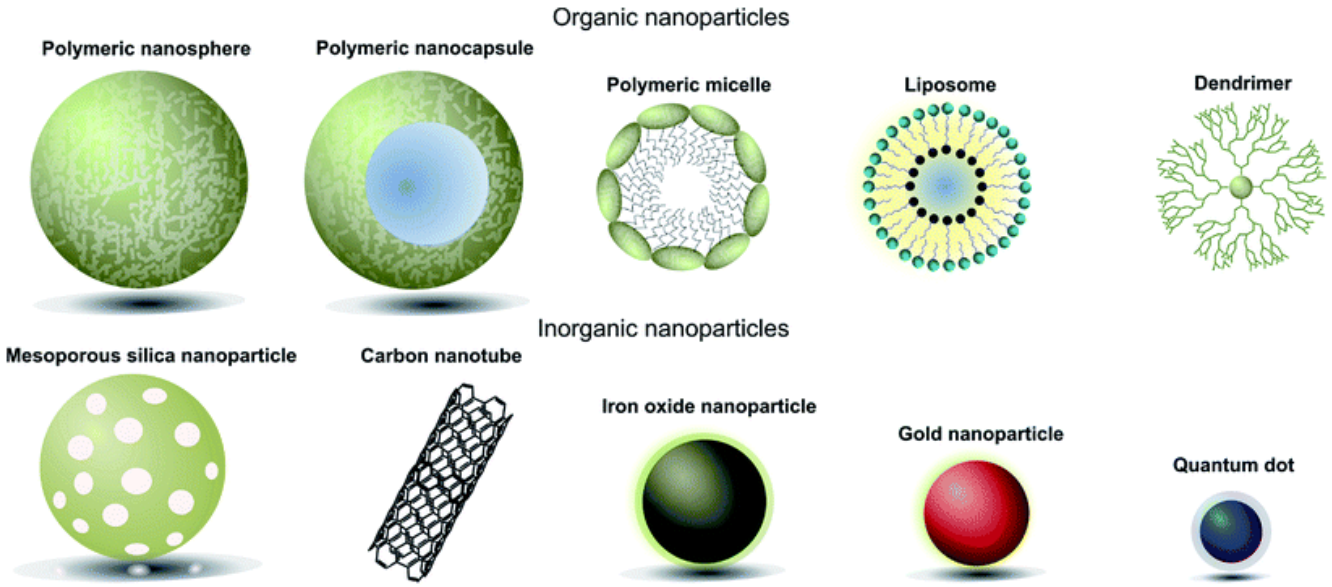

Figure 2.1 Example of existing NPs: organic in the first row, inorganic in the second one. Image from [62].

2.1 State of the art: interaction between nanostructured materials and membranes

Nanostructured materials with nanoscale dimensions (between 1 and 100 nm) are largely employed in biomedical applications today, especially in field as in cancer treatments, bio-imaging, drug delivery techniques and for the development of biosensors [63-67]. Evaluating the NPs' interactions in a physiological environment and understanding which is their effect on human beings can be challenging due to the complexities related to the system under study: the

broad variety of nanomaterial properties that have to be considered (namely the NPs' size, surface charge density and shape [68-72]); the great variations in the biological targets (namely cell lines and biomarkers [70]); the conditions (such as the NPs' concentration [71]) under which the interactions are examined and, overall, the intricateness of living organisms. All these variables affect the interactions and, in turn, could cause possible hazardous effects. The problem related to the complexity of the cellular membrane can be solved using models that can mimic the basic plasma membrane structures, providing a system that is suitable for studying membrane-NP interactions [33, 34].

Studies on the cytotoxicity of engineered nanomaterials have been reported in literature using model membranes [73, 74]: these studies helped to identify a number of mechanisms by which nanomaterials induce toxicity, including membrane damage, such as the formation of thinned regions and holes [74, 75].

In the last decades, the interaction between nanoparticles and model membranes has been investigated by several research groups. The majority of literature on this topic [55, 76-78] concentrate on the interaction of spherical nanoparticles with cellular or model membranes. Verna and Stellacci [79] reviewed how synthetic and natural chemical peculiarities of NP surface impact their interaction with lipid bilayers and cells. Granick et al. [80] explained the correlation between the presence of nanoparticles and the change in head-groups in lipid vesicles, inducing gelation in fluid membranes or fluidizing full gel state ones. Barros-Timmons at al. [81] investigated the behavior of lipid monolayers with coated NPs and with the coating alone. They showed that when there is an interaction with an oppositely charged NP, the functionalization alone will induce the same reaction. Also theoretical investigations has been performed by molecular simulations: Vattulainen et al. [82] reviewed atomistic and coarse-grained simulation studies on carbon NPs interacting with lipid membranes, Yang and Ning [83] described the thermodynamics changes occurring during the interaction between zwitterionic membranes and charged NPs, and Weikl et al. [84] investigated the wrapping behavior of NPs with lipid membranes.

Recently, it has been reported that the NPs' interaction with the neuron cell membrane was driven by the surface charge of the NPs and, in the case of negatively charged particles, it induced a neuronal electrical response [70], whereas no interaction was observed in static membrane potential cells (such as glia). These events are reasonably due to the difference in superficial potential between the neuronal membrane and the external functionalization of the NRs. It has been also shown that NPs can play active roles in mediating biological effects to living organisms: the uptake of fluorescent Cadmium Selenium/Cadmium Sulfur (CdSe/CdS) nanorods (NRs) by Hydra vulgaris, a simple model organism, can be tuned by modifying the NR surface charge [85]. This interaction can lead to biological responses in the living animal (a tentacle writhing response) [69].

Also biological elements at the nanoscale can induce modifications in the membrane structure, such as proteins; an example is given by α-Synuclein, a protein capable of undergo a fibrillation process with the consequent formation of plaques, responsible for the onset of many neurological diseases such as Alzheimer, Parkinson or dementia [86, 87].

2.2 Nanostructured substrates

Nanostructured substrates present some of their features at the nanoscale. During my PhD, I was involved in a project in which anodic porous alumina (APA) was employed as a nanostructured material. APA will be described in the next paragraph. Other examples of nanostructured materials that can interact with cell membrane are ultrathin substrates (i.e. graphene [88] and nanoflakes [89]) or nanoporous structures (i.e. nanoporous silica [90] or titania [91]).

2.2.1 Anodic porous alumina

Another class of nanostructured material that I directly employed during my thesis is *anodic porous alumina* (APA, see attached paper). APA is a layered material usually obtained in thick form (≈10 μm thickness scale) from electrochemical anodization in the acidic aqueous electrolyte of aluminum (Al) foils [92]. In APA, the control of pore size, pore density and porosity is achieved by changing the anodization voltage during the fabrication and the etching

parameters during the post-fabrication treatment [93]. It is widely recognized that the APA surface is biocompatible [94] and with its control of the surface roughness can play an important role in the adhesion and proliferation of cells [95, 96]. The self-ordered nano-structured APA after coating with noble metals (such as gold) can be used for plasmonic-based enhanced spectroscopy such as in surface-enhanced Raman spectroscopy (SERS) [97, 98]. In recent years, the thin form of APA (tAPA), resulting from anodization of Al films of less than 1 μm thickness, has been increasingly used because it can be better integrated into applications involving optical microscopy inspection, which requires flat planar substrates. Additionally, the pores in tAPA can potentially serve as nano-wells for localized drug delivery [99]. In fact, while lower in loading capacity with respect to thick APA, 500 nm tAPA can still allocate a significant amount of bioactive compounds, representing a trade-off between the former case of maximized loading and the case of ultra-thin APA showing the highest SERS enhancement [100]. Finally, the controlled roughness of APA could also improve the physisorption of coating layers of functional materials [101].

In the final part of my thesis, a paper describing the project concerning the use of tAPA as a bio-sensing surface is attached.

Chapter 3
Materials and Methods 1: NPs

In this chapter, I will explain the procedure of hydrophilization and functionalization I performed on CdSe/CdS nanocrystals, describing the instrumentation employed.

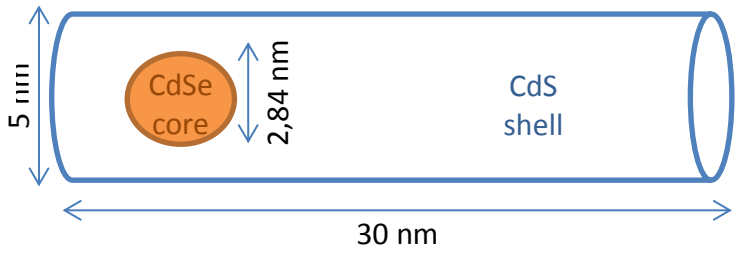

Figure 3.1 Core-shell structure of employed CdSe/CdS NRs.

3.1 Nanorods surface functionalization and characterization

In-house synthetized hydrophobic CdSe/CdS nanocrystals [102] were used in this work. This rod-shaped crystals were 30 nm in length and 5 nm in diameter and diluted in toluene at a concentration of $c_{initial}$ = 7.3 μM, covered by a layer of hydrophobic surfactant, named trioctylphosphine oxide. Table 3.1 shows the NRs' properties and the emission spectrum calculated at the selected wavelength (i.e. 488 nm). Their absorption spectrum is continuous (Figure 3.2). A process of water solubilization was needed to make the crystals suitable for the measurements.

3.2 Water solubilization of hydrophobic nanocrystals

The water solubilization process of the nanocrystals is divided in three steps that are water transfer, cleaning and subsequent characterization.

3.2.1 Water transfer

This step allows covering the hydrophobic sample with an amphiphilic polymer, i.e. (poly(maleic anhydride-1-octadecene), abbreviated as C-18P in the following text. C-18P

intercalates between the hydrophobic chains that cover the surface of the NR, showing its polar head outward.

Properties		ICP results (dilution factor 1000)	
Length (l)	33 ± 7 nm	Cd	9.8 ppm
Diameter (d)	5.0 ± 0.5 nm	S	2.6 ppm
Solvent	Toluene	Se	0.1 ppm
Absorption wavelength	488 nm	NRs concentration	7.3 µM
Emission wavelength	596 nm		

Table 3.1 Properties of the NRs and emission spectra calculated at an excitation wavelength of 488 nm.

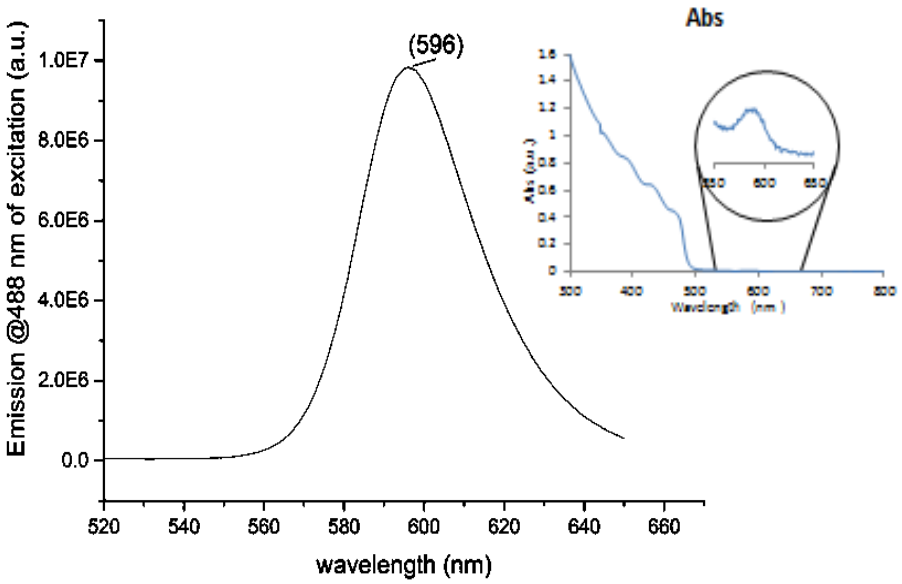

Figure 3.2 Emission spectra at 488 nm excitation wavelength and absorption spectra of NRs (inset).

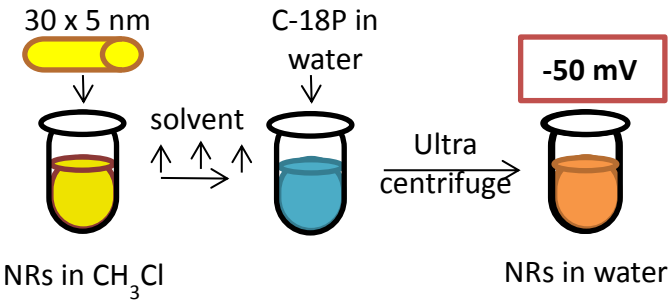

Figure 3.3 Water solubilization process of NRs.

The full coverage of the crystal with polymer's polar head allows the solubilization in a polar solvent, i.e. water [103]. 250 molecules of C-18P per nm^2 of NRs' surface area were sufficient to completely cover the NRs. The surface area of the NRs (A_{rod}) was calculated as the sum of the lateral area (A_{lat}) adds the 2 base areas (A_{base}):

$$A_{rod} = A_{lat} + 2 * A_{base}$$

$$A_{rod} = \left(2 * \pi * \frac{d}{2} * l\right) + \left(2 * \left(\pi * \left(\frac{d}{2}\right)^2\right)\right) = 557{,}4\ nm^2$$

whence

$$\#\text{molecules of polymer} = \left(250\ \frac{molecules}{nm^2} * 557{,}4\ nm^2\right) = 139350\ \text{molecules}$$

Using a stock solution of polymer in chloroform at a concentration of $c_{stock\ C\text{-}18P}$ = 137 mM, I used 100 µL of NRs, ending up with a final concentration of c_{final} = 0,2 µM. The final volume V_{final} was

$$c_{initial} * V_{initial} = c_{final} * V_{final}$$

$$V_{final} = \frac{c_{initial} * V_{initial}}{c_{final}}; \quad V_{final} = 3{,}65\ mL$$

The volume of polymer stock solution needed was then

$$V = \frac{\#\text{molecules of polymer} * c_{final} * V_{final}}{c_{\text{stock C-18P}}}; \quad V = 742\ \mu\text{L}$$

4 mL of chloroform, 100 µL of NRs, 742 µL of polymer stock solution were then put, in this order, in a round-bottom flask (big enough to contain 4 times the volume needed). After a proper stirring, the solvent was let to evaporate using a Rotavapor system, setting the temperature at 40 °C and evaporation pressure (for chloroform) ≈ 430 mmHg for 1 hour. Once the solvent completely evaporated, I added 4 mL of pH 9 borate buffer to re-suspend the sample, which was left overnight in an oven at 60 °C, stirring at 220 rpm.

3.2.2 Cleaning

The obtained sample was ultra-centrifuged to eliminate the excess of polymer. Ultracentrifuge uses high rotation velocities and gradient solutions to separate components of different weights in a sample. In my case, I used water solutions with 20, 40 and 60% molar content of sucrose to create the gradient. Starting from the bottom of the centrifuge tube:

- 2 mL of 60% sucrose solution
- 4 mL of 40% sucrose solution
- 2 mL of 20% sucrose solution
- 1 mL sample

Speed, time and temperature were set at 30’000 rpm, 2 h and 4 °C respectively. Once finished, the sample was collected with the help of a syringe with a long needle and a UV lamp to see the level reached by the sample into the sucrose solution’s gradient. The sample needed to be filtered with a hydrophilic filter (200 nm) and then centrifuged at 3000 rpm 5 times in borate buffer, until it was completely cleaned.

3.2.3 Characterization

The obtained samples were characterized using different techniques to be sure that the process was successful.

- **Electrophoresis** The electrophoresis is the motion of dispersed particles relative to a fluid under the influence of a spatially uniform electric field. It needs the use of a gel. Prepared using Tris/Borate/EDTA buffer (TBE) 0,5 % buffer and 1 % in weight of Agarose, to be poured in a multi-well. The sample was prepared mixing 5 µL of the sample to be investigated with 10 µL of water and 5 µL of the synthetic colored dye, Orange G [104], negatively charged and usually used to monitor the electrophoresis processes.

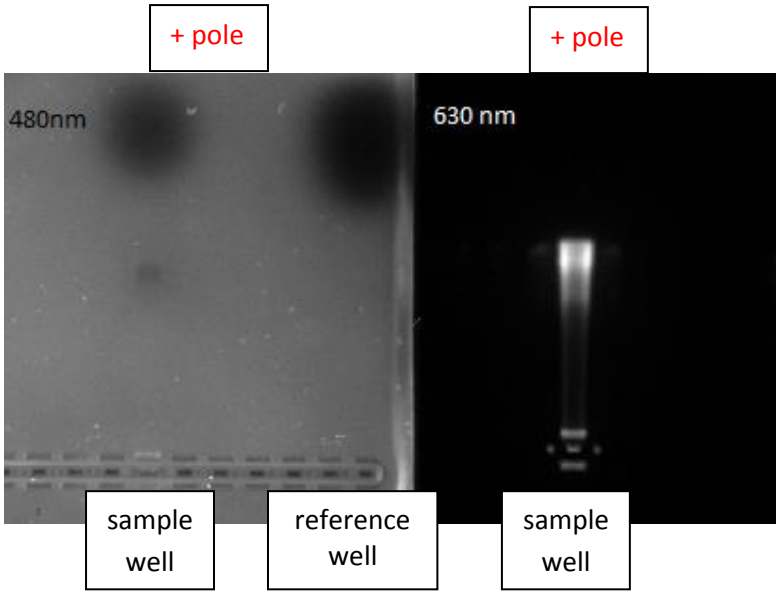

Figure 3.4 An electrophoresis image showing the result of the hydrophilization process, with the polymer represented with the wavelength 480 nm, the nanocrystals with 630 nm.

The sample was put into one of the wells and the instrument was set with a voltage of 100 V and a current of 400 mA for 45 min. The charged sample moved towards the opposite charged pole of the instrument. The smaller is the molecular weight of the element, the more the sample runs towards the opposite charged pole. The lightest element is the marker (OrangeG $_{MW}$ = 452,38 g/mol), whereas the molecular weight of the C-18P is 30000 g/mol. The complex NRs/C-18P will be reasonably heavier. If the ultracentrifugation cleaning process was successful, no polymer should be seen between

the OrangeG marker and the complexed sample positions. The OrangeG and the polymer are visible with 480 nm wavelength: in figure 3.4, left, is clearly visible the ending point of OrangeG run, either in the sample and in the reference well (top of the image). In the right image, the sample run is visible with 630 nm wavelength. Nothing is visible between the position of the sample and the OrangeG: this means that the cleaning process was successful and no free polymer is present in the solution.

- **Dynamic light scattering (DLS)** With a DLS tool is possible to determine the size distribution profile of small particles in suspension (in nm) and their electro kinetic potential (or zeta potential, in mV). Samples were diluted in ultrapure water and if the value of zeta potential was around -40 and -50 mV, the procedure had a positive result.
- **Transmission electron microscopy (TEM)** TEM is a microscopy technique in which a beam of electrons is transmitted through a specimen to form an image. It allows reaching high magnification factors, and it's suitable principally for inorganic samples.

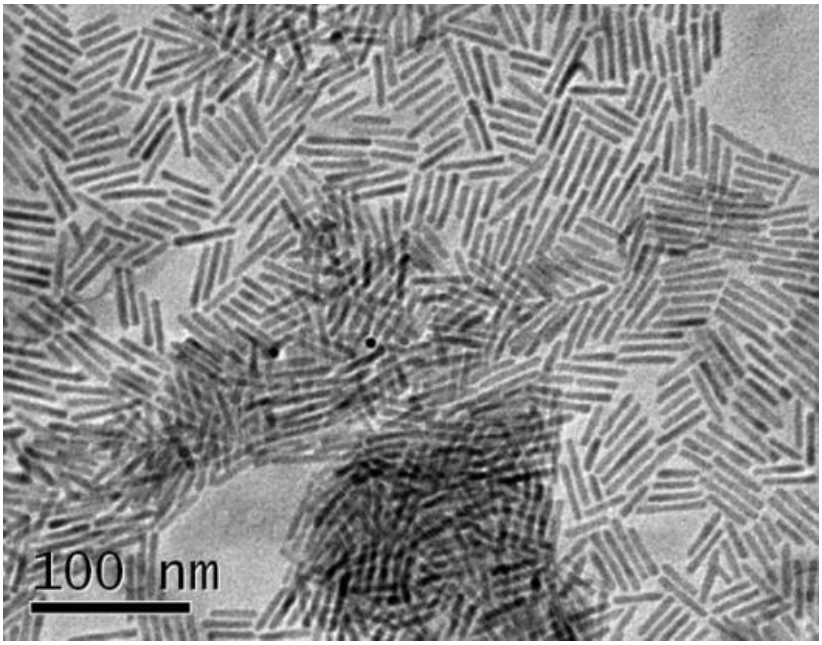

Figure 3.5 TEM images showing the CdSe/CdS nanocrystals in toluene.

The TEM investigation was performed initially to confirm the dimensions of the rods (30x5 nm), and in second place to understand if the polymer coverage of the NRs was successful. The image shows the NRs sample after polymer coating. The absence of a fading halo surrounding the sample confirms the positive result of the process.

- **Inductively Coupled Plasma Mass Spectroscopy (ICP-MS)** Inductively coupled plasma mass spectrometry (ICP-MS) is a type of mass spectroscopy which is capable of detecting metals and several non-metals at concentrations as low as one part in 1015 (part per quadrillion, ppq) on non-interfered low-background isotopes. This is achieved by ionizing the sample with inductively coupled plasma and then using a mass spectrometer to separate and quantify those ions. Using ICP results is possible to quantify the actual concentration of the sample, starting from the concentrations of the single components. The final concentration was obtained using an *in-house* developed software. Taking into account the components of the core, the shape of the particle and its dimensions, the elongation direction of the core seeds and imposing the dilution factor used during ICP inspection, the final concentration of the hydrophilic NRs was $C_{NRs} = 7{,}23\ \mu M$.

3.3 NRs functionalization for the surface charge tuning

After water solubilization NRs were surface-functionalized with different amounts of NH_2-PEG-NH_2 and a tertiary amine (DMEDA), using an EDC cross-linking reaction scheme [105]

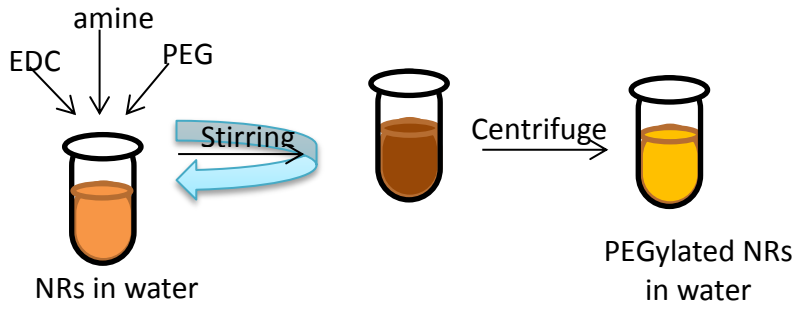

Figure 3.6 Functionalization process for surface charge tuning of NRs.

in order to tune the superficial charge towards more positive values. EDC, DMEDA, PEG and NRs dispersions in water were mixed together and stirred at high speed for 2 hours. The excess was then eliminated by centrifugation and the sample was rinsed in PBS 1X 3 times (every step lasted for 10 minutes, 3500 rpm).

3.4 Polymeric nyle-red encapsulated micelles

Polymeric nyle-red encapsulate micelles were also employed in the experiments involving the cell membranes (Chapter 6). They were fabricated using the same polymer (C-18P) employed to make the NRs hydrophilic (see chapter 3, paragraph 3.2). They were employed in order to eliminate the influence of the semiconductor core from the previously employed NRs. Micelles came in two dimensions (60 nm and 300 nm in diameter) with a fixed $\zeta_{micelles}$ = -24±2 mV. They were made fluorescent by adding nyle-red fluorophore in the preparation procedure (see figure 3.7 for the procedure). Nyle-red is a lipophilic stain that adsorbs at λ = 560 nm and emits at λ = 630 nm (see spectra in figure 3.8).

Sample name	ζ (mV)	EDC/NRs	PEG/NRs	DMEDA/NRs
NR+	+11	5e+05	500	5000
NR-	-24	3e+05	500	1000

Table 3.2 Ratio of molecules of EDC, PEG or DMEDA per number of NR particles used for the tuning of NRs' superficial charge.

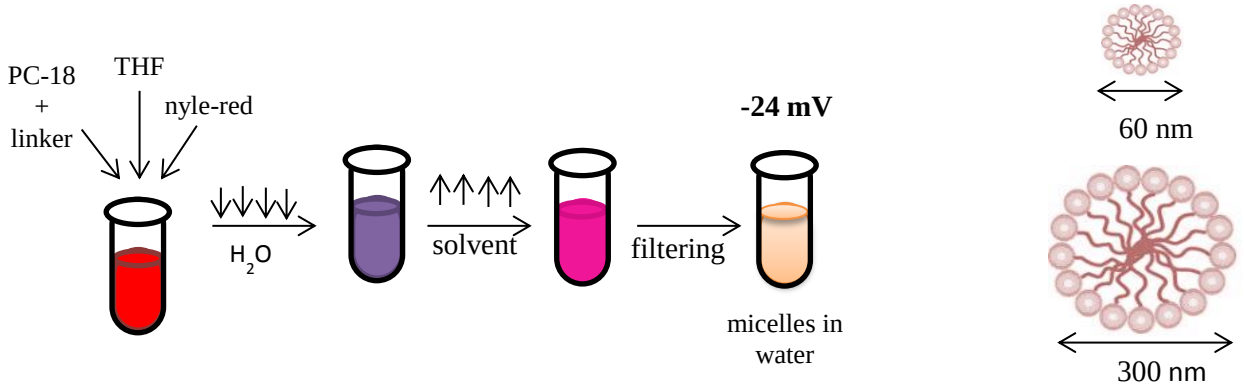

Figure 3.7 Schematic representation of the fabrication procedure of polymeric nyle-red encapsulated micelles.

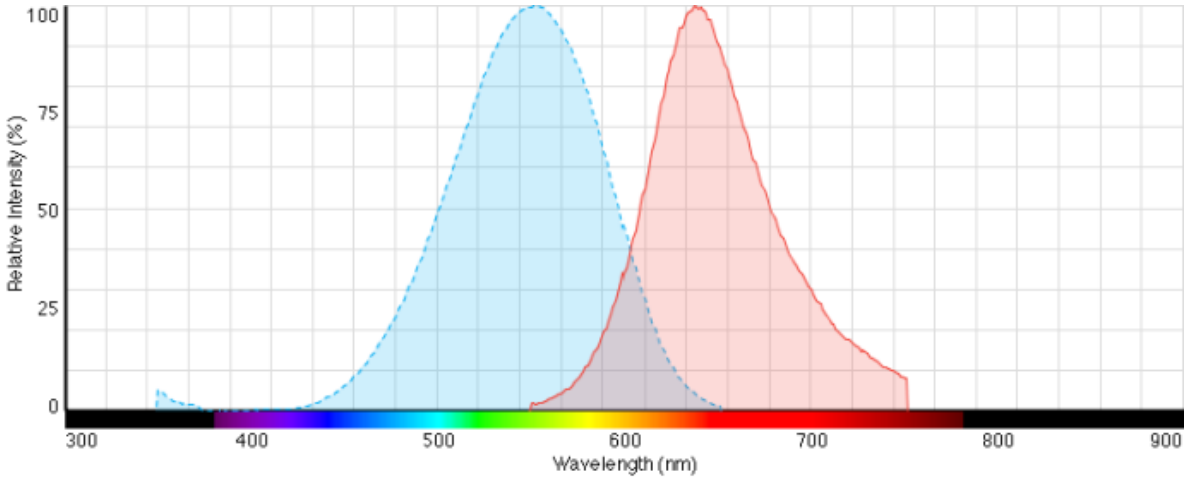

Figure 3.8 Excitation (blue) and emission (red) spectra of nyle-red fluorophore. Image from *www.thermofisher.com*.

Chapter 4
Materials and Methods 2: Membranes

In this chapter, the instrumentation and methods employed during my PhD for the fabrication and characterization of lipid model membranes are described.

4.1 Vesicles preparation

Powdered palmitoyl-oleoyl phosphatidylcholine (POPC), palmitoyl-oleoyl-phosphatidylserine (POPS), 1,2-dioleoyl-3-trimethylammonium-propane (DOTAP) and 1,2-dipalmitoyl-sn-glycero-3-phosphocholine (DPPC) (Figure 4.1) were dissolved in 2:1 vol:vol chloroform/methanol and stored at –20 °C. Proper volumes of the dissolved lipids were mixed in a round bottom glass vial to obtain anionic (-), cationic (+) or zwitterionic mixtures (+/-). In detail, I used for unsaturated lipid mixtures: POPC (+/-), POPC/POPS 90:10 (-), POPC/POPS 75:25 (-), POPC/DOTAP 75:25 (+), POPC/DOTAP 50:50 (+) (all molar ratios). In other mixtures, a molar fraction of DPPC with fully saturated alkyl chains was introduced to obtain POPC/POPS/DPPC 85:10:5 (-), POPC/POPS/DPPC 80:10:10 (-), POPC/POPS/DPPC 70:10:20 (-), POPC/DOTAP/DPPC 45:50:5 (+), POPC/DOTAP/DPPC 40:50:10 (+) and POPC/DOTAP/DPPC 30:50:20 (+) molar ratio mixtures. The solvent was left to evaporate under a gentle nitrogen flux; the vials were then left under vacuum overnight to completely eliminate all of the residual solvent. Vials were weighed before and after solvent evaporation in order to know the exact total amount of lipids (in mg). The lipids were then re-suspended in ultrapure water for mixtures containing DOTAP, and in PBS 1X for the rest in order to obtain 1 mg/mL lipid dispersions, an amount that is optimal for the vesicle extrusion. Lipids were left to hydrate for 20 min then shortly vortexed before being extruded at least 13 times with an Avanti Mini Extruder (Avanti Polar Lipids, Inc.) using 100 nm polycarbonate filters (Whatman, USA) to form unilamellar vesicles dispersions at a concentration of 1mg/mL of lipid. Extrusion was performed at room temperature for unsaturated lipid mixtures and at 60 °C (i.e. beyond the saturated chains lipid Tm) for mixtures containing DPPC. Each vesicle dispersion underwent a size and ζ characterization in a 1.4 mM PBS solution. Sizes were all similar ($\approx$ 100 nm), ζ for every lipid mixture are listed in Table 4.1.

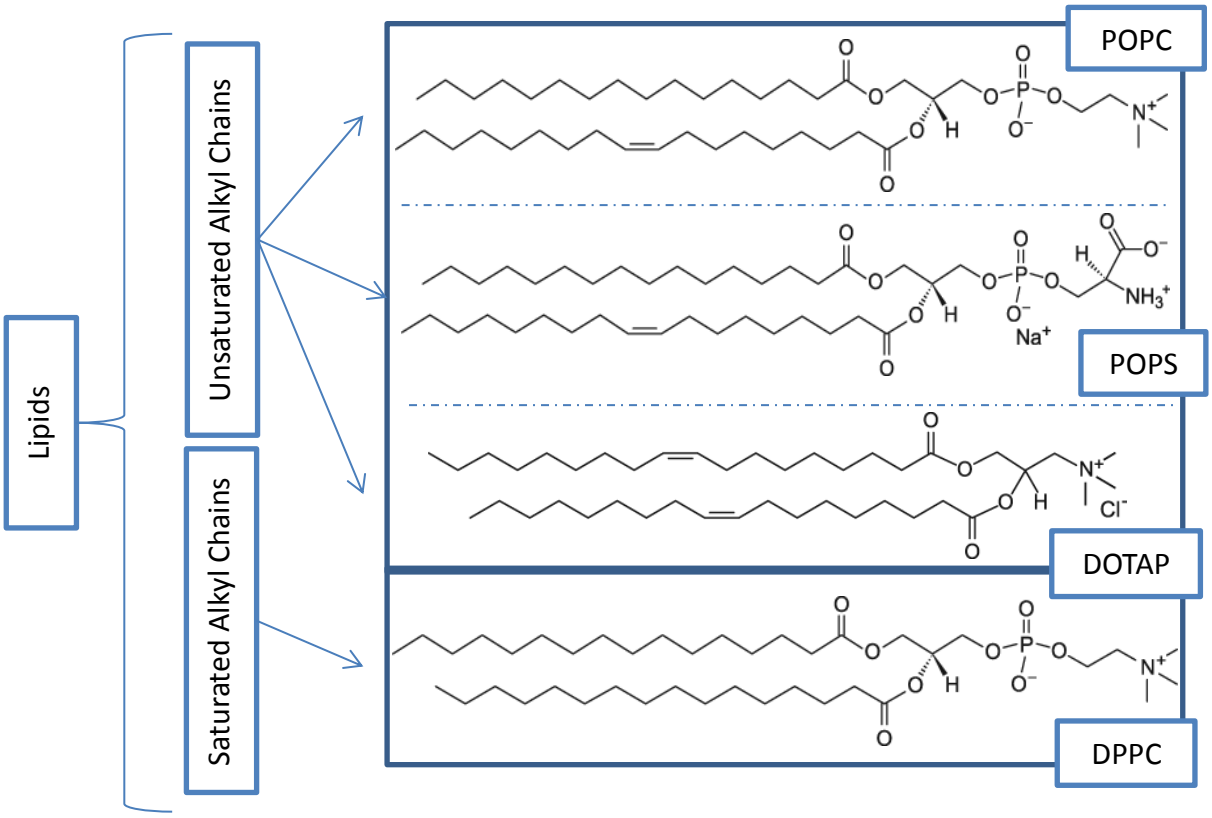

Figure 4.1 Chemical structures of the lipids employed to fabricate the lipid models, divided per saturation level.

Fluid lipid mixtures (mol:mol)	**+/-**	**ζ (mV)**
POPC/POPS 75:25	-	-77 ± 3
POPC/POPS 90:10	-	-54 ± 2
POPC	+/-	-23 ± 1
POPC/DOTAP 75:25	+	13 ± 1
POPC/DOTAP 50:50	+	49 ± 2
Phase separated lipid mixtures (mol:mol:mol)		**ζ (mV)**
POPC/POPS/DPPC 85:10:5	-	-54 ± 2
POPC/POPS/DPPC 80:10:10	-	-54 ± 2
POPC/POPS/DPPC 70:10:20	-	-54 ± 2

POPC/DOTAP/DPPC 45:50:5	+	49 ± 2
POPC/DOTAP/DPPC 40:50:10	+	49 ± 2
POPC/DOTAP/DPPC 30:50:20	+	49 ± 2

Table 4.1 ζ in mV of lipid mixtures studied (positive headgroups +, negative headgroups -, zwitterionic headgroups +/-).

4.2 Quartz Crystal Microbalance with dissipation monitoring

The quartz crystal microbalance with dissipation monitoring (QCM-D) is a tool capable to detect a mass variation per unit area by measuring the change in frequency of its quartz crystal resonator. The resonance is modified by the mass adsorption or desorption at the surface of the acoustic resonator. The QCM-D can be used under vacuum, in gas phase and in liquid environments. In liquid, it is highly effective at determining the affinity of molecules (proteins in particular) to surfaces functionalized with linking sites. Larger entities such as polymers can be investigated too. In my thesis I have exclusively performed experiments in liquid environment.

Common equipment allows resolution down to 1 Hz on crystals with a fundamental resonance frequency of 5 MHz; hence, it is easy to measure mass densities with a sensitivity of 1 ng/cm^2. In addition, the *dissipation factor* is often measured to help analysis. The dissipation factor is the inverse *quality factor* of the resonance, which is the ratio between frequency and bandwidth. It quantifies the damping in the system and is related to the sample's viscoelasticity. The frequency of oscillation of the quartz crystal is partially dependent on the thickness of the crystal. During normal operation, all the other influencing variables remain constant; thus a change in thickness correlates directly to a change in frequency. As mass is deposited on the surface of the crystal, the thickness increases; consequently the frequency of oscillation decreases from the initial value. With some simplifying assumptions, this frequency change can be quantified and correlated precisely to the mass change using the Sauerbray equation [106].

Planar resonators can be operated at a number of overtones. Only odd harmonics can be excited electrically because only these induce charges of opposite sign at the two crystal surfaces. The best agreement between theory and experiment is reached with planar, optically polished crystals for overtone orders between n = 5 and n = 13. On low harmonics, energy trapping is insufficient, while on high harmonics, anharmonic side bands interfere with the main resonance. The resonance frequency of acoustic resonators depends on temperature, pressure, and bending stress. Temperature-frequency coupling is minimized by employing special crystal cuts. A widely used temperature-compensated cut of quartz is the AT-cut.

AT-cut crystals are singularly rotated Y-axis cuts in which the top and bottom half of the crystal move in opposite directions (thickness shear vibration) during oscillation. It has limitations at high and low temperature, as it is easily disrupted by internal stresses caused by temperature gradients in these temperature extremes (relative to room temperature, ~ 25 °C). These internal stress points produce undesirable frequency shifts in the crystal, decreasing its accuracy. As a consequence the AT-cut quartz crystal is most effective when operating at or near room temperature. The quartz crystal is covered by a thin layer of gold, which is the substrate actually coming in contact with the sample. It can be customized and covered with any kind of material. In my thesis, I used SiO_2 covered sensors for the study of the interaction

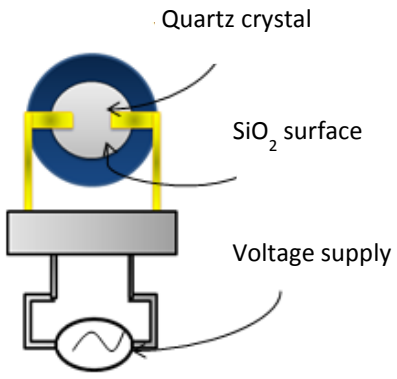

Figure 4.2 Sketch representing a QCM setup.

between nanostructured NPs and proteins with model membranes and gold covered sensors for the study of APA substrates. As I will explain in paragraph 4.2.3, the material of the substrate is very important for the process of vesicle fusion and the formation of SLBs. A typical setup for the QCM-D contains a temperature controller, frequency sensing, an oscillation source and a measurement and recording device (Figure 4.2).

4.2.1 Sauerbrey equation

The Sauerbrey equation was first derived by G. Sauerbrey in 1959 and correlates changes in the oscillation frequency of a piezoelectric crystal with mass deposited on it. He simultaneously developed a method for measuring the resonance frequency and its changes by using the crystal as the frequency-determining component of an oscillator circuit. It describes the frequency shift induced by a thin sample rigidly coupled to the crystal:

$$\Delta m = - C \frac{\Delta f}{n}$$

in which Δm is the mass per unit area that is adsorbed on the sensor, C is the coefficient that describes the sensitivity of the instrument to changes in mass, $\Delta f = f - f_0$ is the shift in frequency and n is the overtone number. It should be noted that the coefficient depends on the crystal properties which, in the case of a sensor with a resonance frequency of 5 MHz, is C ≈ 17.7 $ng \cdot cm^{-2} \cdot Hz^{-1}$.

4.2.2 Quantification of dissipative processes

The bandwidth w quantifies those processes subtracting energy from the oscillation. These may include damping by the holder and ohmic losses inside the electrode or the crystal. The Q-factor (quality factor) is given by

$$Q = \frac{f}{w}$$

where f is the frequency. The "dissipation factor" D, is the inverse of the Q-factor

$$D = Q^{-1} = \frac{w}{f}$$

and gives information about the viscosity of the adsorbed layer; when this value is in the order of $\approx 1x10^{-6}$ is possible to consider the layer rigid and the Sauerbray equation can be used to quantify the total mass adsorbed. If this value is high Sauerbray equation is not valid and alternative methods have to be employed to calculate the adsorbed mass, as the Voigt model [107].

4.2.3 Vesicles fusion process

The process of vesicle fusion on solid substrate in order to obtain a SLB is quite common. QCM-D is the ideal tool to monitor the formation of a SLB, and it has been largely used in the literature for this purpose. In particular, Richter et al. [47] used QCM-D tool to underline the differences in this process due to the use of differently charged lipids or substrate; they showed that negatively charged vesicles (i.e. mixtures containing serine) present a typical trend in the shift in frequency of QCM-D SiO_2 sensor. The initial negative shift in frequency is quite big (typically $\Delta f \approx 400$ Hz for the 7^{th} harmonic) and represents the adsorption of entire vesicles, full of water, on the substrate. Also the increase in D factor is big ($\Delta D > 10^{-5}$), due to the viscoelasticity properties of the entire vesicle.

This step is followed by an increase in frequency and decrease in dissipation, which represents the moment in which vesicle concentration on the sensor's surface reach a critical value at which they fuse in a SLB. The frequency stabilizes at a negative value respect to the beginning of the experiment (indicating the adsorption of material on the sensor's surface) and the dissipation factor will reach the zero value, indicating that the adsorbed layer is rigid and all the water contained in the vesicles has been released (see figure 4.3 A). On the contrary, positively charged vesicles fuse directly in a SLB, as is possible to see in figure 4.3 B, in which the frequency decreases monotonically until a stable value is reached, and no changes can be

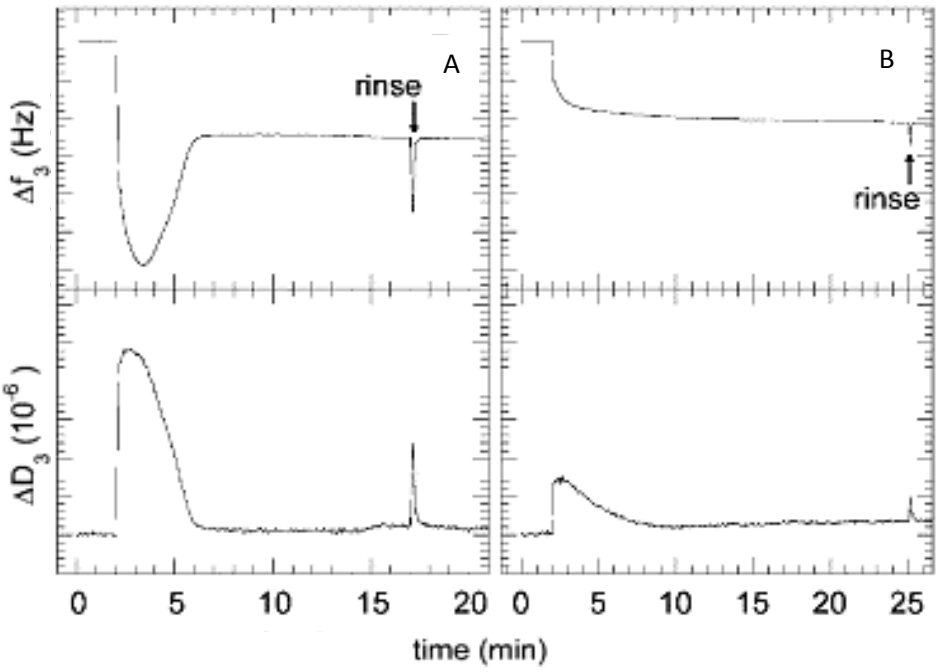

Figure 4.3 Shift in frequency (up) and dissipation (bottom) for A) negatively and B) positively charged lipid on SiO_2 covered QCM-D sensors. Taken from [47].

registered in the D value. Changing the material covering the surface of QCM-D sensor will modify the kinetic of vesicle adsorption. As an example, fabricating a SLB by vesicle fusion using gold as a substrate is not trivial and other shrewdness have to be employed, such as the functionalization of the substrate with self-assembled monolayers of thiols (see attached paper).

4.3 Supported lipid bilayers and QCM-D measurements

SLBs were obtained on quartz crystals sensors covered with SiO_2 (nominal resonance frequency of 5MHz) in a KSV QCM-Z500 QCM-D tool (Biolin Scientific, Gothenburg, Sweden). Every crystal was cleaned by sonication in a 2% SDS solution for 20 min, then rinsed three times with ultrapure water and dried under N_2 flow. To remove any organic contaminants from the surface, the sensors were placed in a UV/Ozone ProCleaner™ chamber (BioForce Nanosciences, Inc., U.S.A.) for 10 min before use.

To prepare the SLB, ultrapure water or PBS 1X buffer was injected into the QCM-D measurement chamber until stability was reached. 2mL of the lipid vesicle solution was then added at a concentration of 0.1 mg/mL to form a stable SLB. The temperature for SLB formation was 22 °C for unsaturated mixtures and 60 °C for mixtures containing DPPC. After it reached stability, the temperature of the SLBs containing saturated lipids was set to 22 °C. POPC, POPC/POPS 90:10 and POPC/POPS 75:25 (mol:mol ratios) LUVs showed the usual SLB formation kinetics after the vesicles had been adsorbed and subsequently fused on the SiO_2 substrate, the same for mixtures containing DOTAP (compare paragraph 4.2.3). The adsorption of entire vesicles on the surface was indicated by a large negative shift in the frequency, i.e., $\Delta f_7/7 \approx -72$ Hz (where $\Delta f_7/7$ is the measured shift in frequency relative to the 7^{th} overtone, normalized by the overtone number), and a dissipation value $\Delta D \approx 12e{+}06$. When the vesicles started to fuse, the frequency decreased until a stable value was reached ($\Delta f_7/7 \approx -26$ Hz) and the dissipation value was close to 0. The fusion process lasted 40 min. For positively charged LUVs, the formation of SLB was faster and there was no adsorption of entire vesicles. However, an SLB was directly formed in 20 min, as was indicated by a $\Delta f_7/7 \approx -16$ Hz and a constant value of $\Delta D = 0$. In the case of SLBs containing DOTAP, there was no full coverage of the sensor's surface, as can be understood by the differences in the $\Delta f_7/7$ at the end of the SLBs' formation process between POPC/POPS 90:10 and POPC/DOTAP 50:50 (mol:mol ratios) (Figure 4.4).

After SLB formation, unattached vesicles were rinsed in either ultrapure water or PBS 1X. Frequency and dissipation change measurements were used to confirm the existence of a stable SLB (compare paragraph 4.2.3) [45, 47, 108] for further investigation with NPs dispersion in water. In the case of POPC/POPS 75:25 mol:mol, POPC/POPS 90:10 mol:mol and POPC, whose vesicles were prepared in PBS 1X buffer, a further rinse with ultrapure water was necessary. After stabilization and a rinsing step, a solution of NPs in ultrapure water (at a concentration of 1 nM for NR-, 5 nM for NR+ and different concentrations for micelles) was injected into the measurement chamber. After 30 min, a final rinsing step with ultrapure water was carried out in order to remove any non-interactive NPs. Changes in the dissipation value

ΔD gave us information about the viscoelastic properties of the adsorbed layer, which is considered rigid for a small value of ΔD. For the quantification of the adsorbed mass of NRs, the Sauerbrey equation [106] was used. For every measurement, the 7th overtone was considered, since it is the most stable among the 11 overtones that were investigated.

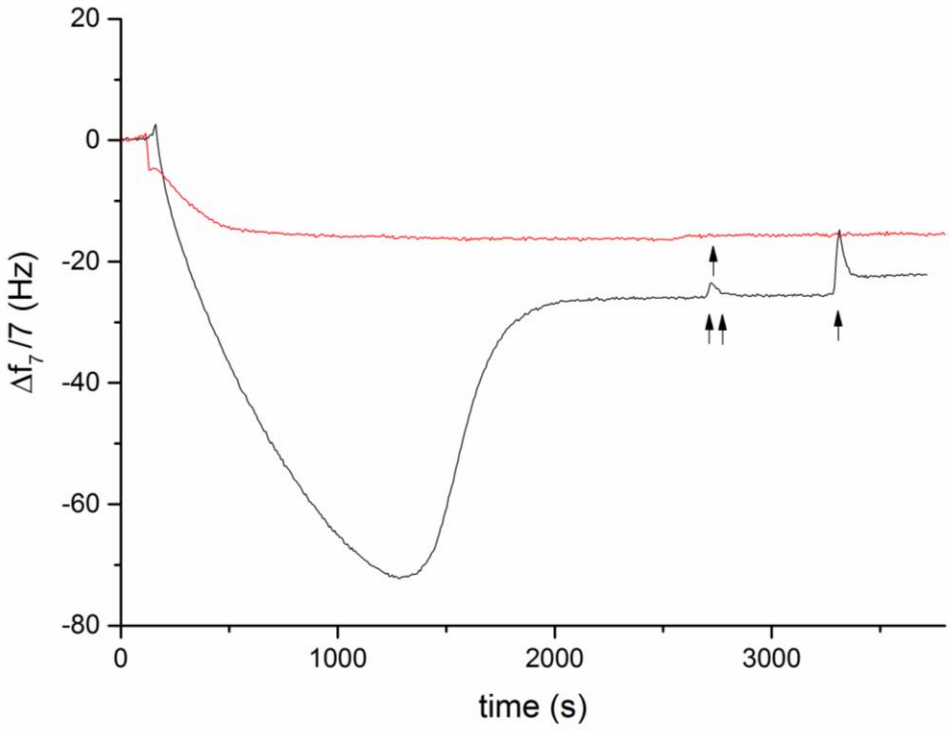

Figure 4.4 Shift of the normalized 7th harmonic resonance frequency of the QCM-D sensor due to: formation of POPC/POPS 90:10 mol:mol SLB (black) and POPC/DOTAP 50:50 mol:mol SLB (red). The single arrow represents rinse with ultrapure water, the double arrow rinse with PBS 1X solution.

4.4 Langmuir-Blodgett Trough

A Langmuir–Blodgett (LB) trough is a laboratory tool that is used to compress monolayers of molecules on the surface of a liquid subphase and measure the surface phenomena due to this compression. It can also be used to deposit single or multiple

monolayers on a solid substrate. The idea of a Langmuir–Blodgett (LB) film was first proven in 1917 when Irving Langmuir showed that single water-surface monolayers could be transferred to solid substrates. 18 years later, Katharine Blodgett discovered that several of these single monolayer films could be stacked on top of one another to make multilayer films [109, 110]. The LB trough's general purpose is to study the properties of monolayers of amphiphilic molecules (e.g. soaps, detergents or lipids). The LB trough allows to prepare a monolayer of amphiphilic molecules on the surface of a liquid, and then compress or expand these molecules on the surface modifying the molecular density, or area per molecule.

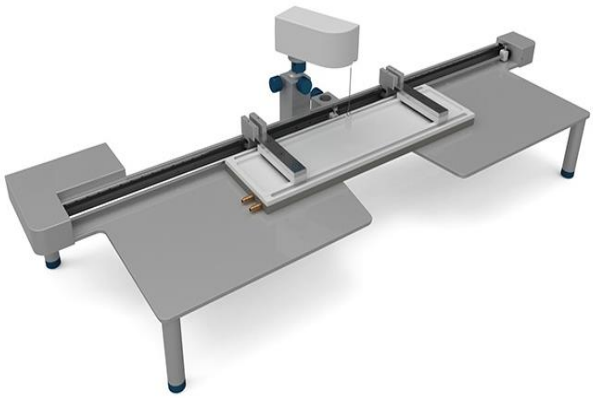

Figure 4.5 A Langmuir-Blodgett trough (from: *www.biolinscientific.com*).

This is accomplished by filling the trough with a subphase (usually water), spreading a amphiphile dissolved in organic solvent over the surface, and then compressing the surface with movable barriers. These barriers are typically made from hydrophobic and chemically inert PTFE (polytetrafluoroethylene), as the trough, to create a meniscus on them that will aid in keeping the molecules inside even in high packing densities.

An important property of the system is its surface pressure π (the surface tension of the pure subphase minus the surface tension of the subphase with amphiphiles floating on surface, see equation 1-1) which varies with the molecular area. The surface pressure – molecular area isotherm (π-A isotherm) is one of the important indicators of monolayer properties.

The surface pressure π is usually measured by the Wilhelmy method, which consists of a plate partially immersed in the liquid connected to an electronic linear-displacement sensor, or electrobalance. The plate can be made of platinum or filter paper presoaked in the liquid to maintain constant mass. The plate detects the downward force exerted by the liquid meniscus which wets the plate. The surface tension calculated is then plotted versus the area per molecule occupied by the single lipid to obtain the π-A isotherm (figure 4.6).

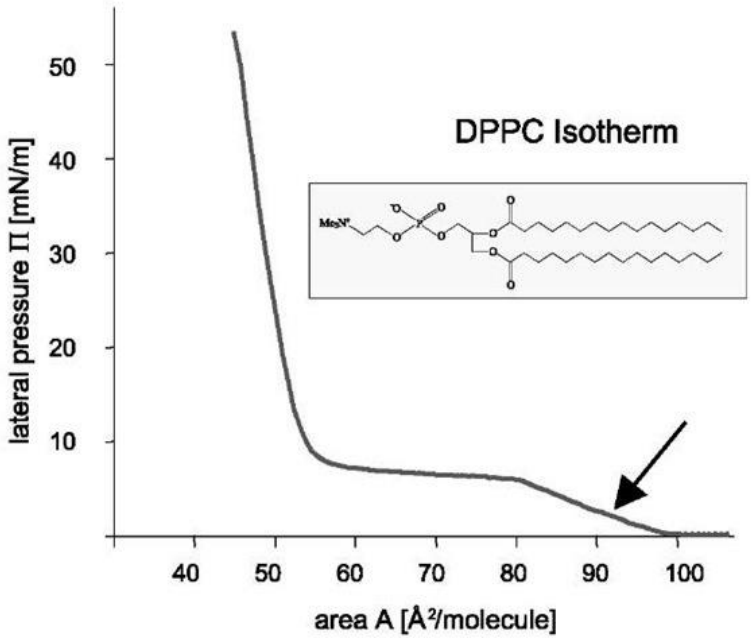

Figure 4.6 Example of Langmuir trough output pressure – area isotherm of a monolayer composed by a saturated chains lipid, DPPC.

In my project, NRs behavior with lipid monolayers was studied using a LB trough.

4.4.1 Compressibility modulus

The evaluation of the compressibility modulus of the lipid monolayer C_s^{-1} can be used to determine how much it is resistant to compression. In general mechanics, it describes the increase in density due to the compression of a substance, and it is directly linked to the mechanical properties of the substance under study. In the case of LMs it can be easily calculated from their π-A isotherm using the first derivative of π on the molecular area that was occupied by the lipids (A). It has been defined as [59, 111] :

$$C_s^{-1} = -A\frac{\partial \pi}{\partial A}$$

The most practical information that C_s^{-1} gives regards the rigidity of the monolayer: a high value of C_s^{-1} indicate that the layer under study is stiff; on the contrary, a low value indicate a soft layer.

4.4.2 Custom made Langmuir trough

I used a custom made trough. This trough was made in PTFE and designed in order to fit on the setup of the mini-trough by KSV NIMA (Bioline Scientific, Sweden) equipped with two

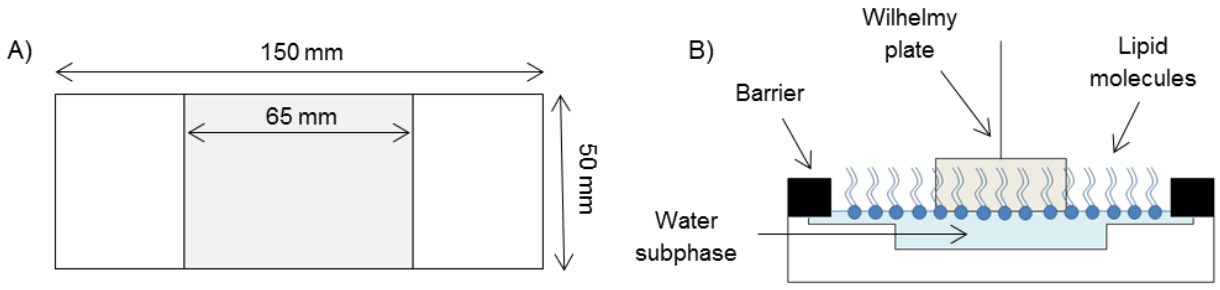

Figure 4.7 A) Sketch of the top view of the custom made Langmuir trough used. The central grey part (65 x 50 mm^2) is 6 mm deep, while the white part is 2 mm deep. B) Sketch of the frontal view of the custom made trough. Objects not in scale.

moving lateral barriers for symmetrical compression, with a central part deeper than the peripheral ones. The trough was fabricated in PTFE. The initial open area of the trough is 7500 mm^2. It is a rectangular trough of 150 x 50 mm, with a central well 65 x 50 mm 6mm deep. The two external regions are 2 mm deep (see figure 4.7). This trough was used in order to minimize the volume of the water phase and decrease the amount of materials needed to perform the experiments (especially the total volume of NPs dispersion).

4.5 Lipid monolayer and surface pressure area isotherms (π-A)

The π-A isotherms were performed to investigate the behavior of NRs with lipid monolayers. 0.3 mg/mL of lipid solutions were prepared in a 2:1 chloroform/methanol mixture. Every solution was stored in the fridge at 4 °C and left at room temperature for a few hours before use. To minimize the risk of changes in the lipid concentration due to the fast evaporation of the solvent, vials closed with Mininert® Valves 15 mm (by Supelco, Bellefonte, PA, U.S.A.) were used. 20 µL of a lipid solution was spread with a Hamilton micro-syringe (10 µL, by Sigma-Aldrich®) at the air-water interface of an ultrapure water subphase or a NR dispersion subphase (the NRs were dispersed in ultrapure water at a concentration of 0.5 nM) in the custom-made Langmuir trough. After spreading the solution, the solvent was left to evaporate for ca. 15 min. The subphase temperature was 20 ± 2 °C. Compression π-A isotherms were then performed at a compression rate of 10 mm/min.

Chapter 5
NPs interaction with model membranes

In this chapter, the results obtained on the study of the behavior of PEGylated CdSe/CdS NRs (which were developed by our group and used in refs [69, 70] and polymeric micelles interacting with model lipid membranes are shown. A systematic study of the interaction between the NPs using different surface charges and SLBs and LMs is described. The surface potential of the model membranes was modulated by changing the membrane composition; mixing zwitterionic lipids with cationic or anionic ones (see Table 4-1). The presence of gel domains in fluid membranes was also investigated by introducing lipids with saturated alkyl chains to the mixtures. Quartz Crystal Microbalance with Dissipation monitoring (QCM-D) technique was used to investigate the SLB and LMs were characterized by performing pressure-area isotherms (π-A) in a Langmuir trough [112]. The results were also interpreted using the DLVO theory.

5.1 Fluid state SLBs and NRs

SLBs made pure of unsaturated lipid chains, fluid at room temperature, were tested with positively and negatively charged NRs.

5.1.1 PEGylated NRs

The NRs' adsorption to the SLB was monitored as a function of the lipid charge by employing fluid state bilayers. The NRs' behavior was also tested on bare SiO_2 substrates, and we discovered that the NR+ were adsorbing on the solid substrate, whereas NR- did not interact with the sensor's surface (Figure 5.1).

After the formation of SLBs, the interaction with both NRs was systematically tested. After the interaction of NRs with SLB ($\Delta D_{NR-} \approx 0.5e+06$, $\Delta D_{NR+} \approx 2.5e+06$), ΔD values were low enough to consider the system as a rigid layer, allowing the Sauerbray equation [106] to be used to calculate the adsorbed mass.

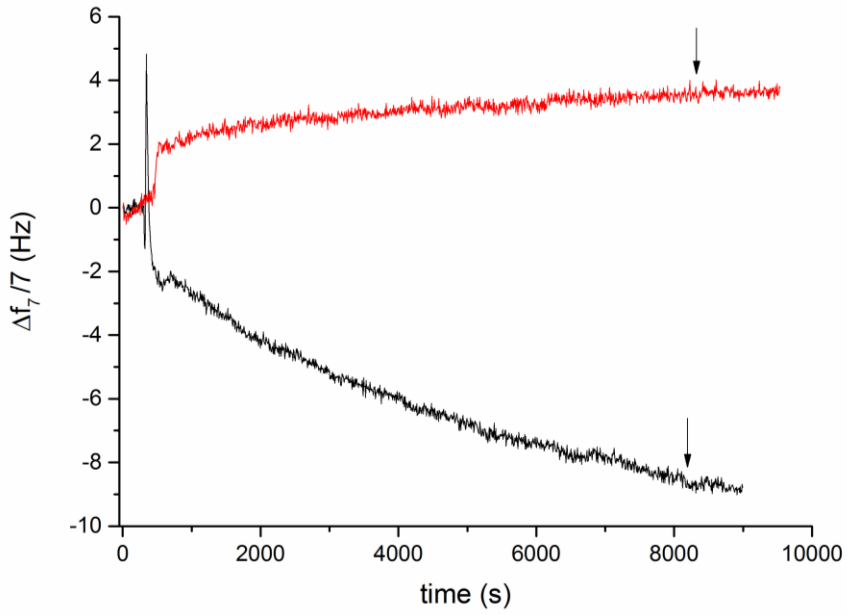

Figure 5.1 Shift of the normalized 7th harmonic resonance frequency of the SiO_2 QCM-D sensor due to the adsorption of NR+ (black line) on bare SiO_2 sensor. NRs- didn't interact with the sensor's surface (red line). The arrow indicates the rinse with ultrapure water.

Figure 5.2 shows the mass of the NRs that was adsorbed on the SLBs as a function of the amount of charged lipids that are present in the mixture. NR- was adsorbed on a positively charged SLB only when the molar percentage of DOTAP in the preparation mixture was 50%. In this case, the difference between the ζ measured for the lipid vesicles that were used for the SLB formation and the ζ measured for the NRs was $|\Delta\zeta_{(\text{POPC/DOTAP 50:50 – NR-})}| \approx 73\pm2$ mV (see Figure 5.3 A). In all other cases, no interaction was observed. NR+, however, was adsorbed on the anionic SLB in the presence of a POPS molar content as low as 10%, showing a Δζ of $|\Delta\zeta_{(\text{POPC/POPS 90:10 – NR+})}| = 65\pm2$ mV. Increasing the molar percentage of the anionic lipid did not increase the adsorbed NR+ mass (ca. 400 ng/cm^2), which apparently reached a saturation value (Figure 5.3 B). Using a SLB with a molar content of POPS of 25%, after the NR+ adsorption phase (corresponding to a frequency decrease) that lasted ca. 30 min, an increase in the frequency shift was registered, while the dissipation value remained constant. This was interpreted as a removal of lipids from the substrate surface. It's important to underline that no adsorption of either NR- or NR+ ($\Delta m \approx 0$) on the zwitterionic lipid bilayer (0% molar of

charged lipids, pure POPC, ζ = -23±1 mV) was registered: the absolute value of the difference between the ζ of the lipids and the ζ of the NRs ($|\Delta\zeta_{(POPC-NR)}|$) is 1±1mV for NRs- and -34±1 mV for NR+. A small decrease in the frequency was also observed for the NR+ that interacted with the positive SLB (both 25% and 50% of DOTAP). This negative Δf is due to the adsorption of NR+ on the bare SiO_2 surface, phenomenon happening in the substrate areas that are not covered by the bilayer, as was previously mentioned.

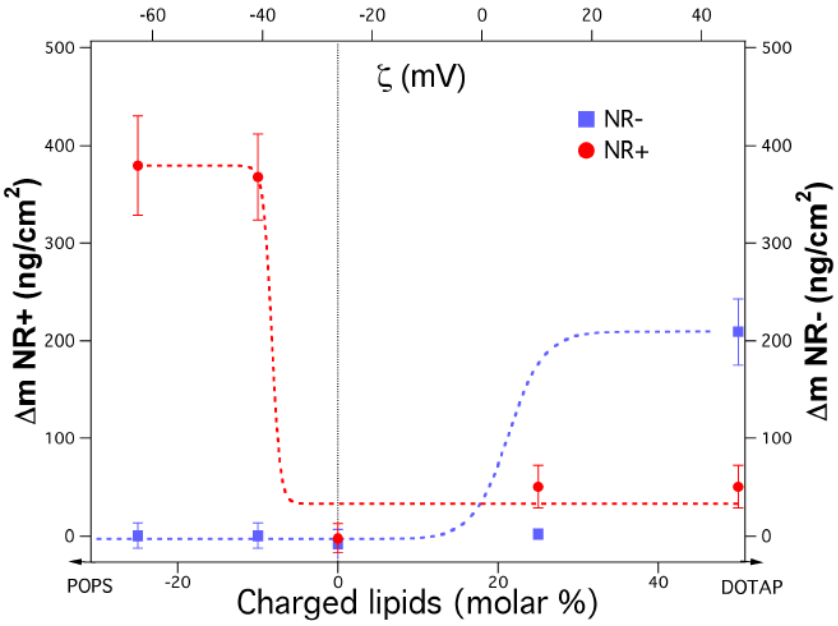

Figure 5.2 Mass adsorbed per unit surface area (Δm) on SLBs due to the interaction of NRs with lipids. Δm is plotted versus the molar percentage of charged lipid in the different lipid mixtures employed. The corresponding ζ is plotted as the top x-axis for clarity. Red circles represent the mass of positively charged NRs with SD, the blue squares represent the same for negatively charged ones. The sigmoid curves (dotted lines) have been plotted so that the correlation between the data points can be easily identified.

Increasing the DOTAP molar percentage in the vesicles, the SLB coverage on the sensor's surface was so small that both NR+ and NR- interacted producing a similar frequency down-shift (data not shown): the NR+ was adsorbed on bare SiO_2 and the NR- was adsorbed by the positive membrane.

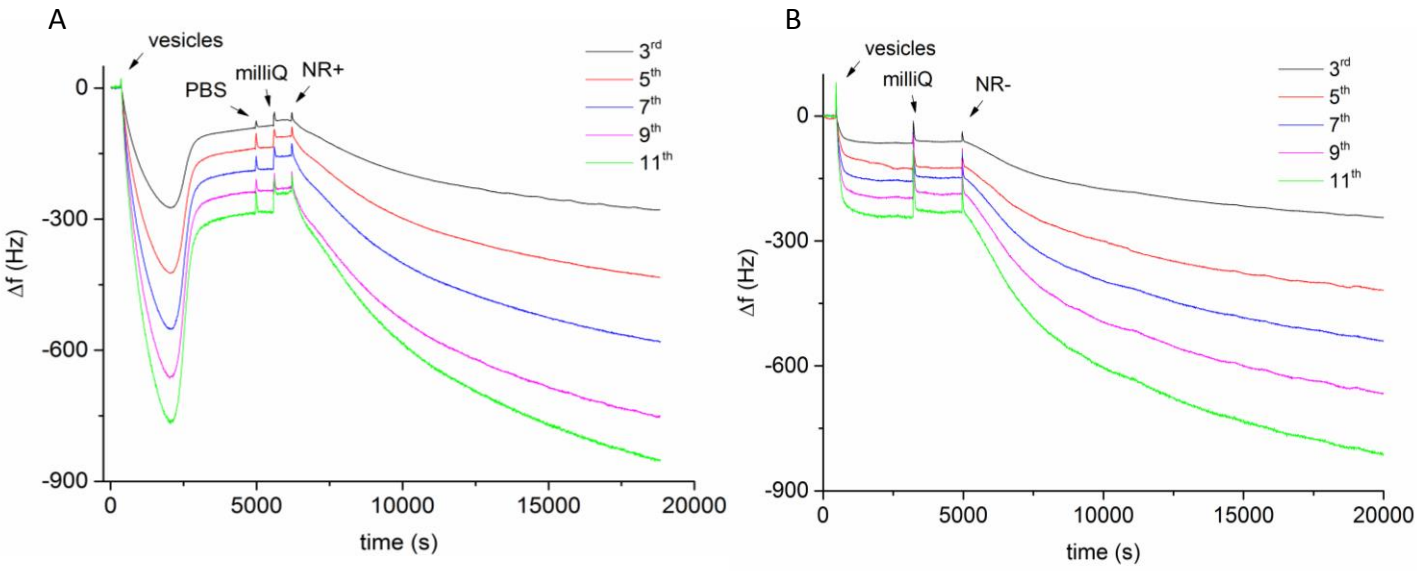

Figure 5.3 Frequency shift of all measured overtones (from 3rd to 11th) for A) POPC/POPS 90:10 mol:mol SLB interacting with NR+ B) POPC/DOTAP 50:50 mol:mol SLB interacting with NR-. NR-.

Summarizing the results, in order to observe an interaction between NRs and fluid state SLBs, not only does the charge of the two objects have to be opposite in sign but a certain $|\Delta\zeta_{(SLB\ -\ NR)}|$ value has to be overcome, e.g., ≈ 70 mV. For lower differences in ζ, no interaction occurs in the cases in which an electrostatic interaction is to be expected (e.g. in the case of POPC/DOTAP 75:25 mol:mol with NR-, ($|\Delta\zeta_{(SLB-NR)}| = 37\pm1$ mV and of POPC with NR- ($|\Delta\zeta_{(SLB-NR)}| = 34\pm1$ mV).

5.1.2 Polymeric micelles

Micelles (that came only with negative surface potential, similar to NR-) were tested with positively charged POPC/DOTAP 50:50 mol:mol SLB. It was observed that a minimum concentration of 5 μM for the small micelles and 25 μM for the large ones was necessary to register an interaction. This concentration is related to the amount of polymer present in the solution, and not to the total number of micelles. In both cases, after an initial phase of

adsorption that lasted for 1 h and 30 min, the micelles destabilized the system leading a detachment of lipids from the surface of the sensor, as it is possible to see from Figure 5.4.

These concentrations were then used as reference value for the testing with cell lines in vitro.

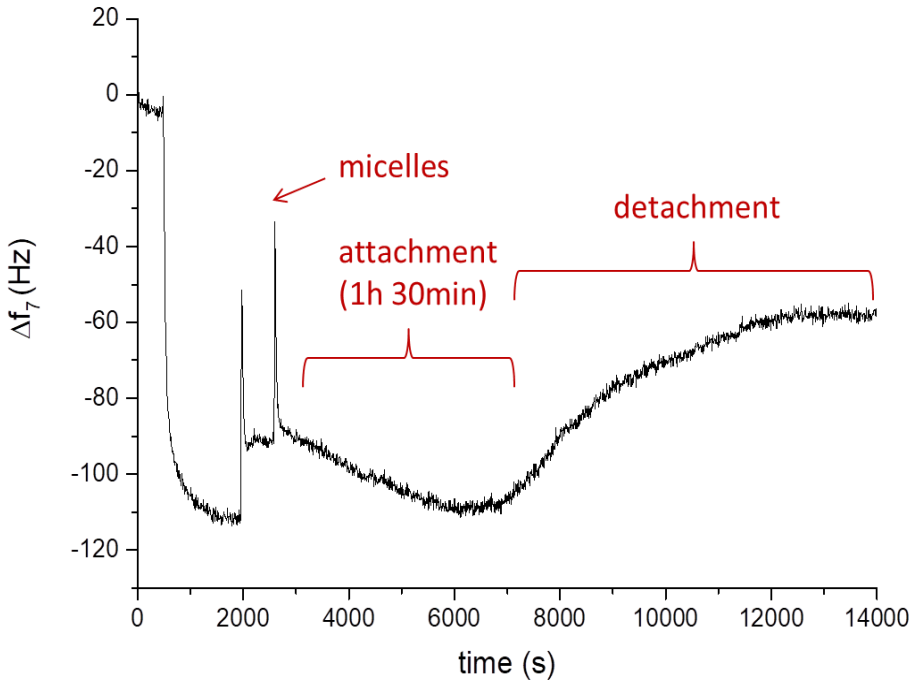

Figure 5.4 Example of micelles behavior with fluid state positive SLB. Small micelles (diameter = 60 nm) are taken into account in this experiment.

5.2 Phase segregated domains SLBs and NRs

After the investigation of the simplest model, made only by lipids that are fluid at the room temperature, the system was made more complex adding saturated chains lipids to mimic the presence of the lipid rafts in the membrane, introducing gel phase domains with different physical properties (especially mechanical) from the fluid bulk. Even the presence of a small amount of saturated lipid in the mixture drastically changed the way in which NRs and lipids interacted. The mixtures that interact with the oppositely charged NRs - as in the unsaturated

mixture study - were modified. 5, 10 and 20% mole of the unsaturated zwitterionic lipid (i.e., POPC) was substituted with a saturated chains lipid with the same hydrocarbon chain length (i.e., DPPC), and the charged lipid molar fraction was kept constant (10% molar POPS or 50% molar DOTAP for anionic and cationic SLB). DLS measurements showed the same ζ values for unsaturated and saturated lipid mixture vesicles at equal anionic/cationic lipid contents (Table 4-1). However, the interaction with the NRs was different in both cases. Figure 5.5 shows the mass of NRs that was adsorbed on the anionic and cationic SLBs, interacting with NR+ and NR- respectively, as a function of the molar percentage of DPPC. In both cases, the amount of NRs that were adsorbed significantly reduced, and quite in the same amount, when DPPC 5 and a 10% molar content were present. No adsorption was registered for a 20% molar content of DPPC. All these data were collected at 22 °C, a temperature at which DPPC is in a solid phase but segregates into a gel phase domain in the fluid lipid matrix that is constituted by POPC and POPS or DOTAP [113].

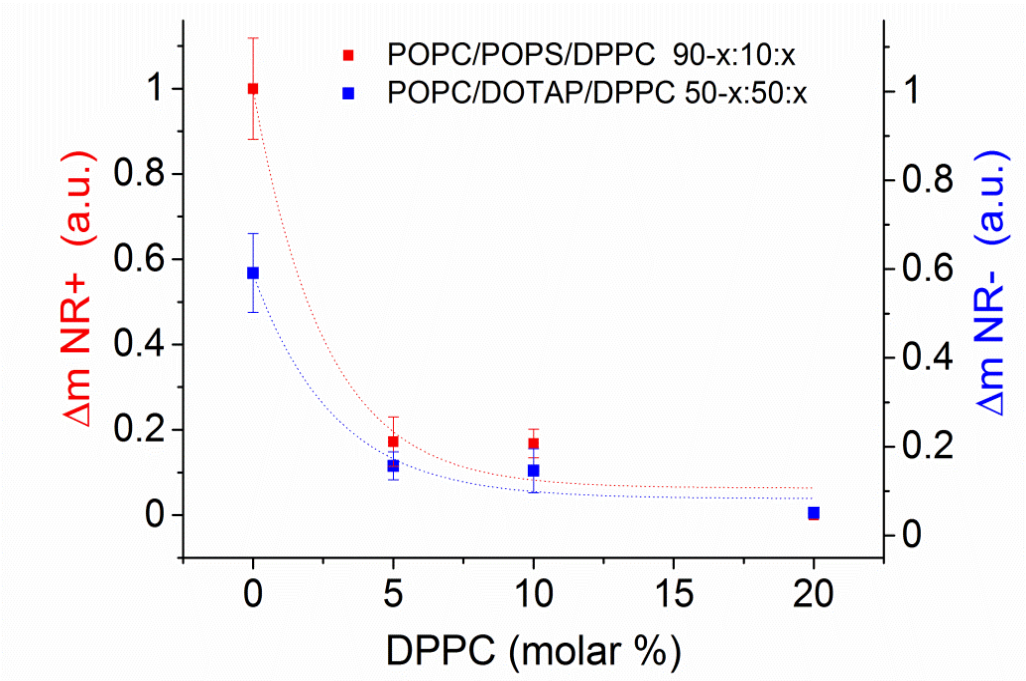

Figure 5.5 Normalized mass of NRs adsorbed on SLBs (Δm) versus the molar percentage of the saturated DPPC in the lipid mixture. Anionic lipid were tested with NR+ (red line), cationic lipid mixtures with NR- (blue line).

These results indicate that not only the charge of the system drives the interaction between the lipid membrane and the NRs, but the membrane composition also plays an important role, since even a small quantity of saturated chain lipids can modify the mechanical properties of the fluid state bilayer creating stiffer zones made of lipids with more compacted hydrophobic chains mimicking the so called lipid rafts in the natural membrane [114], thus inhibiting the interaction with the NRs.

5.3 LMs and NRs

The experiments on SLB were complemented with measurements on LMs on identical systems. Therefore, LMs different in composition were tested with opposite in charge PEGylated NRs. The influence of gel phase domains on the interaction was investigated as well.

5.3.1 π-A isotherms for PEGylated NRs

Having in mind the QCM experiments results, π–A air-water isotherms were performed on the same lipid mixtures that showed a stable interaction with NRs of opposite sign, i.e. POPC/POPS 90:10 and POPC/DOTAP 50:50 (mol:mol ratios) mixtures with NR+ and NR-, respectively. Mixtures containing 10% molar DPPC were also investigated. In Figure 5.6, the isotherms obtained from the NR subphase are reported and compared to the isotherms in ultrapure water. Four different subsequent isotherms were carried out for each sample. POPC/POPS 90:10 mol:mol had a larger lift-off area per molecule (A_{mol}) than POPC/DOTAP 50:50 mol:mol (120 vs 70 $Å^2$/molecule). The collapse pressures (π_{col}) were 47 and 49 mN/m, respectively. In the presence of DPPC, the lift-off A_{mol} was similar for both the anionic and the cationic mixtures (≈ 90 $Å^2$/molecule), whereas the π_{col} were 42 mN/m for the anionic and 35 mN/m for the cationic mixture. In the case of POPC/POPS mixtures, the presence of NR+ in the water subphase led to a left-shift of the isotherm, which was more pronounced for each subsequent compression. The lift-off A_{mol} progressively changed from 120 to 110 $Å^2$/molecule during the subsequent compression cycles, indicating that NR+ strongly interacts with the lipid

head-groups. NR+ alone did not cause any increase in the surface pressure (as NR-), as is shown in Figure 5.7. The left-shifted isotherms and the lower collapse π with respect to the previous curves might indicate a complexation of the serine head-groups with the PEGylated NRs and a progressive removal of lipid molecules from the surface, as is shown in the sketch (Figure 5.6 A).

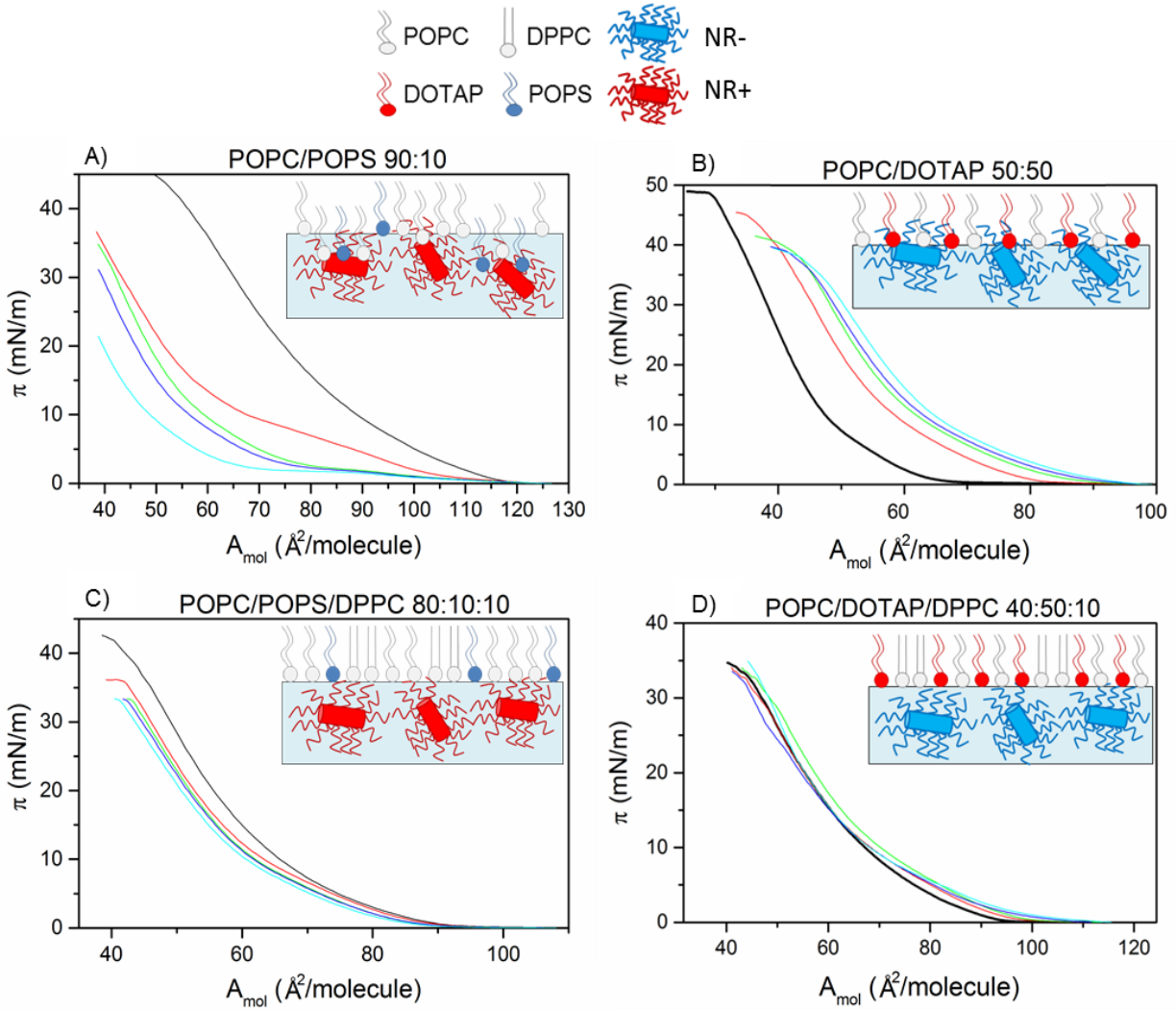

Figure 5.6 π –A isotherms of lipid monolayers interacting with surface functionalized NRs. A) POPC/POPS 90:10 mol:mol B) POPC/DOTAP 50:50 mol:mol C) POPC/POPS/DPPC 80:10:10 mol:mol:mol and D) POPC/DOTAP/DPPC 40:50:10 mol:mol:mol. Black: lipid mixtures in an ultrapure water subphase. Red, green, blue, cyan represent the first, second, third and fourth compressions, respectively, in the NR dispersion subphase.

As in the case of the QCM-D experiments, a strong interaction between NR+ and POPC/POPS 90:10 mol:mol occurred. However, in the case of SLB, the destabilization of the membrane was observed only at a higher POPS content, and this is associated to the lipid removal from the sensor surface. This could be an indication that 1) the ζ of the SLB system is not exactly the same as that of the monolayer due to possible asymmetries [115]; 2) theinteraction in the QCM-D experiment occurs after the SLB has already formed.

The molecular packing could hinder the interaction, considering that the typical surface pressure of a lipid bilayer is $\pi_{bilayer} \approx 30$ mN/m [57], whereas the initial pressure is 0 mN/m in the case of the LMs. For the anionic mixture containing 10% molar of DPPC (Figure 5.6 C), the left-shift of the isotherm is very small but still appreciable, which is in agreement with the QCM-D measurements. In this case, less NR+ adsorbed on the bilayer: NRs are attracted by the oppositely charged lipids towards the surface but the lateral packing between the lipid molecules prevents the insertion of polymer coated NRs between the lipids.

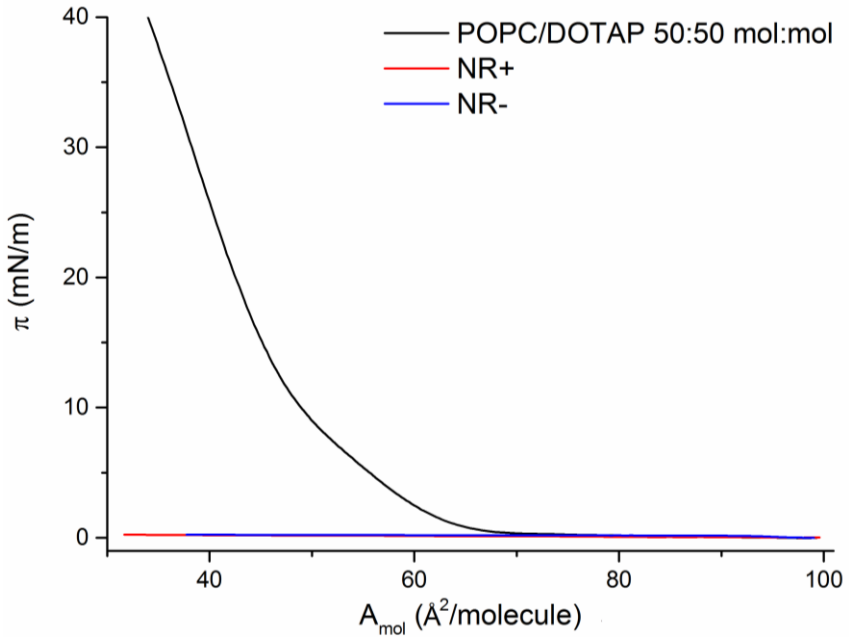

Figure 5.7 π–A isotherms for NRs+ and NRs- in water subphase. POPC/DOTAP 50:50 mol:mol isotherm is shown as a reference.

For cationic monolayers, the interaction with NR- causes a progressive right-shift of the isotherms upon subsequent compressions, suggesting that the NR- (or of their polymer coating) interacts with the lipids and causes an increase in the area per molecule (Figure 5.6 B) (the lift-off area increases from 70 to 95 $Å^2$/molecule during four subsequent compressions). As in the previous case, this effect is strongly hindered by the presence of DPPC (Figure 5.6 D), and only a negligible right-shift of the isotherm is visible at low surface pressure.

As in the QCM-D measurements, the monolayer isotherms were greatly modified in the presence of PEG-amine functionalized NRs in the case of unsaturated lipid mixtures, while very small changes in the mixtures containing DPPC were detected.

5.3.2 Compressibility modulus evaluation

The most relevant changes in the investigated parameter took place in the unsaturated lipid mixtures: in the presence of pegylated NRs, the monolayer becomes softer for POPC/POPS 90:10 mol:mol LM (a decrease in the compressibility modulus (C_s^{-1}) can be seen in Figure 5.8A) but it becomes more rigid for POPC/DOTAP 50:50 mol:mol (an increase in the C_s^{-1} can be seen Figure 5.8B). The differences in the C_s^{-1} in the presence of DPPC were practically negligible, as is to be expected (see Figure 5.8 C and D). The softening of the 10% molar POPS mixture confirmed the presence of fewer molecules at the interface. The interaction takes place at a low π and it is represented by a change in the curve trend in the window between 0 and 9 mN/m: instead of the C_s^{-1} growing in a monotone manner, as it does in the ultrapure water subphase case (in black), it shows a local maximum at 4mN/m followed by a minimum at 9mN/m in the NR+ dispersion subphase (in red). The presence of a local minimum at 9 mN/m is an indication of a possible phase transition in the system; at higher π the trend was similar to the curve obtained on ultrapure water, but at a slightly lower values.

As a result of the decreasing number of molecules at the interface, it was not possible to reach a collapse value in the NR+ dispersion subphase. Adding DPPC to the mixture, the local minimum at 9 mN/m was less pronounced and, at a higher π, the curve was identical to the curve on the ultrapure pure water subphase. This result agrees with the QCM-D measurements,

which demonstrated that the presence of DPPC hindered the interaction between the NRs and the lipids. Regarding the POPC/DOTAP 50:50 mol:mol mixture, no considerable differences were registered between the curve obtained in the presence or in the absence of NR- in the subphase when a low surface pressure range (π = 0-13 mN/m) was used (there was a decrease in C_s^{-1} of $\approx$ 5 mN/m).

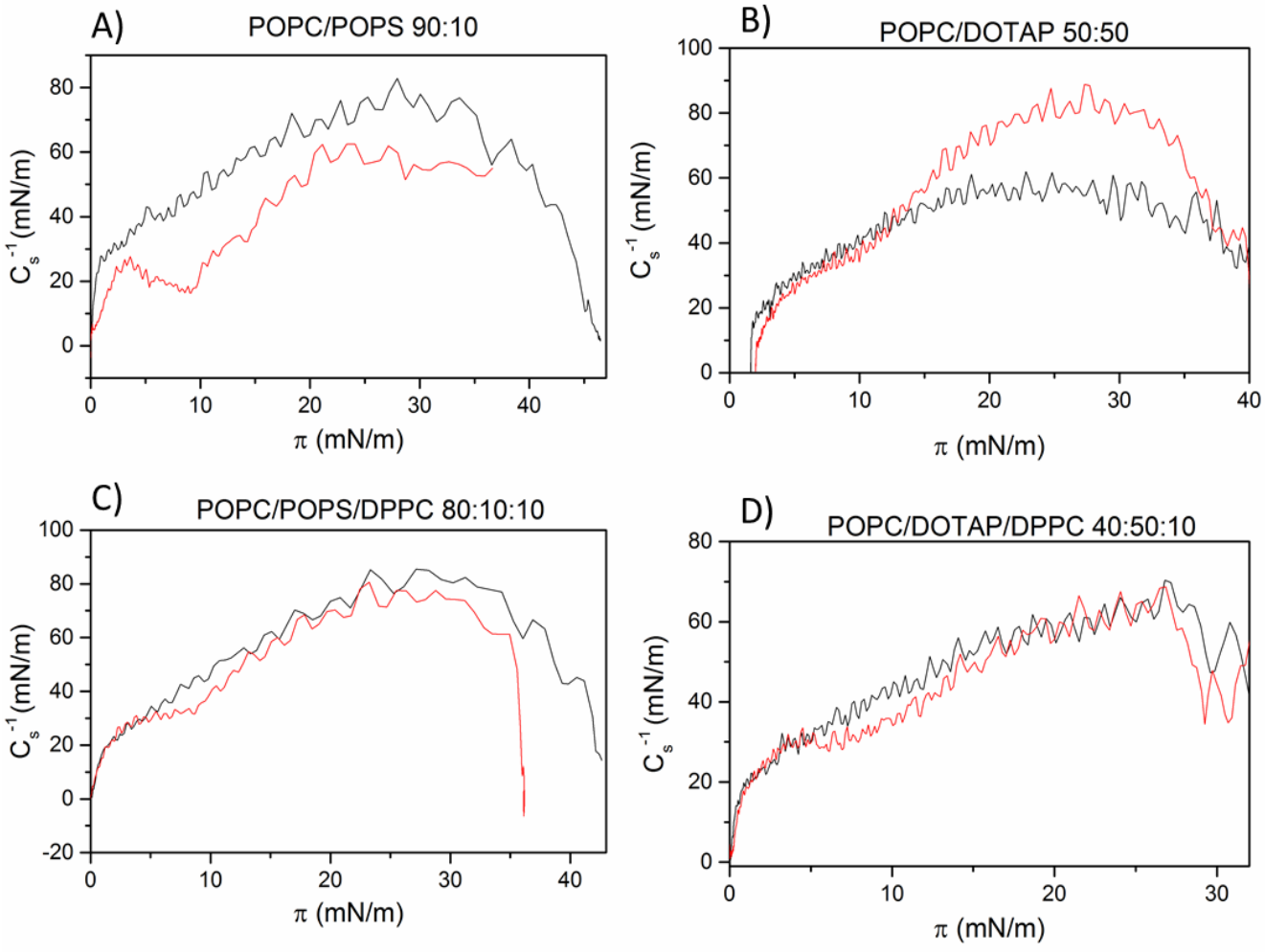

Figure 5.8 Compressibility modulus of LMs C_s^{-1} versus their surface pressure π. Black: LMs in ultrapure water subphase. Red: LMs in NR dispersion subphase. A) and C) are anionic mixtures with NR+, B) and D) are cationic mixtures with NR-. All lipid compositions are in molar ratio.

However, when higher pressures were reached, C_s^{-1} in presence of NRs is higher, indicating an increase in the rigidity of the monolayer due to the insertion of NR-functionalization molecules between the lipids. When DPPC was added to the mixture, values at very low pressures (π = 0-4.5 mN/m) and high pressures (π = 16.5-33 mN/m) remained unchanged. There were small differences in the middle range of pressures of about 8 mN/m, which is comparable with the decrease registered in the unsaturated mixture.

5.4 DLVO theoretical model

The Derjaguin, Landau, Verwey and Overbeek (DLVO) theory explains the aggregation of aqueous colloidal dispersions and describes the forces of interaction between a charged surfaces. DLVO theory is routinely applied to predict the colloidal stability of NP dispersions by summing the electrical double layer of two surfaces and the Van der Waals interaction. A particle-plate interaction model to describe the interaction between NPs and a lipid bilayer was used, following the approach described by Mikelonis et al. [116]. The electrostatic interactions, which can be described by a screened Coulomb potential, dominate at large separation distance and are sensitive to the electrolyte concentration; the van der Waals interaction dominates when the gap between the surfaces is small. The size of the particle was set to the average hydrodynamic size of the NRs. ζ values for the supported lipid membrane (which were estimated by the corresponding values that were obtained for liposomes in bulk, see Table 4-1) and NRs (measured, see Table 3-2) were used. The electrostatic interaction was calculated at a constant potential or constant charge approximation according to the following equations:

$$V_{R,pf,CC} = \pi\varepsilon_0\varepsilon_r a_p \left\{ 2\Psi_{d_f}\Psi_{d_p} \ln\left[\frac{1+e^{(-\kappa s)}}{1-e^{(-\kappa s)}}\right] - \left(\Psi_{d_f}{}^2 + \Psi_{d_p}{}^2\right)\ln\left[1-e^{(-2\kappa s)}\right]\right\} \quad (5.1)$$

$$V_{R,pf,CP} = \pi\varepsilon_0\varepsilon_r a_p \left\{ 2\Psi_{d_f}\Psi_{d_p} \ln\left[\frac{1+e^{(-\kappa s)}}{1-e^{(-\kappa s)}}\right] + \left(\Psi_{d_f}{}^2 + \Psi_{d_p}{}^2\right)\ln\left[1-e^{(-2\kappa s)}\right]\right\} \quad (5.2)$$

$$\Psi = \frac{4k_BT}{ze}\tanh^{-1}\left(\tanh\left(\frac{ze\xi}{4k_BT}\right) \times e^{-\kappa d}\right) \quad (5.3)$$

$$V_{A,pf} = \frac{Aa_p}{6s}\left(1+\frac{14s}{\lambda}\right)^{-1} \quad (5.4)$$

Equation (5.1) holds in the case of constant potential approximation. Equation (5.2) was used to model the constant charge approximation [116]. Equation (5.3) was used to convert the measured ζ into an estimated surface potential using the Gouy-Chapman model. In each of the formulae, ε represents permittivity, a_p represents the particle size, *s* represents the separation distance, Ψ represents the surface potential, κ represents the Debye length and ξsimbolized the zeta potential of the NP.

The van der Waals interaction dominates when the gap between the surfaces is small. It is also rather insensitive to the concentration of the electrolytes, and it is obtained by using the Hamaker theory (see equation (5.4), in which *s* represents the separation distance, A is the Hamaker constant, and λ is the characteristic wavelength of the interaction). Typically, a value of 100 nm is used for λ [117].

The value of the Hamaker constant is a source of uncertainty in the van der Waals energy calculation. In literature, the Hamaker constant of the core material is often used, regardless of the outer stabilizing agent [118, 119]. On the other hand, it is recognized that steric and electro-sterically stabilized particles require a different effective Hamaker constant.

Here, the Hamaker constant was set to 1.62 10^{-20} J, and was calculated as $(A_{11}A_{22})^{1/2}$ in which A_{11} is the Hamaker constant value for the PEG-H_20 interaction (7.2 10^{-20} J) [120] and A_{22} is the Hamaker constant for the lipid bilayer interaction (3.65 10^{-21} J) [121]. All the calculations have been performed using the Igor Pro, Version 6.1, Wavemetrics platform.

5.4.1 DLVO simulations

The interaction between charged NPs and lipid bilayers of various compositions was simulated in the DLVO approximation, and an interaction between a flat plate and a particle was considered [116]. Among the different DLVO approximation methods (constant potential, constant charge, linear superimposition approximation), we chose to use a linearized Poisson-Boltzmann approximation at a constant potential or constant charge between the flat plate and the particle. The results are displayed in Figure 5.9. The interaction energy profiles showed that NR+ (Figure 5.9 A) are attracted by negatively charged bilayers (i.e., POPC/POPS mixtures). The interaction is strongest for POPC/POPS 75:25 mol:mol, which is the membrane with the most negative ζ. Repulsion is predicted between NR+ and POPC/DOTAP. These results are to be expected, and they are in line with the experimental findings (i.e. with the QCM-D results which showed NR accumulation and interaction with LM). However, the model also predicts an attraction to a POPC bilayer, which is different from what was experimentally observed. Therefore, in this case, the repulsive interaction that occurs is higher than the one that was predicted by the model. The same holds for the mirror system, in which NR- interacts with positive membranes (Figure 5.9 B): for both the highly positive lipid system (POPC/DOTAP 50:50 mol:mol) and the most negative lipid system, attraction and repulsion were predicted, respectively, but the model failed to predict the experimental results for the intermediate case (i.e., POPC/DOTAP 75:25 mol:mol). When the potential barrier is low, the data is in accordance with the predictions only using an approximation different from the constant potential one, i.e. in the model of constant charge approximation, which however overestimates the potential barrier [116]. The results indicate that an additional repulsive potential such as a steric interaction and/or hydration force [122] plays a role in the short-range NR/lipid interaction. The non-DLVO interactions are enhanced when saturated chains are present in the

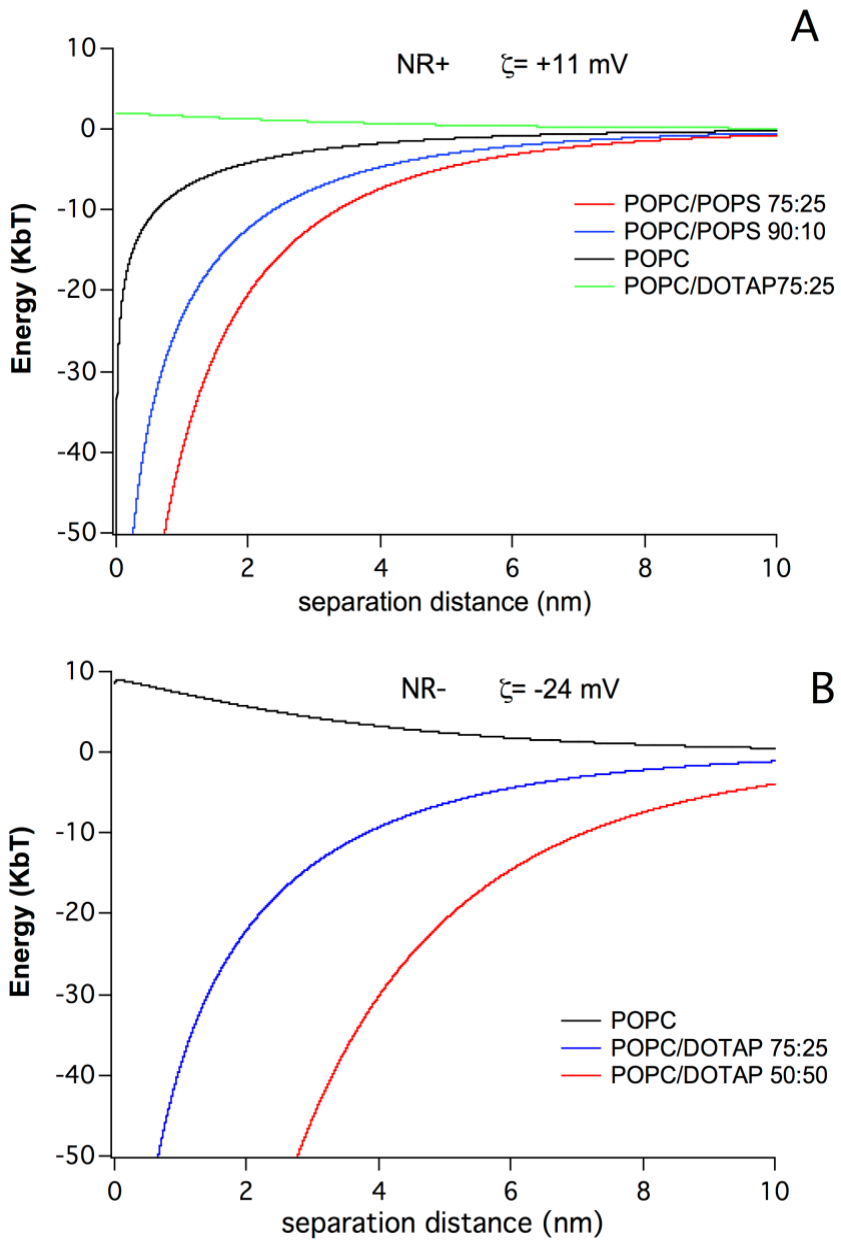

Figure 5.9 Simulations of the lipid bilayer – nanoparticle interaction in the DLVO approximation at constant potential. A) The interaction of NR+ with the membrane of different compositions is attractive for POPC/POPS 75:35, POPC/POPS 90:10 (mol:mol ratios) and for the zwitterionic POPC; repulsion is obtained for a positive membrane POPC/DOTAP 75:25 mol:mol B) The interaction of NR- is attractive in the case of lipid bilayers containing DOTAP and repulsive for a zwitterionic POPC membrane.

membranes and in the associated DPPC gel domains, as is clear from the QCM-D and Langmuir results. It should be noted that the ζ of the lipids applied in the model calculation is measured from the vesicle dispersion therefore it might not represent the actual potential of the bilayer, for instance, due to pure geometrical reasons or to an internal rearrangement of the charged lipids, resulting in an asymmetric bilayer. Further, equations (5.1) and (5.2) hold for spherical particles.

5.5 Conclusions

In the first part of my PhD project, I investigated the interactions between negative NRs (NR-, ζ=-24 mV), amphiphilic polymer coated micelles (ζ=-24 mV) and positive NRs (NR+, ζ = +11 mV) and lipid model membranes made of POPC, POPS, DOTAP and DPPC mixed at different molar ratios as a function of the membrane charge and gel phase presence.

The majority of literature on this topic [55, 76-78] concentrate on the interaction of spherical nanoparticles with cellular or model membranes; my investigation offers information on the interplay between nanorods and membranes, of which there has been little to date.

Supported lipid bilayers and lipid monolayers, either in a fluid phase or in the presence of gel phase domains, and lipid multilayers were considered as models. The results have indicated that there is a fine interplay between the properties of the PEG-amine complex that was used for the functionalization of the NRs and the lipids.

In fluid phase bilayers the difference in the zeta potential between the bilayer and the nanoparticle (PEG-functionalized NRs and polymeric micelles) drives the interaction. It occurs only when a difference of at least 70 mV exists (POPC/POPS 90:10 mol:mol with positive NRs, POPC/DOTAP 50:50 mol:mol with negative NRs and micelles). Svedhem et al. [78] performed a similar study on fluid state lipid bilayers with different compositions and superficial charges, observing that the interaction of un-functionalized spherical TiO_2 nanoparticles is modulated by the charge of the lipid system. Comparing the results with those obtained with neuronal cultures [70], also in that case (in which only highly negatively charged NPs were interacting with the membrane) the interaction was allowed beyond a zeta potential

threshold. Neurons have been known to have action potential, varying their membrane potential from highly negative to positive values. Probably, during this dynamic change and when the membrane potential turns positive, the NPs interact. Here, we calculated this threshold using a model system. In the next chapter, I'll investigate the behavior of the above mentioned NPs with different cell lines to compare with the models.

According to the DLVO simulations, however, adsorption is also expected for lower values. Therefore, non-DLVO terms play a role in the interaction, which is not purely driven by electrostatic and van der Waals forces. This is further supported by the observation that a molar content of saturated lipids as small as 5% severely decreases the amount of NRs that are adsorbed on the bilayer, although the overall charge is constant. Granick et al. [80] explained the correlation between the presence of nanoparticles and the change in head-groups in lipid vesicles, inducing gelation in fluid membranes or fluidizing full gel state ones. In our case, the steric hindrance, which occurred due to the nano and micro gel phase domains, might inhibit the interaction, thus preventing adsorption and state modifications. Again, we can speculate on our results as an explanation of the non-interaction between NPs and glial cells, which can be modeled by our static negatively charged lipid bilayer. In the presence of gel phase domains low or even no interaction was registered, as in the glial cells [70]. This can explain that a situation of dynamic potential changes is necessary to induce the adsorption on NPs onto the membrane, as it happens during the action potential of the neurons.

The lipid monolayer investigations indicate that either a removal of lipids or an accumulation of NRs at the interface may occur, regulated by the PEG-amine/lipid group interaction. This finding highlights the importance of the polymer coating for fine tuning the interaction, which is in line with literature. Barros-Timmons at al. [81] investigated the behavior of lipid monolayers with coated NPs and with the coating alone. They showed that when there is an interaction with an oppositely charged NP, the functionalization alone will induce the same reaction. In these experiments, removal and accumulation events were confirmed by an evaluation of the monolayer's compressibility modulus, which showed variations in the rigidity of the system due to the interaction with the NRs, i.e. softening in the

anionic monolayer interacting with positive NR and stiffening for cationic monolayers with negative particles. Furthermore, we confirmed the inhibition of these phenomena due to the presence of saturated chain lipids in the mixture. This suggests that other properties, such as the rigidity of the lipid systems, are also important in preventing/allowing NR-membrane interaction. The results of the DLVO simulation fully support this fact, since they demonstrate that the interaction is not explained by only considering the electrostatic and van der Waals forces. Therefore, in order to predict and tune the application of NPs, a fine tuning of the membrane/NP interface is necessary in terms of the overall charge and mechanical properties.

During my experiments with synthetic model membranes, NPs were dispersed in pure water. This could be seen as a simplification that could lead too far from the biological studies (in cell medium, the presence of ions and proteins could interfere with the interactions NPs-membrane [123, 124]). Initially, tests started with NPs dispersed in PBS 1X and TRIZMA buffer (from Sigma Aldrich), but no interaction was registered with any system (data not shown). Realistically, the ions present in the buffers caused a shield-effect for the superficial charge of the NP, which was not enough to trigger an interaction. The purpose of this work was to analyze the behavior of the system membrane-NPs related to the charge properties, so we decided, at least for the synthetic model part, to use only pure water to prepare NPs dispersions.

Chapter 6
NPs interaction with cellular membrane

In this chapter, the results obtained on the interaction between three different cell lines and NPs are shown. After the study of the interaction on static potential model membranes and NPs, described in the previous chapter, I investigated the interaction between the same NPs and different cell lines (having either static or dynamic membrane potential) to better understand the role of the surface potential in short-term interactions, avoiding long time of interaction which would imply possible endocytosis. The cell lines employed are: primary postnatal hippocampal mouse neurons, mouse neuroblastoma (N2a) and Chinese hamster ovary (CHO) cells. Neurons are known to be characterized by the so called *action potential*, an electrical spike that changes the membrane potential from negative resting values to more positive ones [125, 126] (Figure 6.1). N2a is a peculiar cell line capable to differentiate into neuronal-like cells in certain condition (i.e., if incubated 48 h in retinoic acid [127]). Once differentiated, they show action potential as neuron, although weaker [127].

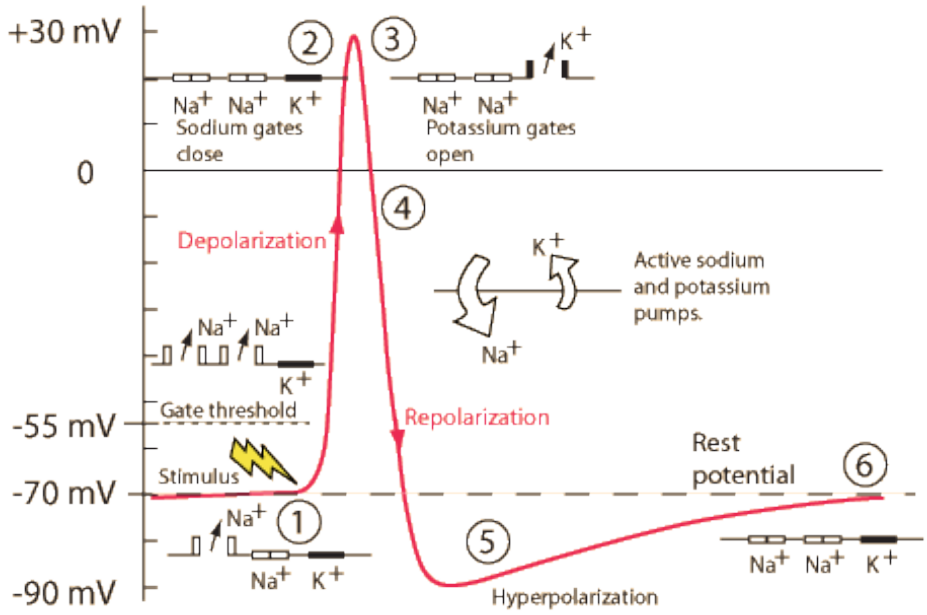

Figure 6.1 Action potential sketch, with representation of ionic channels role in every step. Taken from *hyperphysics.phy-astr.gsu.edu.*

CHO is an epithelial cell line, with a static negative membrane potential. All this cell lines were incubated with NRs and polymeric micelles, and investigated by scanning laser confocal microscopy technique. Tetrodotoxin (TTX) neurotoxin was used to disturb the natural behavior of neuronal cells, inhibiting the *action potential*. TTX is a potent marine neurotoxin (see figure 6.2) naturally carried by some species like pufferfish or porcupinefish and infecting bacteria as *Pseudoalteromonas*, TTX is responsible for many human intoxications and fatalities every year: it inhibits the sodium channels inducing paralysis, and in many cases heart failure and consequently death.

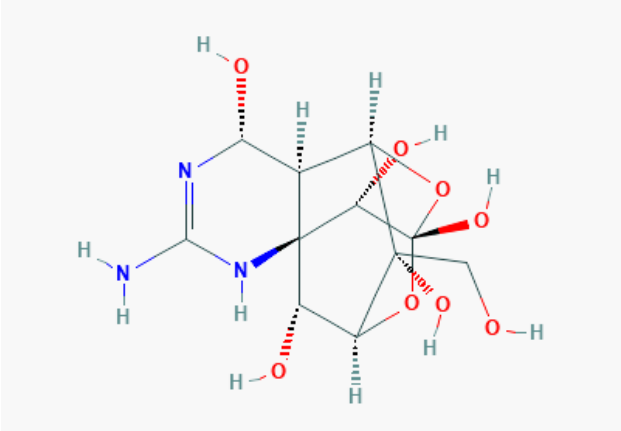

Figure 6.2 Tetrodotoxin chemical structure (from *https://pubchem.ncbi.nlm.nih.gov/*).

There is no known antidote for this toxin. Due to its paralysis effects, it could be used in medical fields as analgesic to treat cancer pains [128]. In my work, it was used to inhibit the action potential spikes in neurons.

6.1 Sample preparation

The sketch in figure 6.3 describes the procedure of sample preparation. For every cell culture coverslip, the short-term incubation with the NPs was limited to 5 min, depositing a drop of 300 µL of NPs dispersion in cell culture medium. In the case of measurements with TTX neurotoxin, TTX was diluted at a concentration of 1 µM in the culture medium. The

concentration of the NPs dispersion was different for every NP, but in most cases corresponded to the smallest amount needed to observe an interaction with the model membranes (Table 6.1).

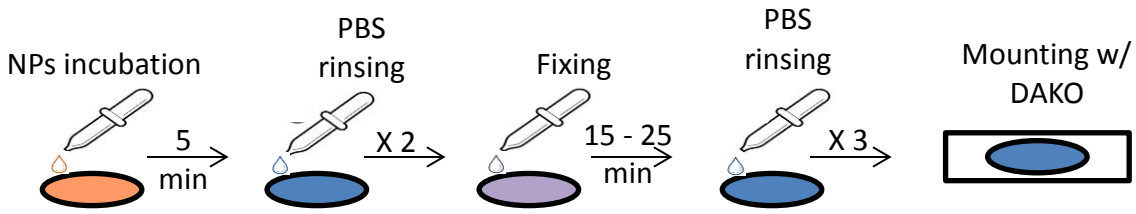

Figure 6.3 Sketch representing the procedure of incubation of NPs with cell lines and sample preparation for confocal microscopy investigation.

NP	concentration
NRs	5 nM
Micelles 60 nm	5 µM
Micelles 300 nm	25 µM

Table 6.1 Concentration for every NP employed in the study with cell lines. The concentration indicated for micelles refers to the total amount of polymer.

After the incubation, the coverslips were rinsed in PBS 1X two times to remove the excess of NPs and the cells were fixed using paraphormaldheyde (PFA) 4%, 25 min for neurons and 15 for the other cell lines.

PFA was then rinsed 3 times using PBS 1X and the coverslip was mounted using DAKO (Agilent, California) as a mounting medium. To avoid interference with the spontaneous NRs fluorescence in the 520-590 nm range, no nuclei marker, such as DAPI, was employed, since it emits in the same spectral range.

6.2 NPs interacting with cell lines: confocal microscopy investigation

Cells fixed after interaction with NPs were investigated by laser scanning confocal microscopy, using a Nikon A1 confocal microscope. Every image was captured using a 60X oil-immersion objective lens. Cell/NP interaction occurs if NPs could be find at the plasmatic membrane: no other marker was present in the sample, so cell membrane detection by laser scanning is possible only due to the presence of NPs. Due to their spectral emission properties (see Chapter 3) NRs were detected using 488 nm laser, whereas micelles using 560 nm laser. For every cell group coming from the same dissection/culture, a control sample was used to find the limit of laser power at which no auto-fluorescence was detected. Control images were captured with 488 nm laser in order to obtain the parameters for the NRs/cells samples investigation, 560 nm laser was used for the control images of micelles/cells samples. Negatively charged micelles, negative and positive NRs were tested with these cell lines; for neurons, a gradient of charged NRs varying from -50 to +20 mV was tested.

Figure 6.4 shows the results obtained using cell lines with negative NRs and 60 nm micelles. 60 and 300 nm micelles behaved in the same way (data not shown). As it is possible to see, negatively charged NRs (-50 mV) and micelles (-24 mV) interacted with neurons and differentiated N2a, whereas no interaction was detected for non-differentiated N2a and CHO cell lines. As stated in the chapter introduction, neurons and differentiated N2a are characterized by the presence of action potential spikes, during which the trans-membrane potential (difference in the distribution of charged ions between extra and intracellular environment) changes from resting negative values toward positive values (i.e. from -70 to +30 mV [126]); instead, non-differentiated N2a and CHO cell lines have a static negative trans-membrane potential (around -50 mV [129]). The dynamically driven trans-membrane potential of the first two groups of cells is the most relevant difference with the other two cell lines, and it seems to drive the interaction with the cellular membrane. Positively charged NRs (+20 mV) did not interact with any cell lines.

In agreement with the results obtained for model membranes described in chapter 5, also for cells in vitro, it is necessary to overcome an electrical threshold in order to observe an interaction between NP and the cell membrane. Neurons were tested with a gradient of charged NRs, i.e. -50, -18, -8, +8 and +20 mV, obtained changing the amount in EDC and DMEDA in the procedure of surface functionalization of NRs (see chapter 3, paragraph 3.3).

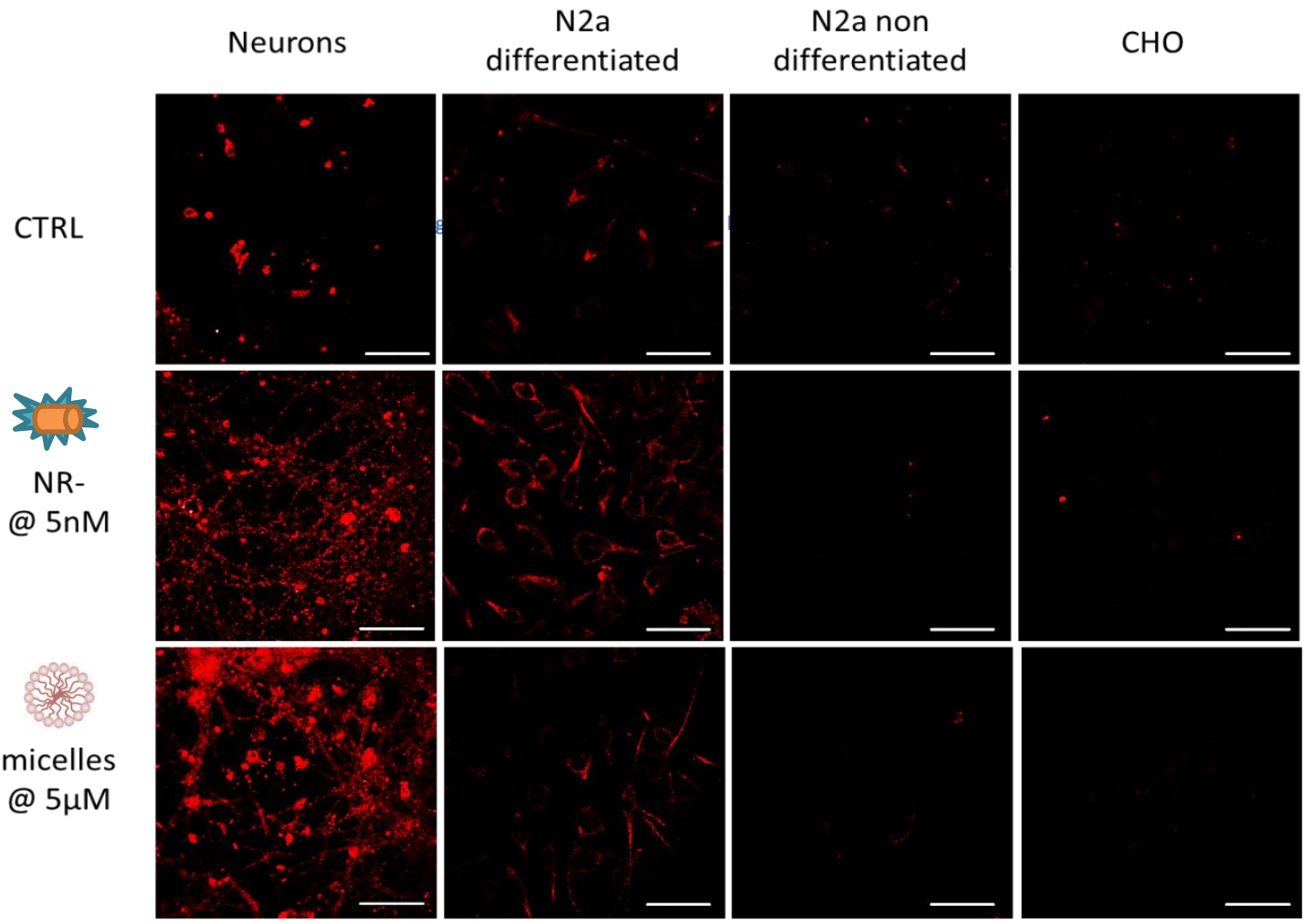

Figure 6.4 Confocal images of neurons, differentiated and non- differentiated N2a and CHO interacting with negatively charge NRs and polymeric micelles. Scalebar: 50µm.

The results are shown in figure 6.5: a strong interaction is registered with -50 mV NRs, a weaker one, but still appreciable with -18 mV and no interaction was observed in all other cases. We can state that also in this case there is a threshold, that, if calculated respect to the positive peak of the action potential spike (+ 30mV), is $\left|\Delta\zeta_{(\text{membrane-NR})}\right| \approx 48$ mV. The value is slightly lower than what was determined with model membranes; however, the zeta potential of the SLB was not measured, but only assumed to be the same of the vesicles before fusion on SiO_2. Positively charged NRs did not interact with any cell line.

The lipid model system with gel phase separated domains is a good model for the static trans-membrane potential cell lines, in which no interaction is registered due to the complexity of the membrane under study.

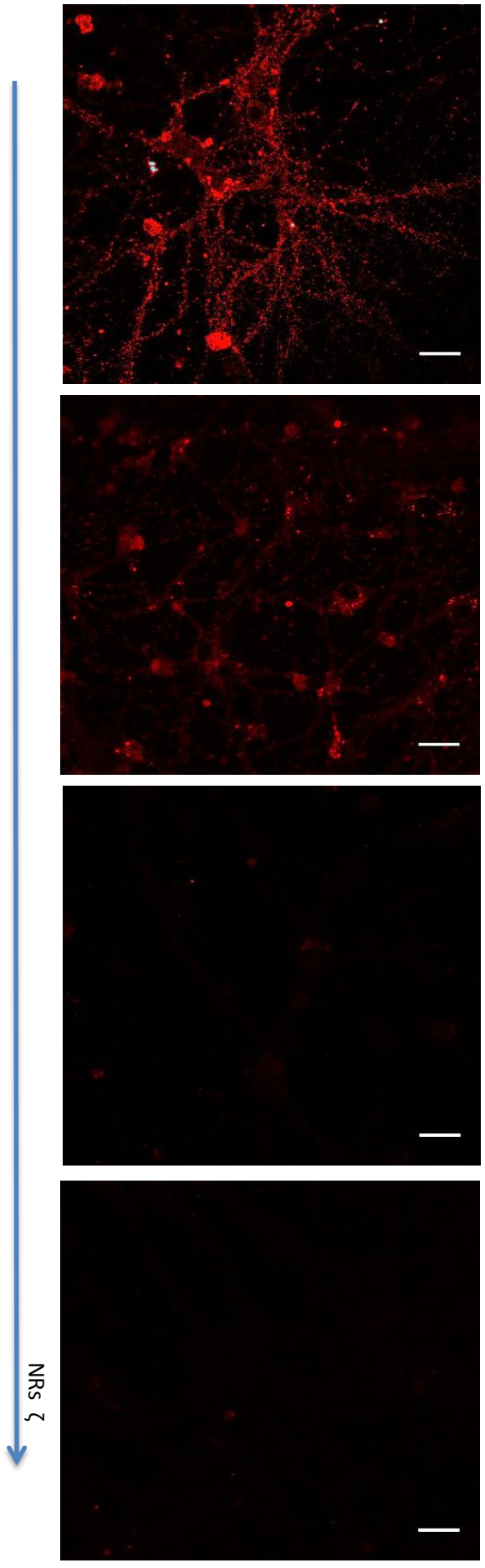

Figure 6.5 Confocal images of neurons interacting with a gradient of charged NRs. In order: -50, -18, -8, +20 mV. Scalebar: 50µm.

6.3 Real time incubation investigation

The same microscopy set up was used to perform real time imaging of NPs attachment of cellular membrane. The coverslip in which cells were seeded was mounted on an aluminum chamber specifically designed for visualization of samples in liquid environment. The chamber has an open top and allows the in situ deposition of the NPs dispersion. A transparent cell culture medium without phenol-red (Molecular Probes, Eugene, Oregon) was used for this purpose, in order to eliminate any other fluorescence source. NPs dispersions were prepared in the same medium, using lower concentrations: 1 nM for NRs, 0.7 µM for 300 nm micelles and 50 nM for 60 nm micelles. The concentration was optimized in order to reduce the background fluorescence and to allow the real-time monitoring of the attachment, otherwise too fast. A time lapse video was acquired (60X immersion objective lens, 2 frames per second for a total duration of 2 min).

Figure 6.6 shows some consequent frames of the 300 nm micelles attachment to the neuronal membrane, figure 6.7 the same experiment with -50 mV NRs: it is clear how the number of NPs attached is increasing with time (i.e. the fluorescence intensity is increasing). The total time of interaction to saturate the membrane with micelles was about 30 seconds, whereas for NRs the process was faster (less than 10 seconds).

Neurotoxin TTX was then introduced in the experiment to modify the action potential spikes of the cells. Cells were incubated for 5 minutes with TTX in transparent medium at 1 µM. NPs dispersed in the same solution were then deposited on the cell culture coverslip. As is possible to observe from figures 6.8 the presence of TTX in the medium caused a decrease in the fluorescence intensity, i.e. it decreased the amount of 300 nm micelles attaching to the neuronal membrane. The effect of the neurotoxin is evident in the first few seconds from the beginning of the experiment. The same experiments were repeated with 60 nm micelles, obtaining the same result (data not shown).

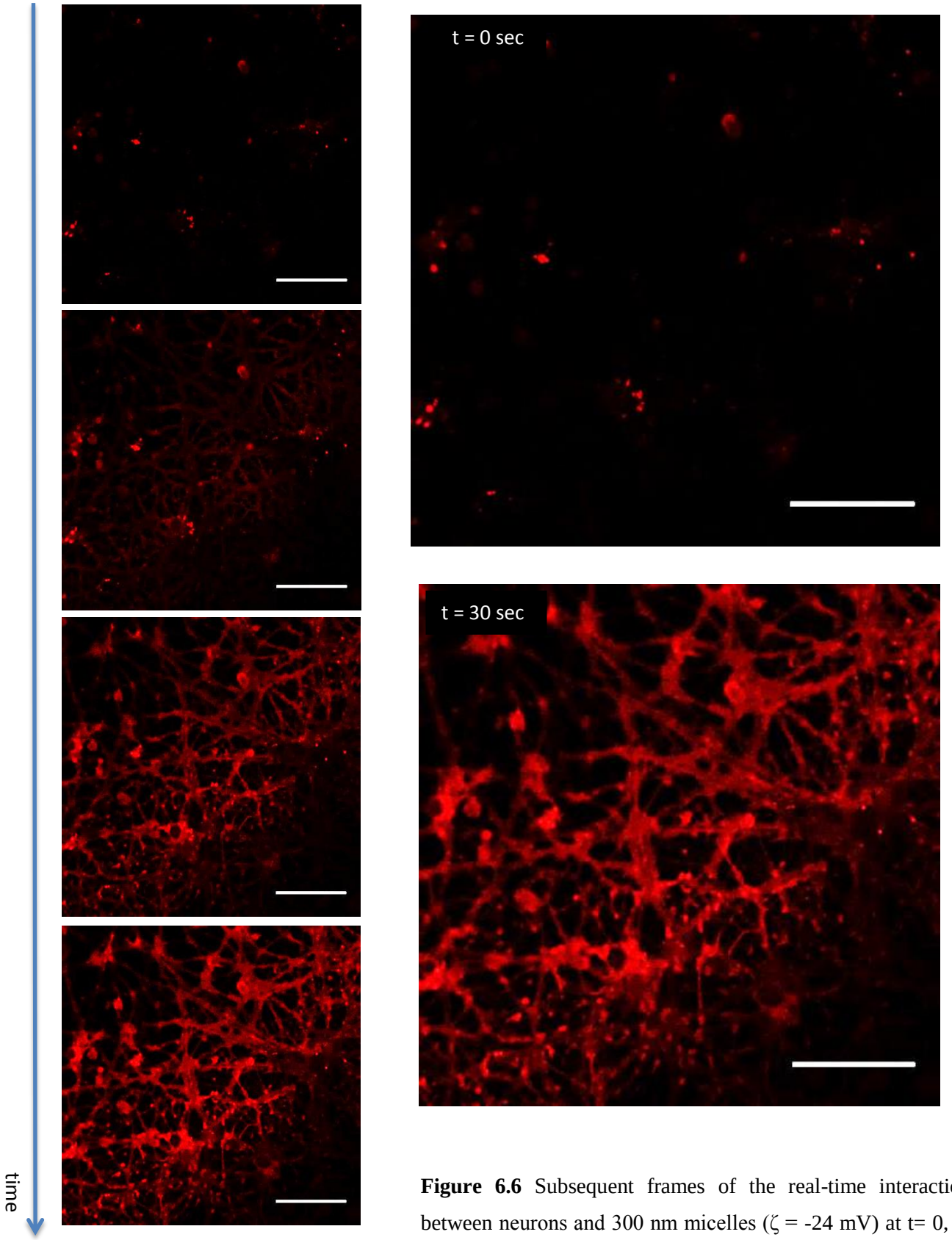

Figure 6.6 Subsequent frames of the real-time interaction between neurons and 300 nm micelles (ζ = -24 mV) at t= 0, 6, 15, 30 sec. Scale bar: 50 μm. The two magnifications show in details the initial and final images of the video.

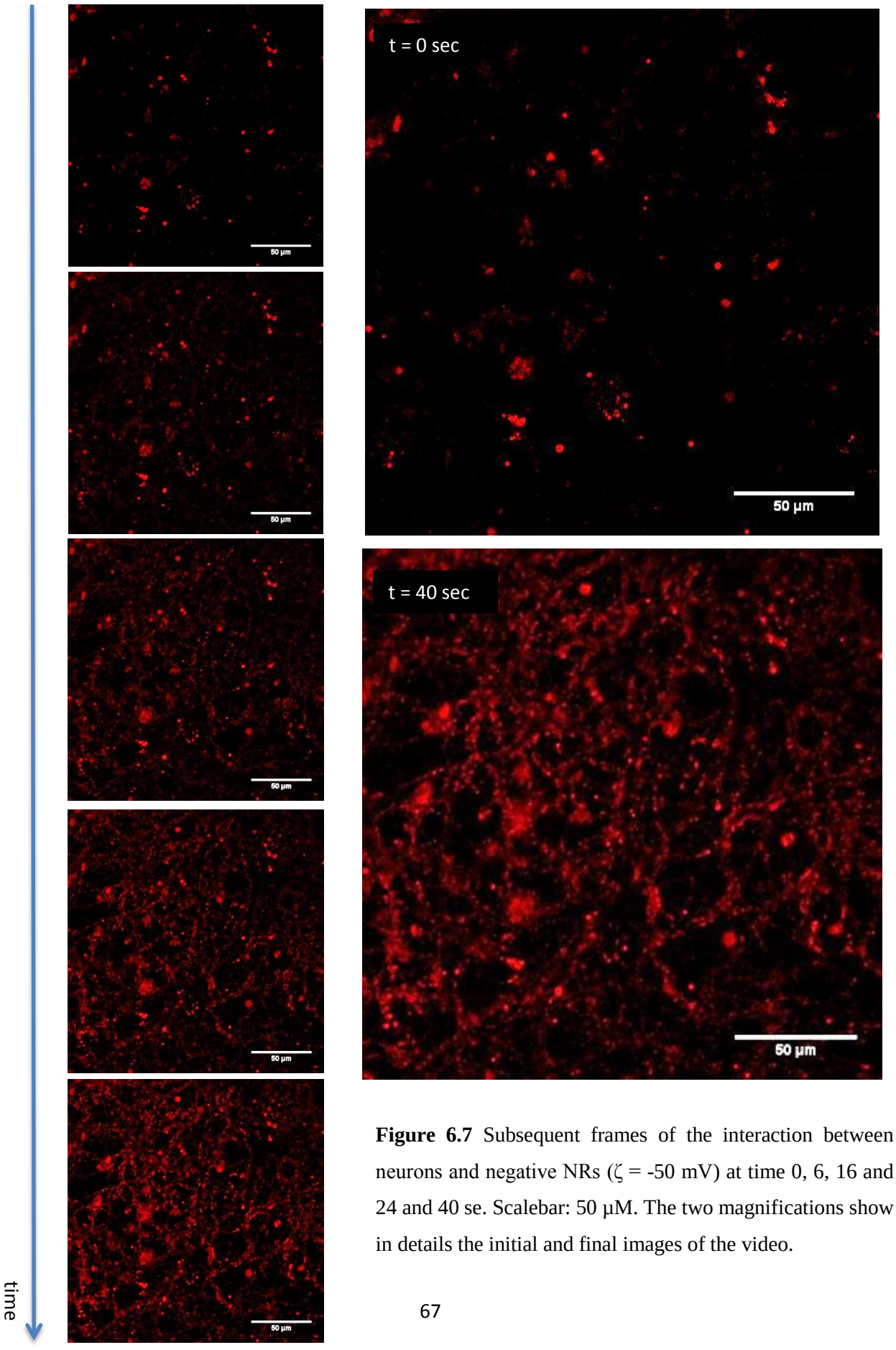

Figure 6.7 Subsequent frames of the interaction between neurons and negative NRs (ζ = -50 mV) at time 0, 6, 16 and 24 and 40 se. Scalebar: 50 µM. The two magnifications show in details the initial and final images of the video.

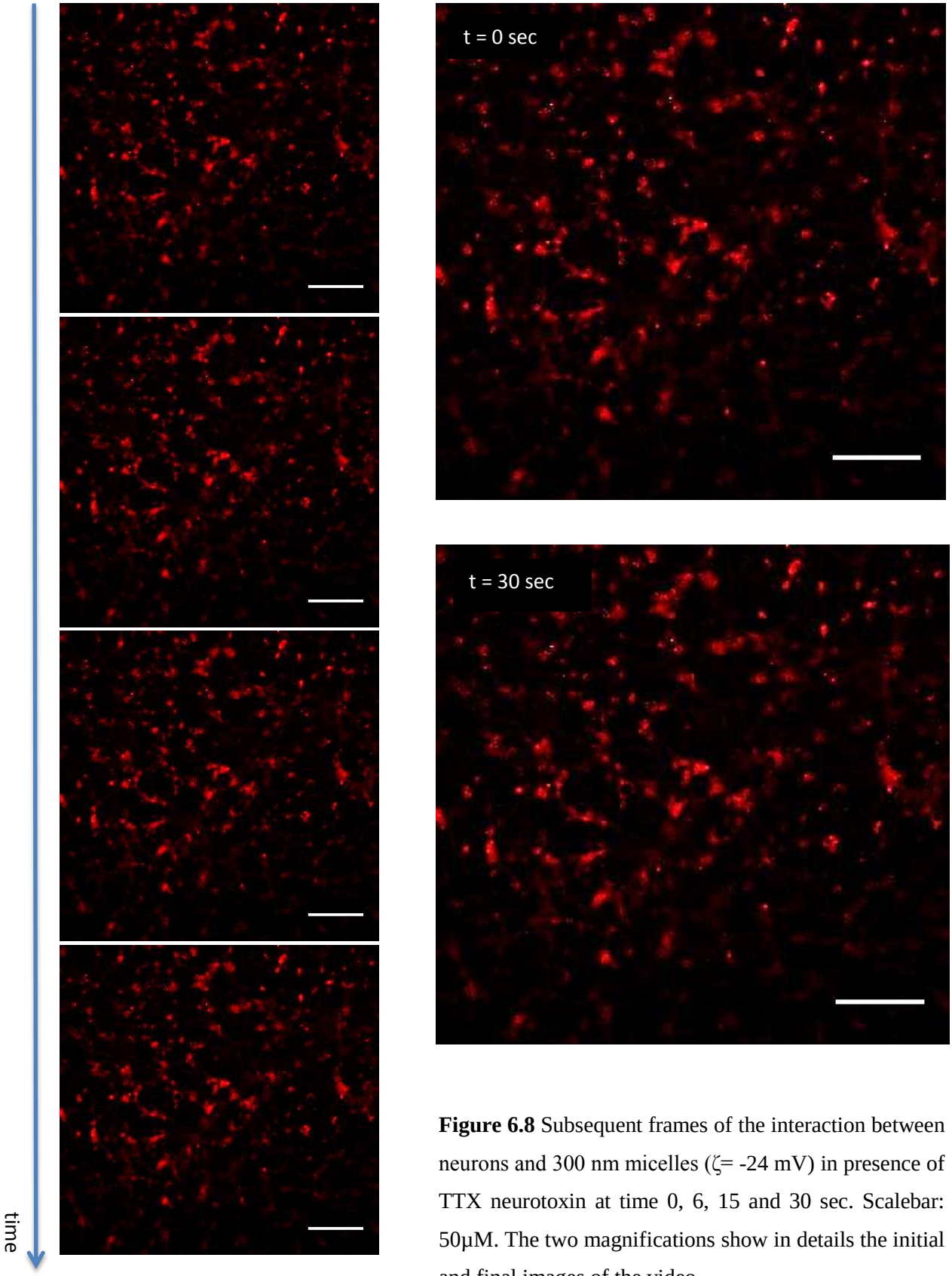

Figure 6.8 Subsequent frames of the interaction between neurons and 300 nm micelles (ζ= -24 mV) in presence of TTX neurotoxin at time 0, 6, 15 and 30 sec. Scalebar: 50μM. The two magnifications show in details the initial and final images of the video.

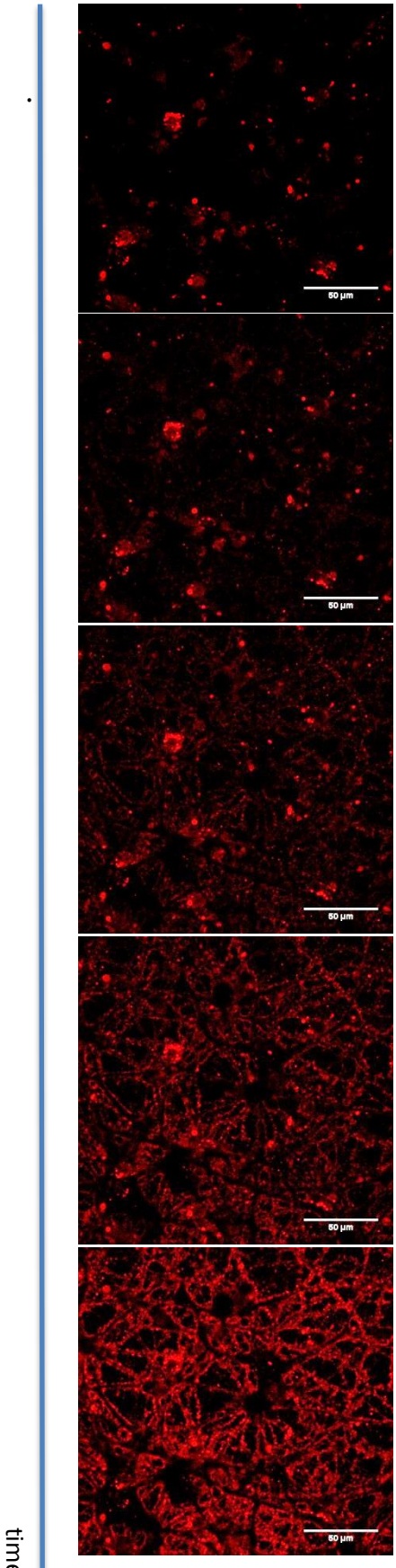

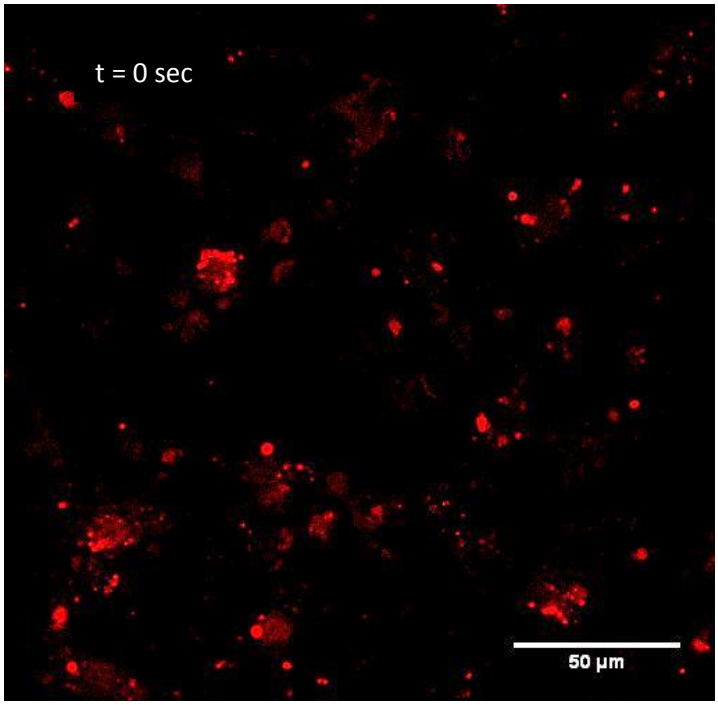

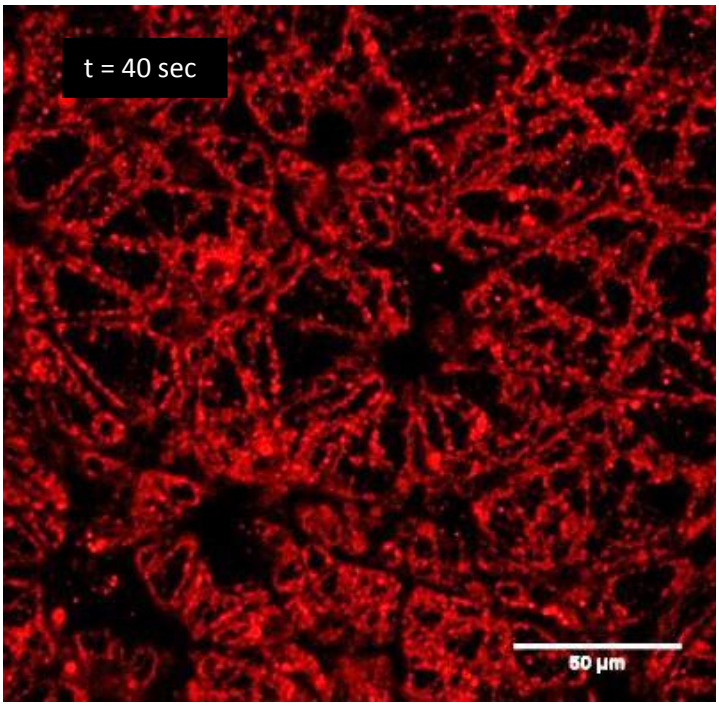

Figure 6.9 Subsequent frames of the interaction between neurons and -50 mV NRs in presence of TTX neurotoxin at t = 0, 6, 16, 24, 40 sec. Scalebar 50 µM. The two magnifications show in details the initial and final images of the video.

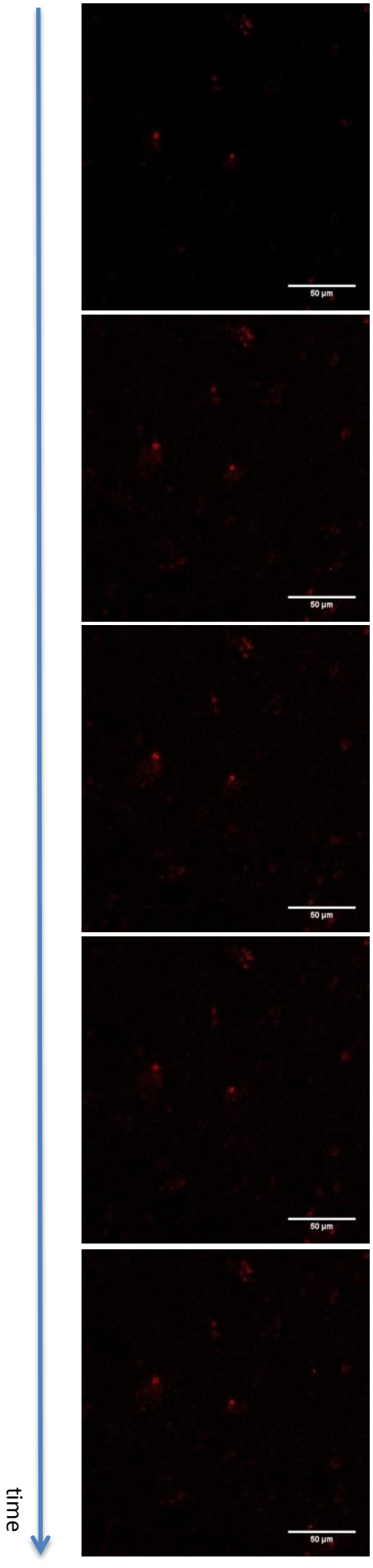

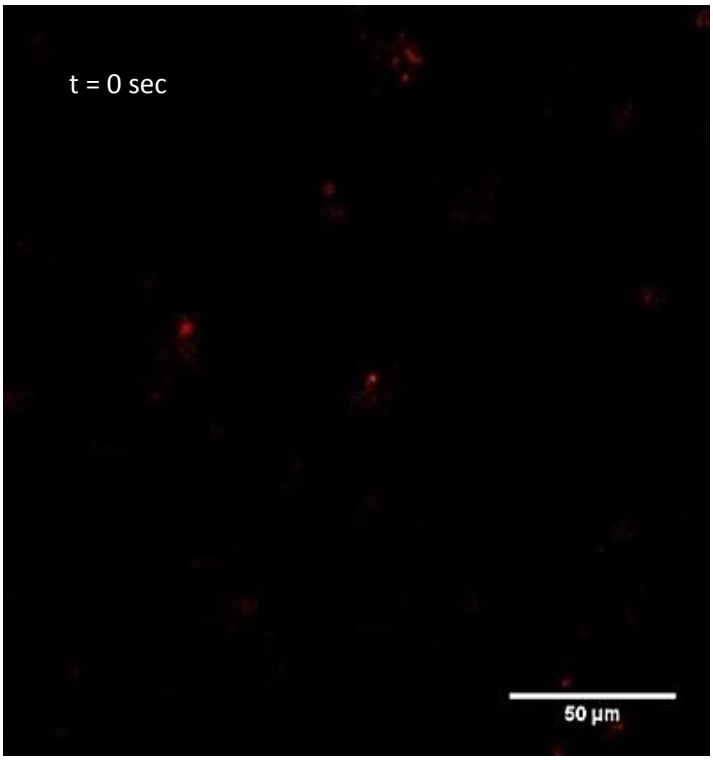

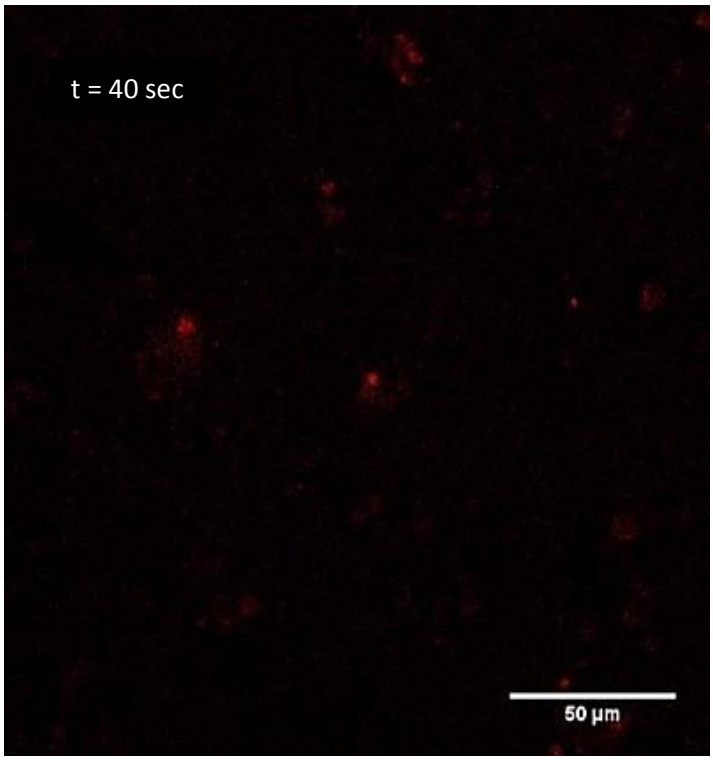

Figure 6.10 Subsequent frames of the interaction between neurons and -18 mV NRs in presence of TTX neurotoxin at t = 0, 6, 16, 24, 40 sec. Scalebar 50 µM. The two magnifications show in details the initial and final images of the video.

The effect of TTX in the interaction was tested also on NRs. Figure 6.9 and 6.10 show the results obtained with -50 and -18 NRs. Although the presence of the toxin, -50 mV NRs interacted with the membrane, whereas no interaction was registered using -18 mV NRs.

As I mentioned before, NRs interaction with the neuronal membrane was driven by the surface charge of the NRs, and a threshold value at -18 mV was found. At this surface potential value, the $\Delta\zeta$ is not sufficient to trigger an interaction.

6.4 Conclusions

I investigated the interaction between surface tuned NRs, tuned from negative to positive zeta potential values and negative polymeric micelles with 60 nm and 300 nm of diameter with in vitro cells. The interaction involves mostly the synaptic elongations, and NPs were employed with the aim to modulate the neuronal activity.

The difference in size did not affect the interaction. Cells investigated were: primary mouse neurons, mouse neuroblastoma differentiated and non-differentiated N2a and Chinese hamster ovary epithelial cells.

The first experiments were conducted incubating cells for 5 minutes with NPs, and then fixing them. From these experiments, it was evident that negatively charged NPs were interacting only with cell lines presenting variable membrane potential (such as neurons and differentiated N2a), whereas no interaction was occurring with static membrane potential cells. The static cell membranes can be resembled to the model membranes with gel phase domains, in which also if the charge requirements were satisfied (i.e. with positive NRs) no interaction was registered due to the steric hindrance created by the complex structure of the membrane. It was needed a dynamic membrane potential to induce the interaction, probably creating the appropriate conditions during the positive peak of the action potential process. The threshold value to observe the interaction is still present, as it is possible to understand by the experiment performed in neurons, in which NRs interacted with the cell membrane only if their potential was lower than -18 mV.

In the second part, time lapse videos captured in real time the process of interaction between NPs and cellular membrane. With these experiments, it was clear that the binding process is very fast (30 sec either for micelles and NRs), but the most relevant result was linked to the effects of TTX neurotoxin on neurons, that inhibiting the zeta potential spikes, blocked the interaction with NPs with a zeta potential not higher than -24 mV, falling back in the static cells case were no interaction was occurring. With -50 mV NRs, no differences were observed with and without the neurotoxin.

During my experiments with cell lines, NPs were diluted in transparent cell culture medium. As the results shown, the interaction between NPs and the cellular membrane occurs only for dynamically changing membrane potential cells (i.e. neurons and differentiated N2a), reinforcing the hypothesis that action potential was triggering the interaction. For the static membrane potential cells, we speculated that the situation is similar to the one observed with synthetic membrane: no interaction was registered with NRs dispersed in media different from water, due to the shield-effect on the charge caused by the ions in solution (see chapter 5).

Appendix A
Study on non-PEGylated NRs and model membranes

In this appendix, the results obtained using non-PEGylated NRs together with model membranes, will be shown. These NRs are the same crystals employed in the rest of my thesis but they underwent only the water solubilization process (see chapter 3, paragraph 3.3) and present a highly negative surface potential (ζ_{NR} = -50mV). In specific, lipid models such as fluid state SLBs, LMs and LMLs were investigated by QCM-D, π-A isotherms and x-rays diffraction (XRD), respectively. These experiments were performed to reinforce the hypothesis of the great importance attributed to the PEG-layer covering the rods in the interaction with membranes. Before showing the results, the XRD technique will be briefly explained.

I. Methods

I.a X-Ray Diffraction

X-ray diffraction (XRD) is an analytical technique primarily used for phase identification of a crystalline material and that can provide information on unit cell dimensions of periodic lattices. XRD is based on constructive interference of monochromatic X-rays on a crystalline sample. X-rays are generated by a cathode ray tube, filtered to produce monochromatic radiation, collimated to concentrate and directed toward the sample. The interaction of the incident rays with the sample produces constructive interference (and a diffracted ray) when conditions satisfy Bragg's Law:

$$n\lambda = 2d \sin \theta$$

This law relates the wavelength of electromagnetic radiation λ to the diffraction angle θ and the lattice spacing d in a crystalline sample. Diffracted X-rays are then detected, processed and counted. By scanning the sample through a range of 2θ angles, all possible diffraction directions of the lattice should be attained. Conversion of the diffraction peaks (see table I in

paragraph II.c as an example) to *d*-spacings allows identification of the mineral because each mineral has a set of unique *d*-spacings.

XRD has been applied in this thesis to investigate the structure of lipid multilayers interacting with NPs, measuring the difference in the sample diffraction peaks with and without the presence of nanoparticles. LMLs (i.e. hydrated lipids deposited on the substrate) present a 1D crystalline structure in the *z* direction, perpendicular to the substrate. The elementary cell of this structure is represented by the hydrated bilayer, i.e., the lipid bilayer including the water molecules of the hydration layer. The Bragg's law can be used to obtain the *d*-spacing of every lamellar cell, i.e. the distance between the two external polar-heads, including the hydration water layer.

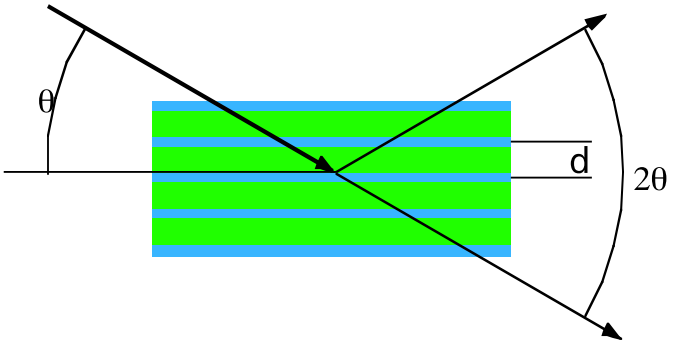

Figure I. Sketch representing Bragg's diffraction in a multilayered structure. See figure 1.8 for the LML structure.

The second information in a diffraction pattern is given by the measured intensities I_l of the Bragg peaks, which allow the determination of the electrons distribution in the crystal lattice (i.e. the electron density of the unit cell). The intensities are related to the amplitude of the structure factors F_l, which are linked to the electron density by a Fourier transform operation. F_l are complex number but, in a centrosymmetric crystal (such as the 1D lipid multilayers) their phase can only assume a value of -1 or 1. In this case, it holds that:

$$\Delta\rho = \sum_{l=1}^{N} F_l \cos\left(2\pi l \frac{z}{d}\right)$$

where ρ is the electron density, N is the number of observed Bragg peaks, F is the structure factor, z is the position in the cell measured in nm and d is the cell dimension in nm, calculated using the Bragg's law.

I used this technique to investigate the behavior of non-PEGylated NRs with positively charged lipid multilayers.

I.b XRD sample preparation and measurements

N-doped SiO_2 wafers 2x1 cm^2 were cut with the help of a diamond blade as substrates for XRD measurements. Wafers were cleaned by sonication in a 2% SDS solution for 20 min at a temperature of 60 °C, then rinsed three times with ultrapure water and dried under N_2 flow. To remove any organic contaminants from the surface, the sensors were placed in ozone cleaner for 10 min before use. 200 µL of vesicles dispersion at a concentration of 0.5 g/L (with and without NRs) were deposited on the wafers and dried under vacuum conditions overnight in order to obtain a lipid multilayer (LML). LUVs dispersion were let to interact with NRs (NRs : lipids ratio 1:1000) for a total of 2 h before being deposited onto the silicon wafers. Samples were annealed in an oven at 60 °C for 30 min, left at room temperature for other 30 min and then the procedure was repeated 5 times in order to make the samples homogeneous. XRD measurements were performed with a rotating anode Rigaku SmartLab diffractometer operating in the reflection mode in θ-2θ geometry with Cu-Kα radiation (35 kV, 30 mA, λ = 1.54 nm) and diffracted beam monochromator, using a step scan mode with the step of 0.075° (2θ) and 4 s per step in dry and wet conditions under a doom. For the wet conditions, 150 µL of ultrapure water were deposited in the well of the XRD sample holder. To keep the humidity at

90% and prevent the formation of water condense on the top of the doom potassium sulfate was deposited into the well.

II. Results

II.a Non-PEGylated NRs with fluid state bilayers

Non-PEGylated NRs were tested with positively charged POPC/DOTAP 50:50 and 75:25 mol:mol SLB. Although the difference in ζ between SLB and NRs was overcoming the threshold we observed with tuned NRs, in this case no adsorption of NRs occurred, reasonably due to the absence of the functionalization agents.

II.b Non-PEGylated NRs and fluid state monolayers

Non-PEGylated NRs were tested with positively charged fluid state LMs, specifically POPC/DOTAP 50:50 and 75:25 molar ratios. Figure II shows the results obtained. Although no interaction was registered using this NRs on SLBs (see paragraph 5.1.2), the figures show a strong interaction between lipids and NRs, similar for both compositions: the lift-off area of the LM increases going from 110 to 144 $Å^2$/molecule in presence of NRs in the subphase; the slope of the isotherm decreases drastically until a sort of second lift-off appears at 60 $Å^2$/molecule. This can be interpreted as a big amount of NRs was attracted towards the surface by the high difference in charge they have with the lipids; this interaction was so strong that lipids were removed from the surface until a saturation is reached (second lift-off area) and a LM with a considerably smaller number of lipids re- arranged with the lipids remaining at the interface. Non-PEGylated NRs did not interact with SLB, and this can be reconducted to the fact that SLBs are in a highly packed situation when the NRs are injected in the measurement chamber, whereas, for LMs, the measurements start from a $\pi \approx 0$ mN/m, i.e. the starting point is in a disordered configuration of the lipids at the interface. Starting from higher values was not possible with our setup: NRs were injected into the subphase when lipids were already in a compressed configuration and they were not dispersing in the water subphase but tent to remain clustered in an isolated drop.

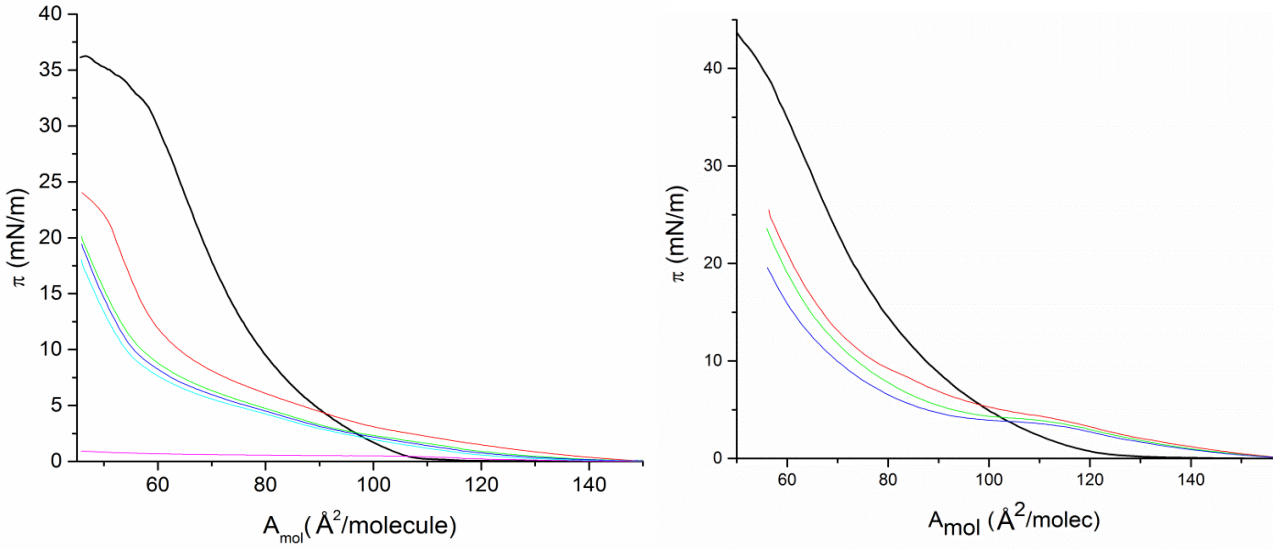

Figure II π –A isotherms of POPC/DOTAP 50:50 (left) and 75:25 (right) mol:mol monolayers interacting with non-PEGylated NRs. Black: lipid mixtures in an ultrapure water subphase. Red, green, blue, cyan represent the first, second, third and fourth compressions, respectively, in the NR dispersion subphase. Magenta isotherm relates to the behavior of NRs in water: they are not going toward the surface in absence of lipids at the interface.

II.c LMLs and NRs

I have tried to get further insight on the NR/membrane interaction by using XRD. This part of the investigation is not fully accomplished yet. I have started my investigation from the simplest NRs in term of structure, i.e. the non-PEGylated ones. Experiments with PEGylated NRs are still ongoing. In order to obtain a structure suitable for this technique, I produced fluid state positive lipid multilayers. The lipid mixture chosen are those already tested in the SLB and LM studies for the same particles. POPC, DOTAP and POPC/DOTAP 50:50 and 75:25 mol:mol mixtures were investigated by XRD both in dry and in wet conditions. Every wet sample was let to stabilize for at least 7 h, in some cases overnight to see no variations in the peaks position due to the continue adsorption of water molecules in the LML. Binary mixtures were then investigated in presence of NRs and compared to see any structural difference. As an example, the pattern of the diffraction peaks for hydrated POPC, DOTAP and POPC/DOTAP

50:50 mol:mol mixture with and without NRs is shown in figure II, Every sample presented till the 5th (6th for pure DOTAP) order of evenly spaced diffraction peaks, indicating the presence of an ordered lamellar structure. From the angular position of every peak, the *d*-spacings of the samples were calculated using the Bragg's law and performing a linear regression on the results obtained for every peak's order. Table I summarize the value for every sample. Then, the relative electron density ρ was calculated. The electron density presents a mirrored graph with information about the position of the elements of the cells constituting the crystalline structure in which there is a high density of electrons. The maximum in the curve represents the water of the hydration layer, followed by the polar head, the unsaturations (i.e. the double C-C bonds in the unsaturated chains lipids) and the zero point represents the hydrophobic center of the bilayer (see figure III). In the case of POPC/DOTAP 50:50 LML the interaction is registered in correspondence of the hydration layer and the polar headgroups (|z| = 2.81 and 2 nm, respectively) indicating an interaction in correspondence of the hydrophilic elements of the LML cell.

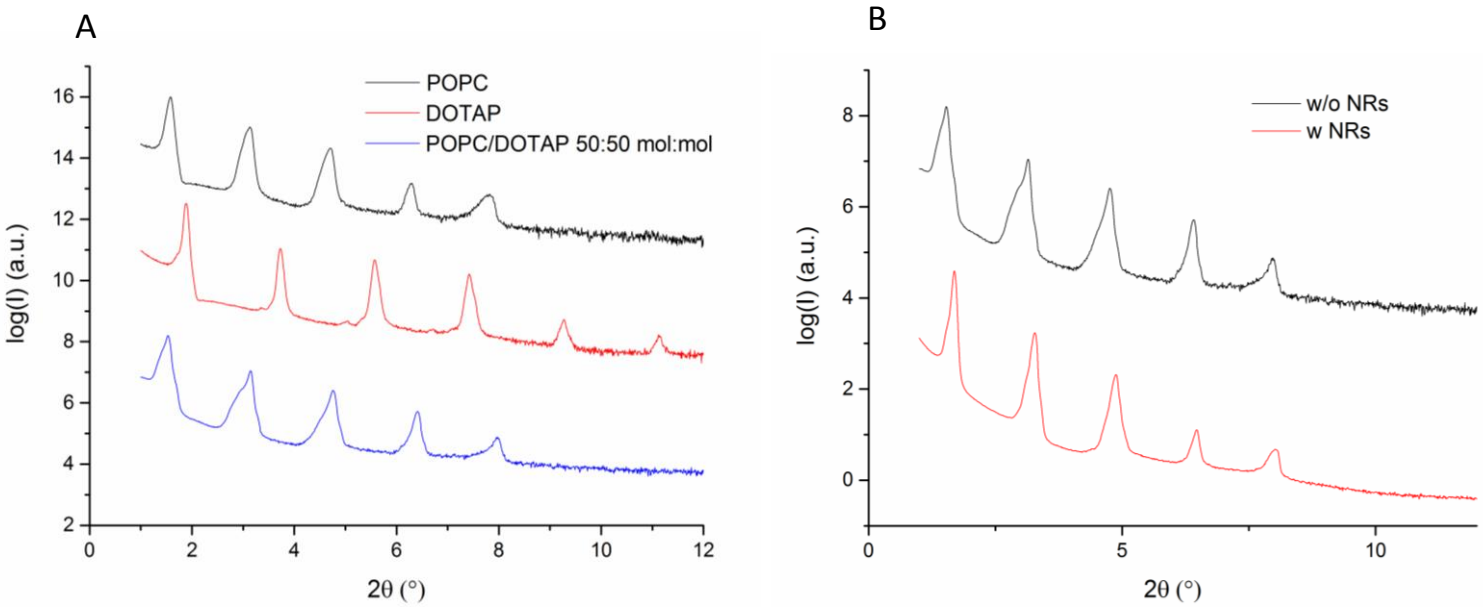

Figure II. Patterns of single POPC, DOTAP and mixtures POPC/DOTAP 50:50 mol:mol (A) and POPC/DOTAP 50:50 mol:mol with and without non-PEGylated NRs (B).

Also, a modification in correspondence of the unsaturated bond (|z| = 0.6 nm) was observed. The resolution of this part of the cell is lost in a lateral enlargement of the curve in presence of NRs. For POPC/DOTAP 75:25 LML the situation is similar, but the biggest modification in the Δρ is in correspondence of the hydration layer in this case, indicating that the NRs have a weaker interaction with this mixture.

Lipid mixture	d-spacing (nm)	Lipid mixture	d-spacing (nm)
POPC	5.7 ± 0.2	**DOTAP**	4.8 ± 0.2
POPC/DOTAP 50:50	5.5 ± 0.2	**POPC/DOTAP 75:25**	5.5 ± 0.2
POPC/DOTAP 50:50 + NRs	5.6 ± 0.2	**POPC/DOTAP 75:25 + NRs**	5.9 ± 0.2

Table I. *d*-spacing of every sample calculated by linear regression from the Bragg's law results of every peak order.

In particular, the position of the highest peak is shifted towards higher z values, resulting in a total increase of the dimension of the cell in presence of NRs. Also in this mixture, a modification in correspondence of the unsaturated bond (|z| = 0.6 nm) was showed but opposite respect to the previous one, being that the curve becomes narrower in presence of NRs.

III. Conclusions

The first interesting observation on the study of non-PEGylated NRs with model membranes is their non-interaction with fluid state bilayers, although the difference in zeta potential highly overcomes the above mentioned threshold. This indicates that the interaction is not exclusively regulated by lipid head-group charges, but also other properties such as the mechanical behavior of the membrane, or the presence of the outer polymeric layer of functionalization plays important roles.

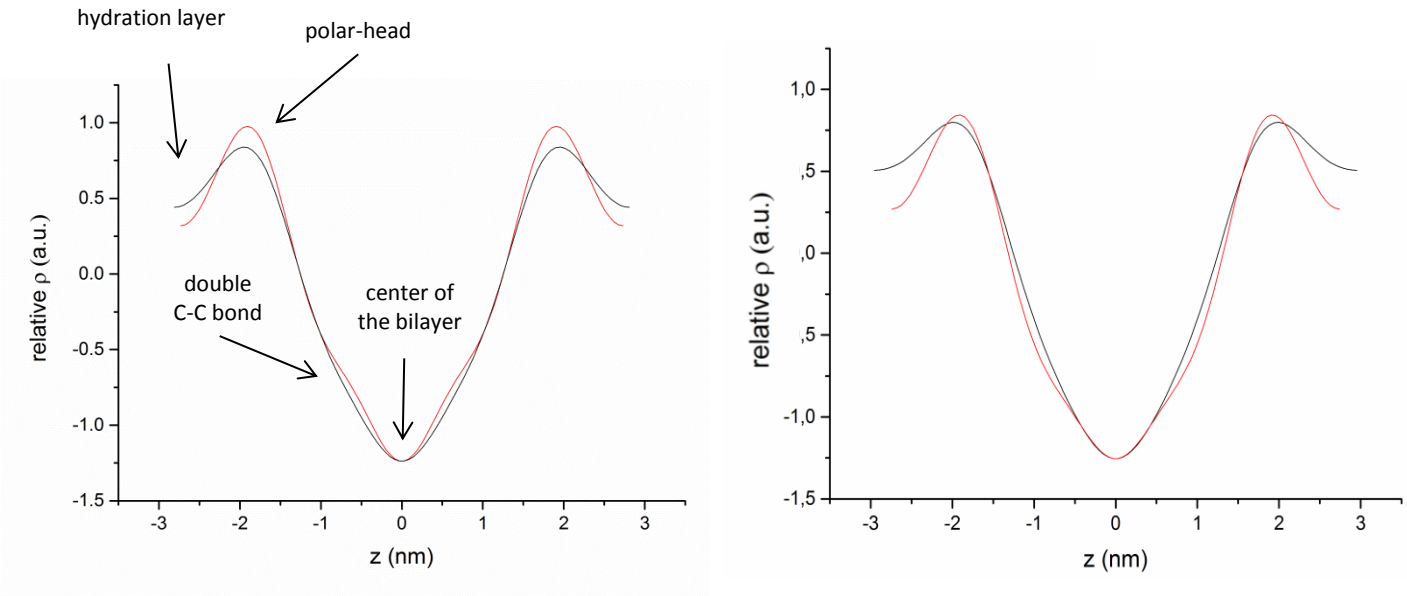

Figure III. Relative electron density profile (Δρ) plotted versus the position in the bilayer respect the central position (z=0 nm). Red curve represents pure lipids, , black curve lipids + NRs. Left: POPC/DOTAP 50:50, right: POPC/DOTAP 75:25.

The importance of the PEG-amine/lipid group interaction is confirmed by the experiments that involve the non-PEGylated NRs: in this case, interaction is highly disturbed respect to the surface charge tuned NRs investigation, leading to a big removal of lipids from the surface after the initial insertion between the polar-heads.

I carried out also an investigation of lipid multilayers with non-PEGylated NRs. I used only fluid state lipids with a positive total charge, and I used the same two compositions, used with LMs, POPC/DOTAP 50:50 and 75:25 molar ratios. From the electron density profiles is possible to see that the dimension of the elementary cell increased in presence of NRs, indicating that an interaction occurred, and that this interaction came in correspondence of the hydrophilic part of the cell: in the case of the 50:50 mol:mol composition, the modification is equally distributed between the polar head and the hydration layer positions ($|z|$ = 1.9 and 2.8 nm respectively), whereas the modification for the less charged mixture 75:25 mol:mol was all

in correspondence of the hydration layer. Here, it is confirmed that hydrophilic NRs interact with lipids following the overall charge of the system inserting between polar head and hydration layer in the case of POPC/DOTAP 50:50, and when the conditions are not respected (as in the case of POPC/DOTAP 75:25) they deposit in the water layer between the single lamellar planes.

References

1. Davson, H. and J.F. Danielli, *The Permeability of Natural Membranes*. 1970: Hafner.
2. O'Brien, J.S., *Cell membranes—Composition: Structure: Function.* Journal of Theoretical Biology, 1967. **15**(3): p. 307-324.
3. Singer, S.J. and G.L. Nicolson, *The Fluid Mosaic Model of the Structure of Cell Membranes.* Science, 1972. **175**(4023): p. 720.
4. van Meer, G., D.R. Voelker, and G.W. Feigenson, *Membrane lipids: where they are and how they behave.* Nature Reviews Molecular Cell Biology, 2008. **9**: p. 112.
5. M. Ashrafuzzaman, J.T., *Membrane Biophysics*. 2012.
6. Sonnino, S. and A. Prinetti, *Lipids and Membrane Lateral Organization.* Frontiers in Physiology, 2010. **1**: p. 153.
7. Bagatolli, L.A., *To see or not to see: Lateral organization of biological membranes and fluorescence microscopy.* Biochimica et Biophysica Acta (BBA) - Biomembranes, 2006. **1758**(10): p. 1541-1556.
8. Simons, K. and E. Ikonen, *Functional rafts in cell membranes.* Nature, 1997. **387**: p. 569.
9. Deborah A. Brown, E.L., *Structure and Function of Sphingolipid- and Cholesterol-rich Membrane Rafts.* The Journal of Biological Chemistry, 2000. **275**(23): p. 17221–17224.
10. Lingwood, D. and K. Simons, *Lipid Rafts As a Membrane-Organizing Principle.* Science, 2010. **327**(5961): p. 46.
11. van Meer, G., D.R. Voelker, and G.W. Feigenson, *Membrane lipids: where they are and how they behave.* Nature reviews. Molecular cell biology, 2008. **9**(2): p. 112-124.
12. Cevc, G., *How membrane chain-melting phase-transition temperature is affected by the lipid chain asymmetry and degree of unsaturation: an effective chain-length model.* Biochemistry, 1991. **30**(29): p. 7186-7193.
13. Berde, C.B., H.C. Andersen, and B.S. Hudson, *A theory of the effects of head-group structure and chain unsaturation on the chain melting transition of phospholipid dispersions.* Biochemistry, 1980. **19**(18): p. 4279-4293.
14. Vaz, W.L.C., F. Goodsaid-Zalduondo, and K. Jacobson, *Lateral diffusion of lipids and proteins in bilayer membranes.* FEBS Letters, 1984. **174**(2): p. 199-207.
15. Lee, A.G., N.J.M. Birdsall, and J.C. Metcalfe, *Measurement of fast lateral diffusion of lipids in vesicles and in biological membranes by proton nuclear magnetic resonance.* Biochemistry, 1973. **12**(8): p. 1650-1659.
16. Steim, J.M., et al., *Calorimetric Evidence For The Liquid-Crystalline State Of Lipids In A Biomembrane.* Proceedings of the National Academy of Sciences, 1969. **63**(1): p. 104.
17. Cullis, P.R. and B. De Kruijff, *The polymorphic phase behaviour of phosphatidylethanolamines of natural and synthetic origin. A 31P NMR study.* Biochimica et Biophysica Acta (BBA) - Biomembranes, 1978. **513**(1): p. 31-42.
18. Boggs, J.M., et al., *Influence of ether linkage on the lamellar to hexagonal phase transition of ethanolamine phospholipids.* Biochemistry, 1981. **20**(20): p. 5728-5735.
19. Helm, C.A., et al., *Phases of phosphatidyl ethanolamine monolayers studied by synchrotron x-ray scattering.* Biophysical Journal, 1991. **60**(6): p. 1457-1476.
20. Yeagle, P.L., *Cholesterol and the cell membrane.* Biochimica et Biophysica Acta (BBA) - Reviews on Biomembranes, 1985. **822**(3): p. 267-287.
21. Ohvo-Rekilä, H., et al., *Cholesterol interactions with phospholipids in membranes.* Progress in Lipid Research, 2002. **41**(1): p. 66-97.

22. Phillips, M.C., *The Physical State of Phospholipids and Cholesterol in Monolayers, Bilayers, and Membranes*, in *Progress in Surface and Membrane Science*, J.F. Danielli, M.D. Rosenberg, and D.A. Cadenhead, Editors. 1972, Elsevier. p. 139-221.
23. Veatch, S.L. and S.L. Keller, *Organization in Lipid Membranes Containing Cholesterol.* Physical Review Letters, 2002. **89**(26): p. 268101.
24. Op den Kamp, J.A.F., *Lipid Asymmetry in Membranes.* Annual Review of Biochemistry, 1979. **48**(1): p. 47-71.
25. Hovius, R., et al., *Improved methods to isolate and subfractionate rat liver mitochondria. Lipid composition of the inner and outer membrane.* Biochimica et Biophysica Acta (BBA) - Biomembranes, 1990. **1021**(2): p. 217-226.
26. Verkleij, A.J., et al., *The asymmetric distribution of phospholipids in the human red cell membrane. A combined study using phospholipases and freeze-etch electron microscopy.* Biochimica et Biophysica Acta (BBA) - Biomembranes, 1973. **323**(2): p. 178-193.
27. Zachowski, A., *Phospholipids in animal eukaryotic membranes: transverse asymmetry and movement.* Biochemical Journal, 1993. **294**(Pt 1): p. 1-14.
28. G.M., C., *The Cell: A Molecular Approach. Structure of the Plasma Membrane*. 2nd edition ed. 2000.
29. Hjort Ipsen, J., et al., *Phase equilibria in the phosphatidylcholine-cholesterol system.* Biochimica et Biophysica Acta (BBA) - Biomembranes, 1987. **905**(1): p. 162-172.
30. Jouhet, J., *Importance of the hexagonal lipid phase in biological membrane organization.* Frontiers in Plant Science, 2013. **4**: p. 494.
31. Mouritsen, O.G. and K. Jørgensen, *Dynamical order and disorder in lipid bilayers.* Chemistry and Physics of Lipids, 1994. **73**(1): p. 3-25.
32. Brezesinski, G. and H. Möhwald, *Langmuir monolayers to study interactions at model membrane surfaces.* Advances in Colloid and Interface Science, 2003. **100-102**: p. 563-584.
33. Chan, Y.-H.M. and S.G. Boxer, *Model Membrane Systems and Their Applications.* Curr. Opin. Chem. Biol., 2007. **11**(6): p. 581-587.
34. Czogalla, A., et al., *Validity and applicability of membrane model systems for studying interactions of peripheral membrane proteins with lipids.* Biochim. Biophys. Acta, Mol. Cell Biol. Lipids, 2014. **1841**(8): p. 1049-1059.
35. Mouritsen, O.G., *Model Answers to Lipid Membrane Questions.* Cold Spring Harbor Perspectives in Biology, 2011. **3**(9): p. a004622.
36. Peetla, C., A. Stine, and V. Labhasetwar, *Biophysical interactions with model lipid membranes: applications in drug discovery and drug delivery.* Molecular pharmaceutics, 2009. **6**(5): p. 1264-1276.
37. Simons, K. and W.L.C. Vaz, *Model Systems, Lipid Rafts, and Cell Membranes.* Annu. Rev. Biophys. Biomol. Struct., 2004. **33**(1): p. 269-295.
38. Maget-Dana, R., *The monolayer technique: a potent tool for studying the interfacial properties of antimicrobial and membrane-lytic peptides and their interactions with lipid membranes.* Biochimica et Biophysica Acta (BBA) - Biomembranes, 1999. **1462**(1): p. 109-140.
39. Sarmento, M.J., M. Prieto, and F. Fernandes, *Reorganization of lipid domain distribution in giant unilamellar vesicles upon immobilization with different membrane tethers.* Biochimica et Biophysica Acta (BBA) - Biomembranes, 2012. **1818**(11): p. 2605-2615.
40. Menon, A.K., *Small oligomers of immunoglobulin E (IgE) cause large-scale clustering of IgE receptors on the surface of rat basophilic leukemia cells.* The Journal of Cell Biology, 1984. **98**(2): p. 577-583.
41. Schönherr, H., et al., *Vesicle Adsorption and Lipid Bilayer Formation on Glass Studied by Atomic Force Microscopy.* Langmuir, 2004. **20**(26): p. 11600-11606.

42. L. Wagner, M. and L. K. Tamm, *Tethered Polymer-Supported Planar Lipid Bilayers for Reconstitution of Integral Membrane Proteins: Silane-Polyethyleneglycol-Lipid as a Cushion and Covalent Linker*. Vol. 79. 2000. 1400-14.
43. Heikkilä, E., et al., *Cationic Au Nanoparticle Binding with Plasma Membrane-like Lipid Bilayers: Potential Mechanism for Spontaneous Permeation to Cells Revealed by Atomistic Simulations.* The Journal of Physical Chemistry C, 2014. **118**(20): p. 11131-11141.
44. Dietrich, C., et al., *Lipid Rafts Reconstituted in Model Membranes.* Biophys. J., 2001. **80**(3): p. 1417-1428.
45. Richter, R.P. and A.R. Brisson, *Following the Formation of Supported Lipid Bilayers on Mica: A Study Combining AFM, QCM-D, and Ellipsometry.* Biophys. J., 2005. **88**(5): p. 3422-3433.
46. Enders, O., et al., *Structural Calorimetry of Main Transition of Supported DMPC Bilayers by Temperature-Controlled AFM.* Biophys. J., 2004. **87**(4): p. 2522-2531.
47. Richter, R., A. Mukhopadhyay, and A. Brisson, *Pathways of Lipid Vesicle Deposition on Solid Surfaces: A Combined QCM-D and AFM Study.* Biophys. J., 2003. **85**(5): p. 3035-3047.
48. Giess, F., et al., *The Protein-Tethered Lipid Bilayer: A Novel Mimic of the Biological Membrane.* Biophysical Journal, 2004. **87**(5): p. 3213-3220.
49. Köper, I., *Insulating tethered bilayer lipid membranes to study membrane proteins.* Molecular BioSystems, 2007. **3**(10): p. 651-657.
50. Vockenroth, I.K., et al., *Stable insulating tethered bilayer lipid membranes.* Biointerphases, 2008. **3**(2): p. FA68-FA73.
51. Dante, S., et al., *Nanoscale structural and mechanical effects of beta-amyloid (1–42) on polymer cushioned membranes: A combined study by neutron reflectometry and AFM Force Spectroscopy.* Biochimica et Biophysica Acta (BBA) - Biomembranes, 2011. **1808**(11): p. 2646-2655.
52. Sterling, S.M., et al., *Phospholipid Diffusion Coefficients of Cushioned Model Membranes Determined via Z-Scan Fluorescence Correlation Spectroscopy.* Langmuir, 2013. **29**(25): p. 7966-7974.
53. Poursoroush, A., M.M. Sperotto, and M. Laradji, *Phase behavior of supported lipid bilayers: A systematic study by coarse-grained molecular dynamics simulations.* The Journal of Chemical Physics, 2017. **146**(15): p. 154902.
54. Bennett, W.F.D. and D.P. Tieleman, *Computer simulations of lipid membrane domains.* Biochimica et Biophysica Acta (BBA) - Biomembranes, 2013. **1828**(8): p. 1765-1776.
55. Rossi, G. and L. Monticelli, *Gold nanoparticles in model biological membranes: A computational perspective.* Biochim. Biophys. Acta, Biomembr., 2016. **1858**(10): p. 2380-2389.
56. Qiu, L., et al., *Molecular dynamics simulations reveal the protective role of cholesterol in beta-amyloid protein-induced membrane disruptions in neuronal membrane mimics.* J. Phys. Chem B., 2018(1520-5207 (Electronic)).
57. Demel, R.A., et al., *Relation between various phospholipase actions on human red cell membranes and the interfacial phospholipid pressure in monolayers.* Biochim. Biophys. Acta, Biomembr., 1975. **406**(1): p. 97-107.
58. Kaganer, V.M., H. Möhwald, and P. Dutta, *Structure and phase transitions in Langmuir monolayers.* Rev. Mod. Phys., 1999. **71**(3): p. 779-819.
59. J.T. Davies, E.K.R., *Interfacial phenomena*. 1963, New York : Academic Press.
60. Rodríguez Patino, J.M., C.C. Sánchez, and M.R. Rodríguez Niño, *Morphological and Structural Characteristics of Monoglyceride Monolayers at the Air−Water Interface Observed by Brewster Angle Microscopy.* Langmuir, 1999. **15**(7): p. 2484-2492.
61. Csúcs, G. and J.J. Ramsden, *Interaction of phospholipid vesicles with smooth metal-oxide surfaces.* Biochimica et Biophysica Acta (BBA) - Biomembranes, 1998. **1369**(1): p. 61-70.

62. Richards, D.A., A. Maruani, and V. Chudasama, *Antibody fragments as nanoparticle targeting ligands: a step in the right direction.* Chemical Science, 2017. **8**(1): p. 63-77.
63. Gupta, A.K. and M. Gupta, *Synthesis and surface engineering of iron oxide nanoparticles for biomedical applications.* Biomaterials, 2005. **26**(18): p. 3995-4021.
64. Jinhao Gao, H.G.a.B.X., *Multifunctional Magnetic Nanoparticles: Design, Synthesis, and Biomedical Applications.* Acc. Chem. Res., 2009. **42 (8)**.
65. Parveen, S., R. Misra, and S.K. Sahoo, *Nanoparticles: a boon to drug delivery, therapeutics, diagnostics and imaging.* Nanomedicine, 2012. **8**(2): p. 147-166.
66. Richard, S., et al., *Iron oxide nanoparticle surface decorated with cRGD peptides for magnetic resonance imaging of brain tumors.* Biochim. Biophys. Acta, Gen. Subj., 2017. **1861**(6): p. 1515-1520.
67. Afsahi, S., et al., *Novel graphene-based biosensor for early detection of Zika virus infection.* Biosensors and Bioelectronics, 2018. **100**: p. 85-88.
68. Bothun, G.D., et al., *Anionic and Cationic Silver Nanoparticle Binding Restructures Net-Anionic PC/PG Monolayers with Saturated or Unsaturated Lipids.* Langmuir, 2017. **33**(1): p. 353–360.
69. Malvindi, M.A., et al., *Rod-Shaped Nanocrystals Elicit Neuronal Activity In Vivo.* Small, 2008. **4**: p. 1747–1755.
70. Dante, S., et al., *Selective Targeting of Neurons with Inorganic Nanoparticles: Revealing the Crucial Role of Nanoparticle Surface Charge.* ACS Nano, 2017. **11**(7): p. 6630-6640.
71. Xu, C., G.A. Tung, and S. Sun, *Size and Concentration Effect of Gold Nanoparticles on X-ray Attenuation As Measured on Computed Tomography.* Chem. Mater., 2008. **20**(13): p. 4167-4169.
72. Bailey, C.M., et al., *Size dependence of gold nanoparticle interactions with a supported lipid bilayer: A QCM-D study.* Biophys. Chem., 2015. **203-204**: p. 51-61.
73. Braydich-Stolle, L., et al., *In Vitro Cytotoxicity of Nanoparticles in Mammalian Germline Stem Cells.* Toxicol. Sci., 2005. **88**(2): p. 412-419.
74. Negoda, A., et al., *Engineered nanomaterial interactions with bilayer lipid membranes: screening platforms to assess nanoparticle toxicity.* Int. J. Biomed. Nanosci. Nanotechnol., 2013. **3**(1-2): p. 52-83.
75. Nel, A., et al., *Toxic Potential of Materials at the Nanolevel.* Science, 2006. **311**(5761): p. 622-627.
76. Atukorale, P.U., et al., *Structure–Property Relationships of Amphiphilic Nanoparticles That Penetrate or Fuse Lipid Membranes.* Bioconjugate Chem., 2018. **29**(4): p. 1131-1140.
77. Chen, H., et al., *In Vivo Study of Spherical Gold Nanoparticles: Inflammatory Effects and Distribution in Mice.* PLoS One, 2013. **8**(2): p. e58208.
78. Zhao, F., et al., *TiO2 nanoparticle interactions with supported lipid membranes - an example of removal of membrane patches.* RSC Adv., 2016. **6**(94): p. 91102-91110.
79. Verma, A.a.S., F. , *Effect of Surface Properties on Nanoparticle–Cell Interactions.* Small, 2010. **6**: p. 12–21.
80. Wang, B., et al., *Nanoparticle-induced surface reconstruction of phospholipid membranes.* Proc. Natl. Acad. Sci. U. S. A., 2008. **105**(47): p. 18171.
81. Torrano, A.A., et al., *Probing the interaction of oppositely charged gold nanoparticles with DPPG and DPPC Langmuir monolayers as cell membrane models.* Colloids Surf., B, 2013. **108**: p. 120-126.
82. Monticelli, L., et al., *Effects of carbon nanoparticles on lipid membranes: a molecular simulation perspective.* Soft Matter, 2009. **5**(22): p. 4433-4445.
83. Li, Y. and N. Gu, *Thermodynamics of Charged Nanoparticle Adsorption on Charge-Neutral Membranes: A Simulation Study.* The Journal of Physical Chemistry B, 2010. **114**(8): p. 2749-2754.
84. Bahrami, A.H., et al., *Wrapping of nanoparticles by membranes.* Advances in Colloid and Interface Science, 2014. **208**: p. 214-224.
85. Tortiglione, C., et al., *Fluorescent Nanocrystals Reveal Regulated Portals of Entry into and Between the Cells of Hydra.* PLoS One, 2009. **4**(11): p. e7698.

86. Marques, O. and T.F. Outeiro, *Alpha-synuclein: from secretion to dysfunction and death.* Cell Death &Amp;amp; Disease, 2012. **3**: p. e350.
87. Stefanis, L., *α-Synuclein in Parkinson's disease.* Cold Spring Harbor perspectives in medicine, 2012. **2**(2): p. a009399-a009399.
88. Yuan, Q., et al., *Highly stable and regenerative graphene–diamond hybrid electrochemical biosensor for fouling target dopamine detection.* Biosensors and Bioelectronics, 2018. **111**: p. 117-123.
89. Das, B., et al., *Biosynthesis of magnesium oxide (MgO) nanoflakes by using leaf extract of Bauhinia purpurea and evaluation of its antibacterial property against Staphylococcus aureus.* Materials Science and Engineering: C, 2018. **91**: p. 436-444.
90. Lin, K.-C., et al., *Biogenic nanoporous silica-based sensor for enhanced electrochemical detection of cardiovascular biomarkers proteins.* Biosensors and Bioelectronics, 2010. **25**(10): p. 2336-2342.
91. Rodriguez-Contreras, A., D. Guadarrama Bello, and A. Nanci, *Surface nanoporosity has a greater influence on osteogenic and bacterial cell adhesion than crystallinity and wettability.* Applied Surface Science, 2018. **445**: p. 255-261.
92. Kikuchi, T., et al., *Fabrication of anodic porous alumina via anodizing in cyclic oxocarbon acids.* Applied Surface Science, 2014. **313**: p. 276-285.
93. Chen, W., J.-S. Wu, and X.-H. Xia, *Porous Anodic Alumina with Continuously Manipulated Pore/Cell Size.* ACS Nano, 2008. **2**(5): p. 959-965.
94. Fawcett, D., et al., *Biocompatibility of nanometre scale porous anodic aluminium oxide membranes towards the RK 13 epithelial cell line: A preliminary study*. Vol. 3. 2015. 1583-1588.
95. Salerno, M., et al., *Adhesion and Proliferation of Osteoblast-Like Cells on Anodic Porous Alumina Substrates With Different Morphology.* IEEE Transactions on NanoBioscience, 2013. **12**(2): p. 106-111.
96. Chung, S.H., S.J. Son, and J. Min, *The nanostructure effect on the adhesion and growth rates of epithelial cells with well-defined nanoporous alumina substrates.* Nanotechnology, 2010. **21**(12): p. 125104.
97. Das, G., et al., *Fabrication of large-area ordered and reproducible nanostructures for SERS biosensor application.* Analyst, 2012. **137**(8): p. 1785-1792.
98. Toccafondi, C., et al., *Multifunctional substrates of thin porous alumina for cell biosensors.* Journal of Materials Science: Materials in Medicine, 2014. **25**(10): p. 2411-2420.
99. Gultepe, E., et al., *Nanoporous inorganic membranes or coatings for sustained drug delivery in implantable devices.* Adv Drug Deliv Rev., 2010(1872-8294 (Electronic)).
100. Toccafondi, C., et al., *Fabrication of Gold-Coated Ultra-Thin Anodic Porous Alumina Substrates for Augmented SERS.* Materials (Basel, Switzerland), 2016. **9**(6): p. 403.
101. Swan, E.E., T.A. Popat Kc Fau - Desai, and T.A. Desai, *Peptide-immobilized nanoporous alumina membranes for enhanced osteoblast adhesion.* Biomaterials, 2005(0142-9612 (Print)).
102. Carbone, L., et al., *Synthesis and Micrometer-Scale Assembly of Colloidal CdSe/CdS Nanorods Prepared by a Seeded Growth Approach.* Nano Lett., 2007. **7**(10): p. 2942-2950.
103. Di Corato, R., et al., *Water solubilization of hydrophobic nanocrystals by means of poly(maleic anhydride-alt-1-octadecene).* J. Mater. Chem., 2008. **18**(17): p. 1991-1996.
104. Gharahdaghi, F., et al., *Mass spectrometric identification of proteins from silver-stained polyacrylamide gel: A method for the removal of silver ions to enhance sensitivity.* ELECTROPHORESIS, 1999. **20**(3): p. 601-605.
105. Quarta, A., et al., *Polymer coated inorganic nanoparticles: tailoring the nanocrystal surface for designing nanoprobes with biological implications.* Nanoscale, 2012. **4**(11): p. 3319-3334.
106. Kankare, J., *Sauerbrey Equation of Quartz Crystal Microbalance in Liquid Medium.* Langmuir, 2002. **18**(18): p. 7092-7094.

107. Yang Z Fau - Dixon, M.C., et al., *Quantification of the Mass and Viscoelasticity of Interfacial Films on Tin Anodes Using EQCM-D.* Appl. Mater Interfaces, 2015(1944-8252 (Electronic)).
108. Richter, R.P., R. Bérat, and A.R. Brisson, *Formation of Solid-Supported Lipid Bilayers: An Integrated View.* Langmuir, 2006. **22**(8): p. 3497-3505.
109. Langmuir, I., *The Constitution And Fundamental Properties Of Solids And Liquids.* Journal of the American Chemical Society, 1917. **39**(9): p. 1848-1906.
110. Blodgett, K.B., *Films Built by Depositing Successive Monomolecular Layers on a Solid Surface.* Journal of the American Chemical Society, 1935. **57**(6): p. 1007-1022.
111. Vollhardt, D., *Morphology and phase behavior of monolayers.* Adv. Colloid Interface Sci., 1996. **64**: p. 143-171.
112. Mohwald, H., *Phospholipid and phospholipid-protein monolayers at the air/water interface.* Annu. Rev. Phys. Chem., 1990. **41**: p. 441-476.
113. Schram, V., H.N. Lin, and T.E. Thompson, *Topology of gel-phase domains and lipid mixing properties in phase-separated two-component phosphatidylcholine bilayers.* Biophys. J., 1996. **71**(4): p. 1811-1822.
114. Picas, L., F. Rico, and S. Scheuring, *Direct Measurement of the Mechanical Properties of Lipid Phases in Supported Bilayers.* Biophys. J., 2012. **102**(1): p. L01-L03.
115. Wacklin, H.P., *Composition and Asymmetry in Supported Membranes Formed by Vesicle Fusion.* Langmuir, 2011. **27**(12): p. 7698-7707.
116. Mikelonis, A.M., S. Youn, and D.F. Lawler, *DLVO Approximation Methods for Predicting the Attachment of Silver Nanoparticles to Ceramic Membranes.* Langmuir, 2016. **32**(7): p. 1723-1731.
117. Anandarajah, A. and J. Chen, *Single Correction Function for Computing Retarded van der Waals Attraction.* J. Colloid Interface Sci., 1995. **176**(2): p. 293-300.
118. Petosa, A.R., et al., *Aggregation and Deposition of Engineered Nanomaterials in Aquatic Environments: Role of Physicochemical Interactions.* Environ. Sci. Technol., 2010. **44**(17): p. 6532-6549.
119. Song, J.E., et al., *Hydrophobic Interactions Increase Attachment of Gum Arabic- and PVP-Coated Ag Nanoparticles to Hydrophobic Surfaces.* Environ. Sci. Technol., 2011. **45**(14): p. 5988-5995.
120. Chan, J., et al., *Soret Coefficients for Aqueous Polyethylene Glycol Solutions and Some Tests of the Segmental Model of Polymer Thermal Diffusion.* J. Solution Chem., 2003. **32**(3): p. 197-214.
121. Robert, P., *Principles of Cellular Engineering*. 1st ed. 2006. 320.
122. Israelachvili, J.N. and H. Wennerstroem, *Hydration or steric forces between amphiphilic surfaces?* Langmuir, 1990. **6**(4): p. 873-876.
123. Fleischer, C.C. and C.K. Payne, *Nanoparticle–Cell Interactions: Molecular Structure of the Protein Corona and Cellular Outcomes.* Accounts of Chemical Research, 2014. **47**(8): p. 2651-2659.
124. Pfeiffer, C., et al., *Interaction of colloidal nanoparticles with their local environment: the (ionic) nanoenvironment around nanoparticles is different from bulk and determines the physico-chemical properties of the nanoparticles.* J. R. Soc., Interface, 2014(1742-5662 (Electronic)).
125. Hodgkin, A.L. and A.F. Huxley, *A quantitative description of membrane current and its application to conduction and excitation in nerve.* The Journal of Physiology, 1952. **117**(4): p. 500-544.
126. deCharms, R.C. and M.M. Merzenich, *Primary cortical representation of sounds by the coordination of action-potential timing.* Nature, 1996. **381**: p. 610.
127. Wu, P.-Y., et al., *Functional decreases in P2X7 receptors are associated with retinoic acid-induced neuronal differentiation of Neuro-2a neuroblastoma cells.* Cellular Signalling, 2009. **21**(6): p. 881-891.
128. Lago, J., et al., *Tetrodotoxin, an Extremely Potent Marine Neurotoxin: Distribution, Toxicity, Origin and Therapeutical Uses.* Marine drugs, 2015. **13**(10): p. 6384-6406.
129. Goldman, D.E., *Potential, Impedance, And Rectification In Membranes.* The Journal of General Physiology, 1943. **27**(1): p. 37.

BEILSTEIN JOURNAL OF NANOTECHNOLOGY

Surface-enhanced Raman scattering of self-assembled thiol monolayers and supported lipid membranes on thin anodic porous alumina

Marco Salerno*[1], Amirreza Shayganpour[1,2], Barbara Salis[1,2] and Silvia Dante[1]

Full Research Paper

Open Access

Address:
[1]Department of Nanophysics, Istituto Italiano di Tecnologia, via Morego 30, I-16163 Genova, Italy and [2]Department of Bioengineering and Robotics, University of Genova, viale Causa 13, I-16145 Genova, Italy

Email:
Marco Salerno* - marco.salerno@iit.it

* Corresponding author

Keywords:
anodic porous alumina; SERS; nanopores; supported lipid bilayers; thiols

Beilstein J. Nanotechnol. **2017,** *8,* 74–81.
doi:10.3762/bjnano.8.8

Received: 15 July 2016
Accepted: 12 December 2016
Published: 09 January 2017

This article is part of the Thematic Series "Self-assembly of nanostructures and nanomaterials II".

Guest Editor: I. Berbezier

Abstract

Thin anodic porous alumina (tAPA) was fabricated from a 500 nm thick aluminum (Al) layer coated on silicon wafers, through single-step anodization performed in a Teflon electrochemical cell in 0.4 M aqueous phosphoric acid at 110 V. Post-fabrication etching in the same acid allowed obtaining tAPA surfaces with ≈160 nm pore diameter and ≈80 nm corresponding wall thickness to be prepared. The tAPA surfaces were made SERS-active by coating with a thin (≈25 nm) gold (Au) layer. The as obtained tAPA–Au substrates were incubated first with different thiols, namely mercaptobenzoic acid (MbA) and aminothiol (AT), and then with phospholipid vesicles of different composition to form a supported lipid bilayer (SLB). At each step, the SERS substrate functionality was assessed, demonstrating acceptable enhancement (≥100×). The chemisorption of thiols during the first step and the formation of SLB from the vesicles during the second step, were independently monitored by using a quartz crystal microbalance with dissipation monitoring (QCM-D) technique. The SLB membranes represent a simplified model system of the living cells membranes, which makes the successful observation of SERS on these films promising in view of the use of tAPA–Au substrates as a platform for the development of surface-enhanced Raman spectroscopy (SERS) biosensors on living cells. In the future, these tAPA–Au-SLB substrates will be investigated also for drug delivery of bioactive agents from the APA pores.

Introduction

Anodic porous alumina (APA) is a layered material usually obtained in thick form (≈10 µm thickness scale) from electrochemical anodization in the acidic aqueous electrolyte of aluminum (Al) foils [1]. In APA, the control of pore size, pore density and porosity is achieved by changing the anodization voltage during the fabrication and the etching parameters during the post-fabrication treatment [2]. It is widely recognized that the APA surface is biocompatible with practically all cell types and

provides a means of controlling the surface roughness [3,4], the latter of which can play an important role in the adhesion and proliferation of cells [5-7]. The self-ordered nano-structured APA, also demonstrated recently as a possible nanolithographic mask [8,9] and for chemical sensors and biosensors [10], after coating with noble metals can be used for plasmonics-based enhanced spectroscopy such as in surface-enhanced Raman spectroscopy (SERS) [11-14].

In recent years, the thin form of APA (tAPA), resulting from anodization of Al films of less than 1 μm thickness, has been increasingly used because it can be better integrated into applications involving optical microscopy inspection, which requires flat planar substrates. Moreover, it allows to move toward a more robust engineering of APA surfaces by exploiting the standard microtechnology of photolithography, thereby paving the way to large scale fabrication in possible future devices.

The enhancement factor in APA-based SERS can be as high as 1000, which means that the technique may detect molecules [15]. Additionally, the pores in tAPA can potentially serve as nano-wells for localized drug delivery [16,17]. In fact, while lower in loading capacity with respect to thick APA [18], 500 nm tAPA can still allocate a significant amount of bioactive compounds, representing a trade-off between the former case of maximized loading and the case of ultra-thin APA showing the highest SERS enhancement [19]. Finally, the controlled roughness of APA could also improve the physisorption of coating layers of functional materials [20,21].

The main component of the biological membrane that separates and protects the interior of all living cells from the outside environment is a phospholipid bilayer. For this reason, as well as for the complexity of real samples of living cells, we decided to test the tAPA–Au SERS-active substrates on SLBs in phosphate-buffered saline (PBS) buffer solution, which provide an excellent model system to mimic the native cellular membranes [22].

In the present work, the fabrication and modification of tAPA aiming at its exploitation as a functional substrate for biosensing based on SERS effect are presented. In particular, it is reported on SERS effect on SLBs obtained from spontaneous lipid vesicle fusion and representing a simplified model of living cells membrane. Since the vesicle fusion is not trivial to achieve on Au surfaces, we first functionalized the Au with self-assembled monolayers (SAM) of thiols, to provide the appropriate surface condition to allow SLB formation. SERS effect was tested and proved for each fabrication step of the system.

Experimental

tAPA fabrication and modification to achieve SERS-activity

An ≈500 nm thick Al layer was first coated on a silicon wafer by an electron-beam evaporation system PVD75 (Kurt J. Lesker Ltd., UK) working at a base pressure of 10^{-6} Torr with a deposition rate of 0.5–1 Å/s. tAPA was fabricated in a single-step (≈15 min) anodization performed at 110 V in 0.4 M phosphoric acid electrolyte at a bath temperature of ≈15 °C. Post-fabrication etching in the same electrolyte for 20 min at room temperature (RT) plus 15 min at 35 °C allowed to obtain tAPA with ≈160 nm pore size and ≈80 nm wall thickness. After thoroughly rinsing with de-ionized water, blowing dry with nitrogen and dehydrating on a hotplate set at 100 °C for 15 min, the tAPA was overcoated by the same electron-beam evaporation system with a ≈25 nm thick Au layer to make it SERS-active. More details on similar fabrication procedure can be found in references [12,13].

The characteristic size of tAPA pores was obtained by scanning electron microscope (SEM) imaging with a JSM-7500F (Jeol, Japan) and subsequent grain analysis carried out with Igor 6.22 (Wavemetrics, OR, USA).

Incubation of thiols and fabrication of lipid vesicles

Different thiols were used in combination with the different lipids to be coated onto them by electrostatically-driven physisorption. We used two thiols, namely 4-mercaptobenzoic acid (MbA) and 11-amino-1-undecanethiol hydrochloride (AT), from Sigma (Milan, Italy), and three lipids, namely 1-palmitoyl-2-oleoyl-*sn*-glycero-3-phosphocholine (POPC), 1-palmitoyl-2-oleoyl-*sn*-glycero-3-phospho-L-serine (POPS) and, 1,2-dioleoyl-3-trimethylammoniumpropane (DOTAP), from Avanti Polar Lipids (Alabaster, Alabama, US). All solvents were purchased from Sigma-Aldrich.

First, the substrates were incubated at rt for 2 h with a 1 mM aqueous solution of the thiol molecule, either MbA or AT, to let the sulfur of the –SH group bind covalently to the Au surface (chemisorption). The substrates were then gently washed with their aqueous solutions and dried under nitrogen flow.

All the lipids were dissolved in chloroform/methanol 2:1 vol/vol, dried under a gentle nitrogen flux in a test tube, and put under a mild vacuum overnight to remove all solvent traces. POPC/POPS in a 9:1 mol/mol ratio and DOTAP were then re-suspended in PBS at a 5 g/L concentration, let to swell for 30 min, and extruded 11 times through a polycarbonate filter (Whatman, USA) with 100 nm pore diameter to form unilamellar vesicles.

Preparation of the Raman target analytes: SLBs

The lipid vesicles were diluted to 0.5 g/L in the PBS buffer and vortexed immediately before use. The thiol SAM was incubated overnight with the lipid vesicle dispersion, to allow vesicle physisorption and fusion onto the substrate. The following day the samples were carefully washed with PBS three times to remove the exceeding vesicles.

For the cationic lipids (namely DOTAP), we used a thiolated molecule that presents a positively charged group at its end. This is MbA, whose COOH group is protonated in PBS buffer to COO^-. For the anionic lipid mixture (namely POPC/POPS) AT was used, which becomes positive in aqueous solution because of the terminal amino group.

SERS measurements

SERS measurements were performed with a micro-Raman spectrometer inVia (Renishaw, UK) equipped with the software program WiRE 3.2. We used for excitation a laser with 785 nm wavelength and 100 mW power, equipped for dispersion with a grating with 1200 grooves/mm. For detection microscope objectives with a magnification of 50× (NA: 0.75) and 60× (water immersion, NA: 1.0) were used. The spectra were collected in the 300–3200 cm^{-1} spectral range.

The SERS enhancement factor G achieved by employing tAPA–Au with respect to the flat Au on silicon substrate can be estimated by using a simple formula:

$$G = \frac{P_{\mathrm{Ref}}\ t_{\mathrm{Ref}}}{P_{\mathrm{SERS}}\ t_{\mathrm{SERS}}} \times \frac{A_{\mathrm{Ref}}}{A_{\mathrm{SERS}}} \times \frac{I_{\mathrm{SERS}}}{I_{\mathrm{Ref}}}. \qquad (1)$$

where P, t, A and I are laser power, accumulation time, active area for molecule adsorption and Raman intensity of the specific band, respectively [13]. The subscripts, SERS and Ref, indicate SERS and Raman measurements on tAPA–Au and on flat Au substrates, respectively.

QCM-D characterization of adsorption

A quartz microbalance Z500 (KSV Instruments, Finland) was used for the QCM-D experiments. Au coated AT-cut quartz crystals (QSense, Sweden) with a 5 MHz fundamental resonance frequency were used. Before each experiment, the quartz sensor was first cleaned in a UV/Ozone ProCleaner (BioForce Nanoscience, US) for 10 min, then washed with milli-Q (18.2 MΩ·cm resistivity) water, dried under nitrogen flux and cleaned again for 10 min in the ozone cleaner.

The sensor was then mounted in the measurement chamber. The chamber was filled with proper buffer (aqueous solution for thiols, PBS for DOTAP vesicles and milli-Q water for POPC/POPS vesicles), and left to reach an equilibrium (≈30 min) before injecting the solution of interest. 3 mL of solution (1 mM thiols in aqueous solution, and a concentration of 0.25 g/L for both DOTAP in PBS and POPC/POPS in milli-Q) where then injected in the measurement chamber and left until the adsorption process reached an end (overnight measurement for thiols, 2 h for vesicles). The sensor was then rinsed with the proper buffer solution. If not stated otherwise, changes in frequency and dissipation of the seventh overtone (35 MHz) are shown; all experiments were carried out at a temperature of 22 °C.

Results and Discussion

SERS-active tAPA–Au substrates

The control of the geometrical features of nanostructured substrates is of critical importance in SERS [23]. The SEM images reported in Figure 1 show the good control achieved in both mean pore size and its dispersion and prove the long range uniformity of the surfaces with the Au coating to make it plasmonic-active.

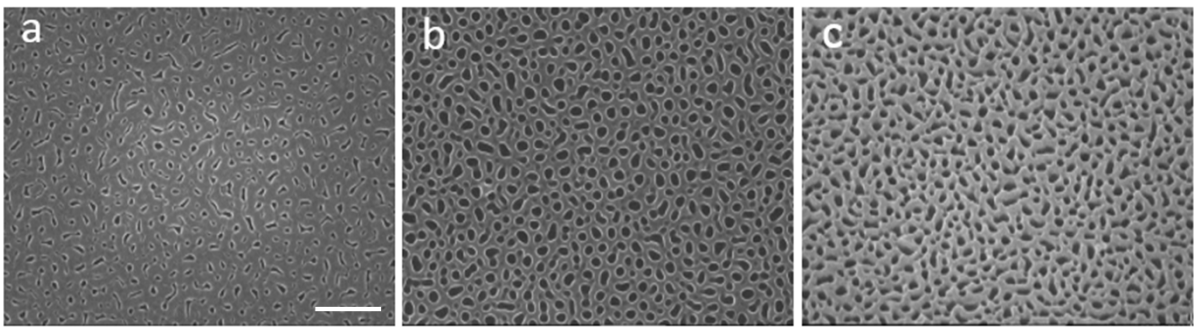

Figure 1: SEM images (20,000× magnification, scale bar 1 μm) of tAPA substrates (thickness ≈500 nm), a) as-prepared, b) after pore widening, and c) after 25 nm Au coating.

tAPA–Au substrates could possibly be used as a carrier layer for local drug delivery [24], as a substrate for living cell cultures thanks to its controlled porosity [3-7], and for SERS [25]. However, since SERS is a surface-only effect, this sensitive detection will be limited to the top of the tAPA–Au substrates, i.e., to the bottom of the living cells, where they would adhere to the nanoporous substrate.

SERS enhancement due to tAPA–Au on thiols, lipids, and thiol–lipid systems

The Raman measurements were performed first on the thiol molecules. We started from the raw materials, in powder form, to obtain reference spectra for future comparison and best identification of the typical bands. Then, we measured the Raman scattering of the thiols adsorbed to flat Au substrates. For technical reasons of SLBs assembly, the two thiols selected, MbA and AT, in ethanol and PBS solutions have a negatively or positively charged group, respectively.

The spectra of the thiols powder on flat Au, along with the respective molecular structures, are shown in Figure 2a. In Figure 2b the spectra of the SAM of the same thiols obtained after incubation on flat Au from 1 mM water solution for 2 h at RT are shown. The subsequent step was the deposition of the thiol molecules for the formation of SAM onto tAPA–Au and the observation of the respective spectra. The nanopores in the oxide under the Au, which are replicated by the top Au surface thanks to the low Au thickness of ≈25 nm, allowed for SERS effect. In Figure 2c we report the typical Raman spectra obtained on tAPA–Au for both MbA and AT.

The spectra of each thiol in all forms (pristine powder and film adsorbed onto the flat Au and tAPA–Au substrate) look similar. MbA present two major peaks at ≈1593 and ≈1076 cm^{-1}, which can be ascribed to aromatic ring vibrations, and also at ≈1181 and at ≈1290 cm^{-1}, which belong to C–H mode [26-28]. AT presents the major peaks at ≈1434 and ≈1477 cm^{-1} assigned to the C–H and at ≈1074 cm^{-1} assigned to the N–H, while the peak at ≈1074 cm^{-1} belongs to the C–C stretching.

In Supporting Information File 1, Figure S1 again the Raman spectra of both thiol SAMs, coupled according to the same thiol

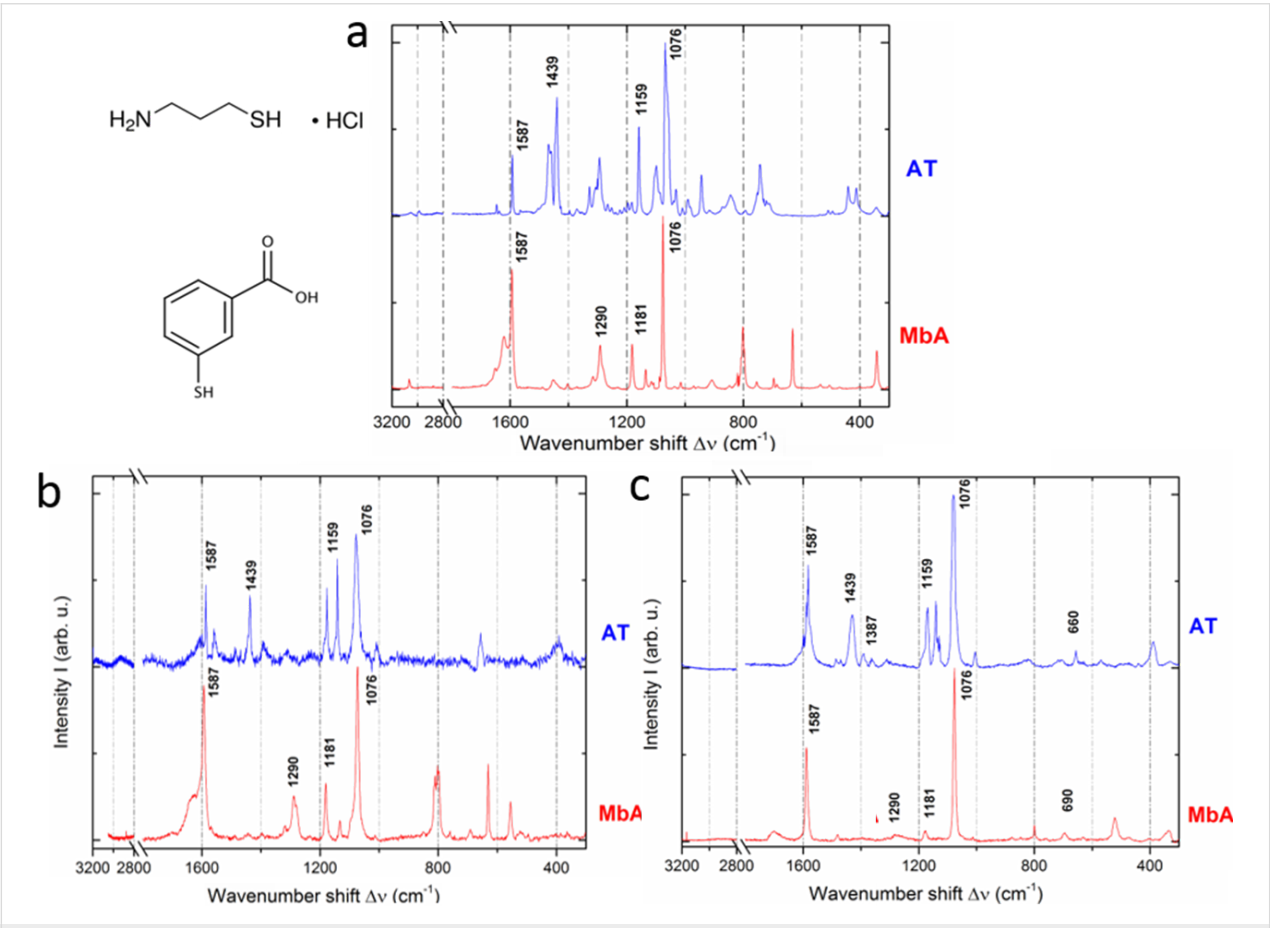

Figure 2: Raman spectra of thiols a) in powder form (with their molecular structures); b) in flat film form, after adsorption to the flat Au substrates from water solution; c) in film form on tAPA–Au.

deposited on the different substrates of flat Au and tAPA–Au, are presented, for easier visualization of the substrate effect. It appears clearly that on tAPA–Au the major characteristic peaks of both MbA and AT are highly enhanced. Taking into account the measurement parameters (i.e., t_{Ref} and t_{SERS} both 10 s, while P_{Ref} and P_{SERS} are 100 and 1, respectively), a G factor of approximately 600 and 1000 was calculated for MbA and AT, respectively. The SERS effect of the nanophotonic tAPA structure, after coating with Au and thus thanks to the localized surface plasmon resonances of this thin film, emerges. The same effect may also be used on the SLBs, at the later stage of the model system fabrication.

For the selected lipids, we first tested the Raman spectra of the powders and then of the SLB form, on both the flat Au and nanoporous tAPA–Au. The molecular structure and Raman spectra of lipids in powder form are shown in Figure 3.

The molecules of choice, i.e., POPC and POPS, are two glycerophospholipids largely present in real cellular membranes. In particular, we prepared a mixture of POPC and POPS suspended in PBS with the molar ratio of 8:2, in order to resemble the plasma membrane composition both for charge and acyl chain length and unsaturation grade. However, the reason for the choice of DOTAP is technical, associated with the fabrication of artificial bilayer membranes [29,30].

The lipids are larger molecules than the thiols and present richer spectra, at least in the powder form. The main features in their Raman spectra depend on the hydrocarbon chain, and can be ascribed to scissoring and twisting of CH_2 and CH_3 and to stretching of C–C and C–H. More precisely, the bands identified in the higher wavenumber region appear at 3007 cm^{-1} (unsaturated =CH stretching), 2882 cm^{-1} (CH_2 Fermi resonance) and 2847 cm^{-1} (CH_2 symmetric stretching). The middle wavenumber region presents bands at 1737 cm^{-1} (C=O ester stretching), 1657 cm^{-1} (C=C stretching), 1442 cm^{-1} (CH_2 scissoring), 1300 cm^{-1} (CH_2 twisting) and 1267 cm^{-1} (=C–H in-plane deformation). In the lower wavenumber region, the C–C stretching emerges as a broad band around 1090 cm^{-1}. In particular, two contributions at 1065 and 1089 cm^{-1} appear with a shoulder at 1125 cm^{-1}. Additional bands appear at 719 and 876 cm^{-1} that are ascribed to the symmetric and asymmetric stretching of choline $N^+(CH_3)_3$, respectively [31,32].

The lipids were further investigated on tAPA–Au substrates, for the possible occurrence of SERS. Figure 4 shows Raman spectra for three mixtures of lipids in SLBs form, on both flat Au and tAPA–Au.

From the comparison of the spectra of lipids in SLBs form versus those in powder form, the most interesting difference observed is that in the films several peaks disappear or are weaker. Whereas some form of quenching can't be excluded, this is probably due to light polarization constraints in the ordered geometry of the molecular film, where not all modes of chemical groups may be excited, as it can be instead in the assembly of randomly oriented microcrystals of the powders [33].

It appears that on tAPA–Au as compared to flat Au the characteristic thiol peaks are still present and enhanced. As a consequence, for MbA the major peaks at ≈1590 and ≈1080 cm^{-1}, ascribed to aromatic ring vibrations, and ≈1181 cm^{-1}, ascribed to C–H deformation, appear. Also AT presents the major peaks

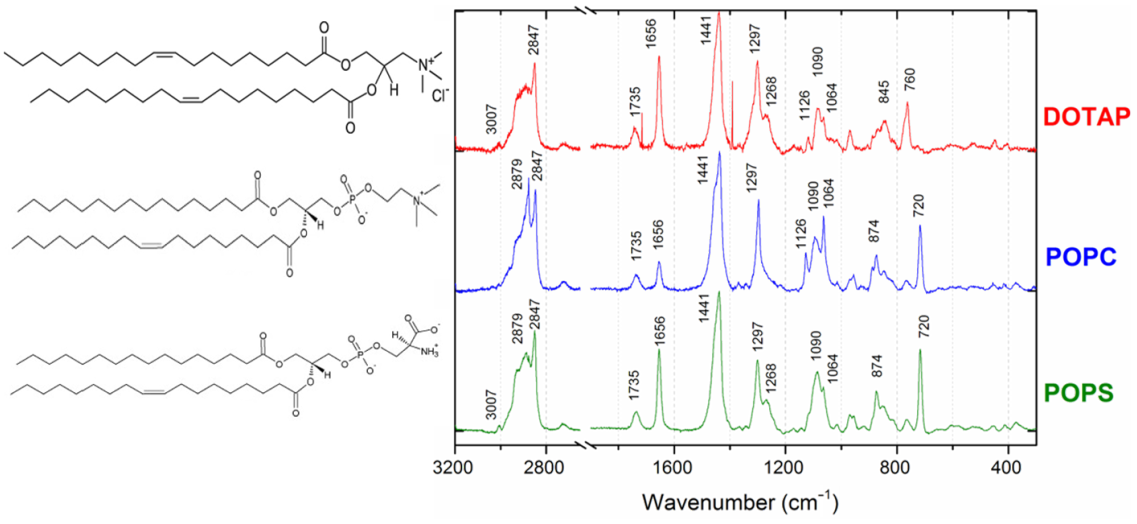

Figure 3: Raman spectra of lipids in powder form on flat Au substrates, with their molecular structures.

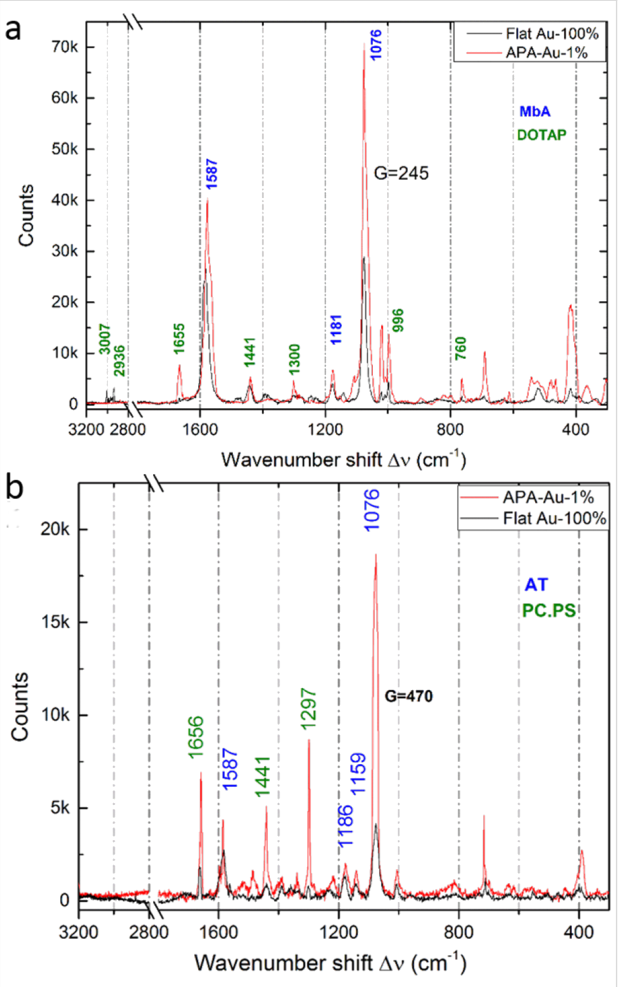

Figure 4: Raman spectra of the thiol-SLB systems on both flat Au and tAPA–Au: a) MbA and DOTAP, b) AT and POPC/POPS blend.

at ≈1580, ≈1159 and ≈1074 cm^{-1}, due to C–NH, N–H wagging and C–C stretching mode, respectively.

Additionally, in Figure 4 we have bands from the lipids, namely ≈1656 cm^{-1} (C=C stretching), ≈1440 cm^{-1} (CH_2 scissoring), ≈1300 cm^{-1} (CH_2 twisting), ≈1267 cm^{-1} (=C–H in-plane deformation), and ≈719 cm^{-1} (choline) [34].

The values of enhancement G due to the tAPA–Au nanostructured substrates have been calculated according to Equation 1. Since the peaks on tAPA–Au are 2–4 times higher in the presence of 100 times lower laser power, a G of ≈250 at ≈1076 cm^{-1} and 500 at ≈1076 cm^{-1} is obtained for the thiol–lipid system of MbA–DOTAP and AT–POPC/POPS, respectively.

QCM-D measurements

The lipid adsorption process on Au was independently monitored by QCM-D technique. This method allows the quantification of the adsorbed mass onto the surface of a vibrating Au-coated quartz electrode through the measurement of the mass-induced frequency shift. Additionally, the measurement of the dissipation gives indication about the viscoelastic properties of the adsorbed layer. The quartz–Au substrate was thus used as a control for success of the incubation of the tAPA–Au substrates in the lipid dispersion. In a preliminary step (data not shown) we have monitored the chemisorption of thiols onto the Au-coated QCM-D sensors; the functionalized sensors where then exposed to the lipid vesicles and the process of adsorption was monitored.

The QCM-D time-evolution profiles presented in Figure 5a,b show that the lipids successfully adsorbed to the Au surface of quartz in both cases. However, the two lipid systems behave differently. For DOTAP on MbA (Figure 5a) one can observe a big shift in frequency ($\Delta f \approx -1135$ Hz) and a high value of dissipation ($D \approx 40 \times 10^{-6}$), indicating the adsorption on the sensor's surface of a viscoelastic structure [35]. DOTAP vesicles do not fuse on Au functionalized with MbA, rather entire vesicles are adsorbed instead. On the contrary, for POPC/POPS on AT (Figure 5b) the frequency shift is low ($\Delta f \approx -157$ Hz for the reported 7th harmonic) and the value of dissipation is close to zero, indicating the adsorption of a smaller mass with more rigid structure on the surface. The reason may be that the POPC/POPS vesicles rupture in contact with the AT-functionalized Au and an SLB forms on the surface [36,37]. Table 1 shows the thickness values of SAM and adsorbed layers obtained with the QCM software. The values have been retrieved by using the Sauerbrey model of rigid layers for the SLBs and the Voigt model of viscoelastic layers for the adsorbed vesicles, assuming for the material densities the following values: $\rho_{AT} = 0.9$ g/cm^3 for AT, $\rho_{MbA} = 1.34$ g/cm^3 for MbA, and $\rho_v = 1$ g/cm^3 for vesicles (made mostly of water), according to references [38,39]. The data confirm that DOTAP vesicles adsorb on the sensor without rupturing, with a thickness of the adsorbed layer of ≈90 nm. POPC/POPS vesicles create an SLB on the sensor with a thickness of ≈4 nm. When the formation of an SLB occurs, the fingerprint region is not visible. As already pointed out in Figure 4, we ascribe this effect to the orientation of the molecules and the polarization of the incoming beam. When vesicles are adsorbed on the surface, all the characteristic peaks of the lipid molecules are expected from the Raman spectra, since the vesicles contain all molecular orientations. In accordance to this, the Raman spectra of DOTAP collected from QCM sensor show a signal in the lipid fingerprint region which is different from the spectra collected on the Au–tAPA surface that are flat in the 2800–3000 cm^{-1} region. This indicates that the porosity of the substrate may influence the vesicle fusion process. This finding is still under further investigation.

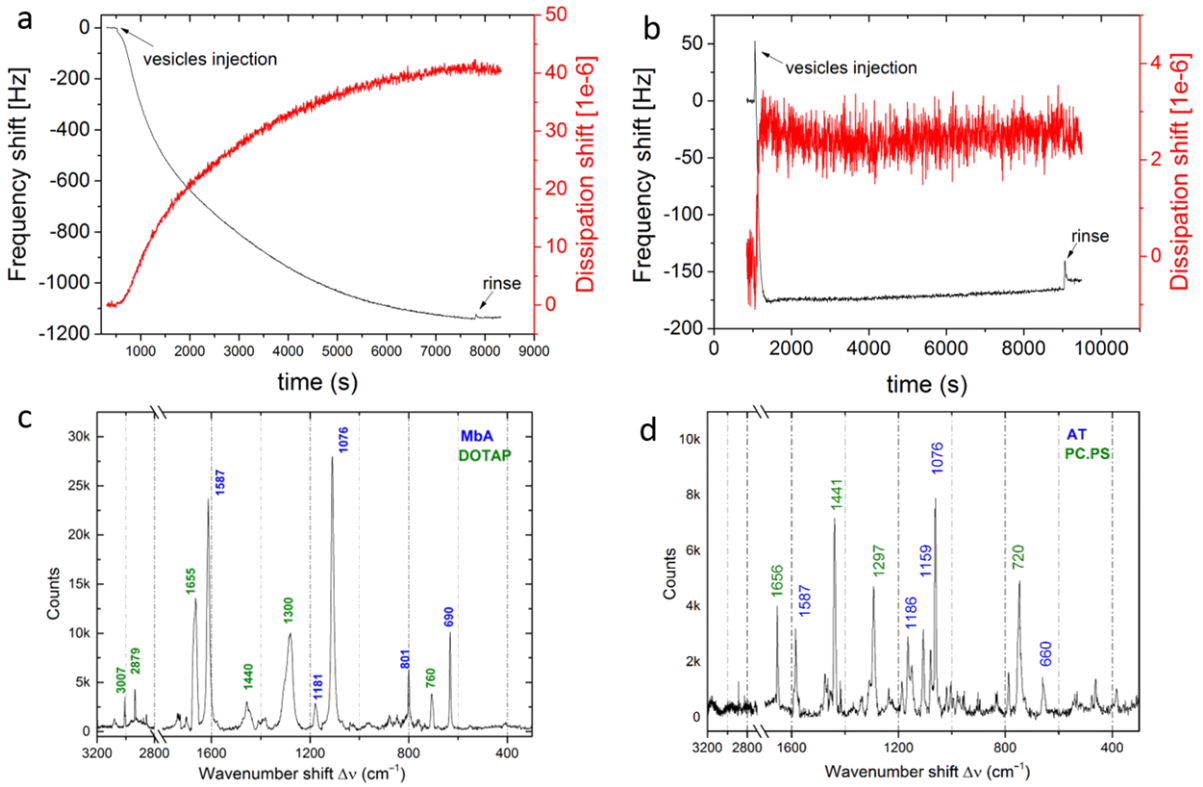

Figure 5: a,b) QCM-D measurements of shift in frequency and dissipation of a) DOTAP on MbA substrate, and b) POPC/POPS on AT substrate; c,d) respective Raman spectra on QCM sensors coated with c) MbA and DOTAP, and d) AT and POPC/POPS blend.

Table 1: Shift in frequency Δ*f* and shift in dissipation *D* and relative standard deviations of the layers adsorbed on the QCM sensor's surface. Every experiment was repeated three times.

Solution	*d* [nm]	std dev [nm]	Δ*f* [Hz]	std dev [Hz]	*D* [10^{-6}]	std dev [10^{-6}]
POPC/POPS (milli-Q) AT	3.9	0.1	−92	14	1.5	0.4
DOTAP (PBS) MbA	96	3.5	−1054	19.4	41.5	0.2

In Supporting Information File, Figure S1 the spectra of both lipids are presented again, grouped according to the different types of substrates, which makes it possible to compare the effect of the substrate on the resulting spectra.

Conclusion

We successfully fabricated tAPA substrates on silicon wafer through anodization of ≈500 nm thickness and post-production etching, resulting in oxide films with pores of ≈160 nm size and ≈80 nm wall thickness. After coating with a ≈25 nm Au layer covering the tAPA features, our substrates become SERS-active and allow for an investigation of the chemical vibrations of molecules, as demonstrated by sensitive Raman measurements on bare thiols and on their combinations with lipid membranes, namely MbA with DOTAP and AT with POPC/POPS. The enhancement factor was estimated to be 500 to 1000 on tAPA–Au with respect to the flat Au surface and to the silicon substrate. The chemisorption of thiols and lipids was confirmed on quartz-Au by QCM-D technique. The present results point to the possible future use of the tAPA–Au surfaces as disposable substrates for assessing the cell functionality in biosensors/bioassays.

Supporting Information

Supporting Information File 1

Additional figures.
[http://www.beilstein-journals.org/bjnano/content/supplementary/2190-4286-8-8-S1.pdf]

References

1. Diggle, J. W.; Downie, T. C.; Goulding, C. W. *Chem. Rev.* **1969,** *69,* 365–405. doi:10.1021/cr60259a005
2. Sulka, G. D. *Nanostructured Materials in Electrochemistry;* Wiley-VCH: Hoboken, NJ, U.S.A., 2008; pp 1–116.
3. Karlsson, M.; Johansson, A.; Tang, L.; Boman, M. *Microsc. Res. Tech.* **2004,** *63,* 259–265. doi:10.1002/jemt.20040
4. Salerno, M.; Caneva-Soumetz, F.; Pastorino, L.; Patra, N.; Diaspro, A.; Ruggiero, C. *IEEE Trans. NanoBioscience* **2013,** *12,* 106–111. doi:10.1109/TNB.2013.2257835
5. Gentile, F.; Tirinato, L.; Battista, E.; Causa, F.; Liberale, C.; di Fabrizio, E. M.; Decuzzi, P. *Biomaterials* **2010,** *31,* 7205–7212. doi:10.1016/j.biomaterials.2010.06.016
6. Ross, A. M.; Jiang, Z.; Bastmeyer, M.; Lahann, J. *Small* **2012,** *8,* 336–355. doi:10.1002/smll.201100934
7. Rahmany, M. B.; Van Dyke, M. *Acta Biomater.* **2013,** *9,* 5431–5437. doi:10.1016/j.actbio.2012.11.019
8. Yanagishita, T.; Masuda, H. *AIP Adv.* **2016,** 6.
9. Yanagishita, T.; Masuda, H. *Electrochim. Acta* **2015,** *184,* 80–85. doi:10.1016/j.electacta.2015.10.019
10. Santos, A.; Kumeria, T.; Losic, D. *TrAC, Trends Anal. Chem.* **2013,** *44,* 25–38. doi:10.1016/j.trac.2012.11.007
11. Chung, A. J.; Huh, Y. S.; Erickson, D. *Nanoscale* **2011,** *3,* 2903–2908. doi:10.1039/c1nr10265f
12. Toccafondi, C.; Thorat, S.; La Rocca, R.; Scarpellini, A.; Salerno, M.; Dante, S.; Das, G. *J. Mater. Sci.: Mater. Med.* **2014,** *25,* 2411–2420. doi:10.1007/s10856-014-5178-4
13. Toccafondi, C.; La Rocca, R.; Scarpellini, A.; Salerno, M.; Das, G.; Dante, S. *Appl. Surf. Sci.* **2015,** *351,* 738–745. doi:10.1016/j.apsusc.2015.05.169
14. Kneipp, K.; Kneipp, H.; Kneipp, J. *Acc. Chem. Res.* **2006,** *39,* 443–450. doi:10.1021/ar050107x
15. Nie, S.; Emory, S. E. *Science* **1997,** *275,* 1102–1106. doi:10.1126/science.275.5303.1102
16. Salerno, M.; Thorat, S. *13th Ceram. Cells Tissues. Regen. nanomedicine, tissue Genet. Eng. role Ceram.* **2011**, 171.
17. Gultepe, E.; Nagesha, D.; Sridhar, S.; Amiji, M. *Adv. Drug Delivery Rev.* **2010,** *62,* 305–315. doi:10.1016/j.addr.2009.11.003
18. Aw, M. S.; Bariana, M.; Losic, D. Nanoporous Anodic Alumina for Drug Delivery and Biomedical Applications. In *Nanoporous Alumina: Fabrication, Structure, Properties and Applications;* Losic, D.; Santos, A., Eds.; Springer Series in Materials Science, Vol. 219; Springer: Berlin, Germany, 2015; pp 319–354. doi:10.1007/978-3-319-20334-8_11
19. Toccafondi, C.; Zaccaria, R. P.; Dante, S.; Salerno, M. *Materials* **2016,** *9,* 403–414. doi:10.3390/ma9060403
20. Swan, E. E. L.; Popat, K. C.; Desai, T. A. *Biomaterials* **2005,** *26,* 1969–1976. doi:10.1016/j.biomaterials.2004.07.001
21. Chang, P.-C.; Liu, B.-Y.; Liu, C.-M.; Chou, H.-H.; Ho, M.-H.; Liu, H.-C.; Wang, D.-M.; Hou, L.-T. *J. Biomed. Mater. Res., Part A* **2007,** *81,* 771–780. doi:10.1002/jbm.a.31031
22. Tamm, L. K.; McConnell, H. M. *Biophys. J.* **1985,** *47,* 105–113. doi:10.1016/S0006-3495(85)83882-0
23. Das, G.; Patra, N.; Gopalakrishnan, A.; Zaccaria, R. P.; Toma, A.; Thorat, S.; Di Fabrizio, E.; Diaspro, A.; Salerno, M. *Analyst* **2012,** *137,* 1785. doi:10.1039/c2an16022f
24. Thorat, S.; Diaspro, A.; Scarpellini, A.; Povia, M.; Salerno, M. *Materials* **2013,** *6,* 206–216. doi:10.3390/ma6010206
25. Das, G.; Patra, N.; Gopalakrishanan, A.; Proietti Zaccaria, R.; Toma, A.; Thorat, S.; Di Fabrizio, E.; Diaspro, A.; Salerno, M. *Microelectron. Eng.* **2012,** *97,* 383–386. doi:10.1016/j.mee.2012.02.037
26. Zheng, J.; Zhou, Y.; Li, X.; Ji, Y.; Lu, T.; Gu, R. *Langmuir* **2003,** *19,* 632–636. doi:10.1021/la011706p
27. Mayo, D. W.; Miller, F. A.; Hannah, R. W. In *Course Notes on the Interpretation of Infrared and Raman Spectra;* Mayo, D. W.; Miller, F. A.; Hannah, R. W., Eds.; Wiley: Hoboken, NJ, U.S.A., 2004; i–xxvi. doi:10.1002/0471690082.fmatter
28. Velleman, L.; Bruneel, J.-L.; Guillaume, F.; Losic, D.; Shapter, J. G. *Phys. Chem. Chem. Phys.* **2011,** *13,* 19587–19593. doi:10.1039/c1cp21765h
29. An, H. H.; Han, W. B.; Kim, Y.; Kim, H.-S.; Oh, Y.; Yoon, C. S. *J. Raman Spectrosc.* **2014,** *45,* 292–298. doi:10.1002/jrs.4461
30. Taylor, R. W.; Benz, F.; Sigle, D. O.; Bowman, R. W.; Bao, P.; Roth, J. S.; Heath, G. R.; Evans, S. D.; Baumberg, J. J. *Sci. Rep.* **2014,** *4,* 5940. doi:10.1038/srep05940
31. Schulz, H.; Baranska, M. *Vib. Spectrosc.* **2007,** *43,* 13–25. doi:10.1016/j.vibspec.2006.06.001
32. Köhler, M.; MacHill, S.; Salzer, R.; Krafft, C. *Anal. Bioanal. Chem.* **2009,** *393,* 1513–1520. doi:10.1007/s00216-008-2592-9
33. Zumbusch, A.; Langbein, W.; Borri, P. *Prog. Lipid Res.* **2013,** *52,* 615–632. doi:10.1016/j.plipres.2013.07.003
34. Czamara, K.; Majzner, K.; Pacia, M. Z.; Kochan, K.; Kaczor, A.; Baranska, M. *J. Raman Spectrosc.* **2015,** *46,* 4–20. doi:10.1002/jrs.4607
35. Richter, R. P.; Bérat, R.; Brisson, A. R. *Langmuir* **2006,** *22,* 3497–3505. doi:10.1021/la052687c
36. Reimhult, E.; Höök, F.; Kasemo, B. *Langmuir* **2003,** *19,* 1681–1691. doi:10.1021/la0263920
37. Peng, P.-Y.; Chiang, P.-C.; Chao, L. *Langmuir* **2015,** *31,* 3904–3911. doi:10.1021/la504532a
38. Campiña, J. M.; Martins, A.; Silva, F. *J. Phys. Chem. C* **2007,** *111,* 5351–5362. doi:10.1021/jp0662146
39. Hewas, A. M. Analysis of metal ions in water using SAM-modified EQCM electrodes. Ph.D. Thesis, Department of Chemistry, University of Leicester, 2013.

License and Terms